MONASH University

A Single Molecule Localization and *In situ* Crosslinking Study of the Beta-barrel Assembly Machinery in *Escherichia coli*

Sachith Dilshan Gunasinghe
BSc (Honours)

A thesis submitted for the degree of Doctor of Philosophy

at Monash University in 2017

Department of Microbiology

Biomedicine Discovery Institute

Copyright notice

Abstract

The Beta-barrel Assembly Machinery (BAM) complex of bacteria is essential for cell viability. In *E. coli* it is identified as a hetero-oligomer comprising of BamA core beta-barrel and four other accessory lipoproteins (BamB-E). Importantly, the BAM complex forms the central hub of bacterial outer membrane protein assembly where the transport pathway delivers a number of different proteins to the cell surface. Despite numerous structural biological evidence gathered through crystallography, a huge gap of knowledge still prevails regarding the protein assembly mechanism deployed by the BAM complex *in vivo*. Especially in the absence of any potential energy source in the periplasmic space, it is still unclear how the BAM complex catalyses nascent beta-barrel protein assembly and insertion into the outer membrane.

I attempted to shed light on some of these unanswered questions through studying the spatio-temporal organization of the BAM complex *in vivo* using single molecule localization microscopy techniques described in Chapter 3. This study revealed that the BAM complex exists as highly organised assembly precincts (clusters) in the cell surface of *E. coli* outer membrane and the auxiliary lipoprotein subunit BamB was crucial to maintain this spatial distribution. In Chapter 4, using *in situ* crosslinking approaches I was able to characterise unorthodox interfaces of the BamB beta-propeller that could promote non-canonical protein interactions between neighbouring BAM complexes, in turn, facilitating the formation of the protein assembly precincts in the outer membrane.

These findings provide a missing piece of the mechanistic puzzle of the BAM complex in catalysing the assembly and insertion of substrate outer membrane proteins. Additionally, this *in vivo* surface localization study carried out on *E. coli* BAM complex provide some groundwork to spatially characterise similar supramolecular assembly nano-machines in other gram-negative bacteria.

Declaration

This thesis contains no material which has been accepted for the award of any other degree or diploma at any university or equivalent institution and that, to the best of my knowledge and belief, this thesis contains no material previously published or written by another person, except where due reference is made in the text of the thesis.
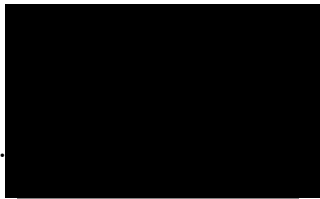
……⬛⬛⬛⬛..   31st October 2017
                                                 …………………………

Sachith Dilshan Gunasinghe   **Date**

Publications during enrolment

Gunasinghe SD, Webb CT, Elgass KD, Hay ID and Lithgow T (2017), Super-Resolution Imaging of Protein Secretion Systems and the Cell Surface of Gram-Negative Bacteria. *Front. Cell. Infect. Microbiol.* 7:220.doi: 10.3389/fcimb.2017.00220

Acknowledgements

First and foremost I would like to thank my excellent supervisor Prof. Trevor Lithgow for giving me this wonderful opportunity and especially believing in a chemist to do all these microbiology work. Your constant support, supervision and sometimes bit of a motivational boost helped me immensely during this PhD. Your creative nature towards solving fundamental questions in biology inspired me and I will strive to emulate your professionalism throughout my research career.

I would like to extend my gratitude to my co-supervisors Dr. Toby Bell and Dr. Kirstin Elgass for introducing me to the amazing technology of Super resolution microscopy. Your profound knowledge about the subject matter helped to fashion my experiments and eventually to build a successful research out of it.

To my collaborators, I am ever grateful for your support during my PhD. Your professional advice shaped my research project in many positive ways. To Dr. Keith Schulze, thank you for devoting your time and efforts in helping me with the enormous task of image analysis. Without your persistent support, this dissertation would not have been successful. To Dr. Alex Fulcher, thank you for being a good friend and a teacher in microscopy. To Dr. David Steer, thank you for your expertise in mass spectrometry analysis. To Dr. Peter Boag, thank you for giving me permission to use your lab microscope.

To all the Lithgow lab members, thank you for making my PhD journey one of the memorable experiences ever. Special thanks to Dr. Chaille Webb, Dr. Takuya Shiota, Dr. Iain Hay, Dr. Rhys Dunstan and Dr. Christopher Stubenrauch for dedicating your time and efforts on shaping my PhD. To Dr. Matt Belousoff and Dr. Denisse Leyton, thank you for your many advices over the years. To Von Torres (my lovely neighbour), Tricia Lo (my other lovely neighbour), Pankaj Deo, Seong Hoong Chow, Kher Shing Tan (our lovely

RA), Rebecca Bamert (from great Aussie bake-off), Gilu Abraham, Matthew Stellato, Julie Nguyen, Jonathan Wilksch, Jiyoti Verma, Victoria Hewitt and Eric Mandela, thank you for your support.

Finally to my family, words cannot describe how thankful I am to you. Thank you to my lovely wife, who has always been a positive force in my life. I am ever grateful for your love and support every day. This would not have been possible without you by my side. To my big brother, thank you for your support and making the Aussie experience the best. My mother and father, to your endless love, support and many life lessons, I am eternally grateful. Finally to my grandparents, thank you for your many blessings, and thank you for believing in me, always.

Contents

List of figures

Chapter 5

List of tables

Abbreviations

AT	Autotransporters
APS	Ammonium persulfate
BAM	Beta-barrel Assembly Machinery
BN	Blue Native
BPA	p-benzoyl-L-phenylalanine
BSA	Bovine serum albumin
DIC	Differential interference contrast
DDM	n-Dodecyl β-D-maltoside
*d*STORM	Direct stochastic optical reconstruction microscopy
DTT	Dithiothreitol
ECL	Enhanced chemiluminescence
EDTA	Ethylenediaminetetraacetic acid
EM	Electron microscopy
EPEC	Enteropathogenic *Escherichia coli*
FRAP	Fluorescence recovery after photobleaching
GSH	Glutathione
IM	Inner membrane
kDa	Kilo Dalton
LB	Luria broth
LPS	Lipopolysaccharide
MEA	2-aminoethanethiol
OD	Optical density
OM	Outer membrane
OMPs	Outer membrane proteins
PA	Photo activated
PALM	Photoactivation localization microscopy
PAGE	Polyacrylamide gel electrophoresis

PBS	Phosphate buffered saline
PCR	Polymerase chain reaction
PMSF	Phenylmethanesulfonyl fluoride
POTRA	Polypeptide transport-associated
PPP	Planar Point Pattern
PSF	Point spread functions
rpm	Revolutions per minute
RESOLFT	Reversible saturable optical fluorescence transitions
ROI	Region of Interest
SDS	Sodium dodecyl sulphate
SIM	Structured illumination microscopy
SMLM	Single molecule localization microscopy
SNR	Signal-to-noise ratio
SR	Super Resolution
STED	Stimulated emission depletion
STORM	Stochastic optical reconstruction microscopy
TBS	Tris-buffered saline
TCA	Trichloroacetic acid
TEMED	Tetramethylethylenediamine
TIRF	Total internal reflection fluorescence
°C	Degrees Celsius
x g	Times gravity

Chapter 1: Introduction

1.1 Spatial heterogeneity in bacterial membranes.

From population level to molecular level, heterogeneity is found everywhere in the microbial world. Bacteria are known to show very noticeable morphological features such as flagella, pili and division septa, which at the cellular level underline an asymmetric distribution of membrane proteins. Particularly in rod-shaped bacteria, it has been well documented that a large number of proteins have distinct subcellular localizations at specific times to perform vital functions associated with the cell membrane (Shapiro et al., 2002; Fishov and Norris, 2012). Studies involving clustering of the chemotaxis receptor network proteins (mediating responsiveness to chemotaxis)(Ames and Parkinson, 2006), FtsZ ring structure formation at mid-cell region (governing cytokinesis)(Bi and Lutkenhaus, 1991), production of sporulation proteins and their assembly (regulating spore morphogenesis)(Driks and Losick, 1991) and polar specific MreB and PopZ proteins (organizing cell wall synthesis and chromosomal segregation respectively)(Gahlmann and Moerner, 2014) are some examples that explicitly describes spatial heterogeneity of membrane proteins and how it orchestrates cellular dynamics at a molecular level (Rudner and Losick, 2010). The uneven distribution of fluorescently stained membrane lipid (Christensen et al., 1999; Fishov and Woldringh, 1999) and discrete localization sites observed for fluorescently labelled lipopolysaccharides (LPS) (Begg and Donachie, 1973; Ryter et al., 1975; Ghosh and Young, 2005) indicates that this heterogeneity is not restricted to outer membrane proteins (OMPs).

Formation of membrane domains as a result of coupled events involving transcription and translation, followed by protein assembly and insertion has been previously demonstrated

to be one of the major reasons for bacterial membrane heterogeneity (Norris and Madsen, 1995; Binenbaum et al., 1999; Bakshi et al., 2012). In simple terms, heterogeneity implies privileged spaces or "hot spots" for extended molecular interactions, mediated through either lipid-lipid, protein-protein or lipid-protein associations. So what could be the mechanism driving this heterogeneous organization of cell envelop constituents?

1.2 Imaging beyond the classical limits; the advent of super resolution microscopy.

Fluorescence microscopy has proven to be a powerful tool for cell biologists, given the wide array of fluorescent probes available (fluorescent fusion proteins, chromosomal tags and fluorescent antibodies) that can be utilised to specifically label and detect sub-cellular components in a cellular context. Together with increasingly higher quality optics, sensitive detectors and coherent light sources, the resolution capacity of fluorescence microscopy has now been extended to generate superior images with finer details than ever before. Until these recent developments, microbiologists were unable to fully capitalize on fluorescence microscopy, since the diffraction limit of light means only objects larger than ~250 nm in lateral dimension and ~500 nm in axial dimension could be resolved: any objects smaller than these limits are merely blurred spots (Patterson et al., 2010). Many of the structures of interest in microbes are much smaller than this classical limit, with bacteria themselves only 1-10 µm in length (Koch, 1996).

The advent of super-resolution microscopy extended the classical limit imposed by conventional light microscopy (Hell, 2007; 2009; Huang et al., 2009; Huang et al., 2010). There are two general classes of super-resolution microscopy. The first class of imaging modalities utilises spatially patterned fluorescence excitation beams to achieve the sub-

diffraction level of resolution. The most notable examples of this technique are stimulated emission depletion (STED) microscopy (Hell and Wichmann, 1994; Klar and Hell, 1999), reversible saturable optical fluorescence transitions (RESOLFT) microscopy (Hell and Wichmann, 1994; Hofmann et al., 2005) and structured illumination microscopy (SIM) (Gustafsson, 2000; 2005). The second class circumvents the diffraction barrier through actively controlling the fluorescence emitter (fluorescent proteins, antibodies or tags) concentrations by stochastic photo-activation or by stochastic photo-switching (Heilemann et al., 2009a; Lippincott-Schwartz and Patterson, 2009; Kamiyama and Huang, 2012), thereby enabling spatio-temporal resolution of emitter localizations. This class includes photoactivation localization microscopy (PALM) (Betzig et al., 2006) and stochastic optical reconstruction microscopy (STORM), collectively known as single molecule localization microscopy (SMLM) (Rust et al., 2006). These techniques are documented to reach 10-25 nm of lateral resolution (Kamiyama and Huang, 2012), sufficient scale to visualize macromolecules in small cellular systems (Figure 1.1).

A

Acquiring series of stochastic photo-switching events

Superimposition of centroid determined images

Reconstruction of mapping spatial localizations

B

Reconstruction of mapping spatio-temporal trajectories

time

Stochastic photo-activation followed by spatial trajectory mapping of molecules

C

Photobleaching

Fluorescence recovery time

D

Evanescent field

Coverslip

Incident beam

Reflected beam

Figure 1.1 Methods for single molecule localization and tracking. (A) STORM and **(B)** PALM super-resolution microscopy, collectively referred to as single molecule localization microscopy methods (SMLM). These modalities utilise stochastic photo-switching or photo-activation of a subset of fluorescence emitters to achieve sub-diffraction resolution of 10-25 nm in lateral dimensions. PALM is well known for live cell imaging and mapping spatiotemporal trajectories of individual fluorescently labelled molecules (Manley et al., 2008). STORM technique is documented for its use in determining the localised positioning of fluorescently labelled molecules in both live and fixed samples (Kamiyama and Huang, 2012). Mobility of fluorescent fusion proteins in live cells can also be surveyed through **(C)** FRAP and **(D)** TIRF microscopy techniques. In FRAP experiments, a relatively small area within the cell is being irreversibly photo-bleached by a high intense laser beam, followed by subsequent monitoring of the redistribution of non-bleached fluorescence molecules into the photo-bleached region under low laser power. TIRFM relies upon the generation of a rapidly decaying evanescent field at the interface of sample and coverslip to sparsely excite fluorophores, providing a high signal-to-background ratio in single particle tracking studies (Toomre and Bewersdorf, 2010).

1.3 Understanding the complex architecture of outer membrane in bacteria.

In order to exploit their environmental niches, bacteria undertake vital tasks such as sensing the external milieu, cell to cell communication, nutrient uptake against concentration gradients, cell-cell warfare and the secretion of macromolecules into the environment. Gram-negative bacteria have a highly evolved cell wall with two membranes composed of a complex array of integral and peripheral proteins, as well as phospholipids and glycolipids. The outer membrane is an asymmetric bilayer, with the inner leaflet comprised of phospholipids and the outer leaflet instead composed from lipopolysaccharides (LPS) (Figure 1.2). As discussed herein, we are beginning to appreciate that this asymmetric lipid environment promotes spatial heterogeneity of membrane constituents and impedes the sort of lateral mobility that is common for the proteins integrated in phospholipid bilayers. Super resolution microscopy is being applied to dissect diverse aspects of bacterial cell biology, including membrane protein structure

and dynamics (Xie et al., 2008). Here, we highlight the advances that have been made in understanding spatial-temporal characteristics of bacterial surface proteins, particularly protein secretion systems, that the recent advances in microscopy has allowed. To date, model bacterial systems like *Escherichia coli* and *Caulobacter cresentus* have been the subject for the majority of single molecule localization studies (Gahlmann and Moerner, 2014).
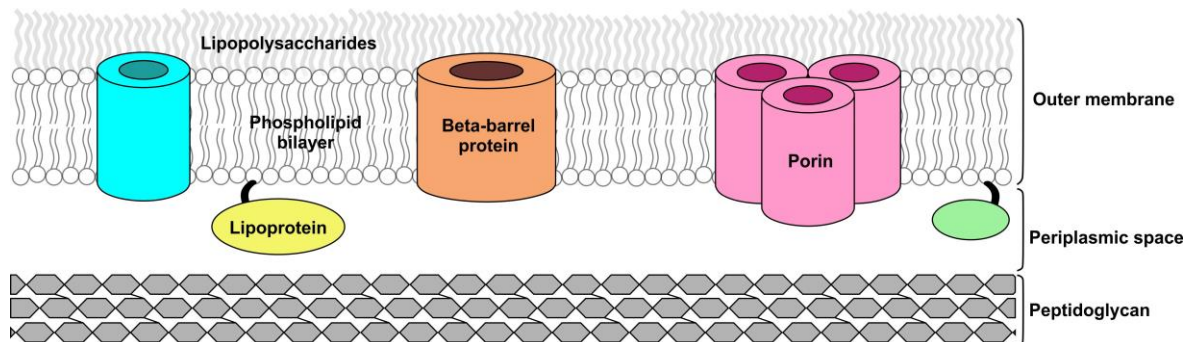
Figure 1.2 Architecture of bacterial outer membrane. A majority of outer membrane proteins have a beta-barrel topology and this includes commonly found porins spanning the membrane of Gram-negative bacteria. Lipoproteins are lipid anchored to the inner leaflet of the outer membrane. The outer leaflet is dominated by lipopolysaccharides (LPS) making this bilayer evermore asymmetric.

1.4 Fluorescence imaging of outer membrane structure, biogenesis and spatio-temporal organization.

1.4.1 Fluorescence imaging of outer membrane proteins (OMPs).

Most bacterial outer membrane proteins (OMPs) have a β-barrel architecture (De Geyter et al., 2016; Plummer and Fleming, 2016; Noinaj et al., 2017; Slusky, 2017) and, of these, the channels that allow for selective permeability of small molecules across the outer membrane are referred to as porins (Hancock, 1987). Some of these porins display surface exposed extracellular domains, often simply loops of polypeptide between adjacent β-strands, which none the less provide the means to fluorescently label them for mobility assessment studies on live cells (Gibbs et al., 2004; Spector et al., 2010; Rassam et al., 2015) (Figure 1.3). With the aid of fluorescence recovery after photo-bleaching (FRAP) and single particle tracking using total internal reflection fluorescence microscopy (TIRFM), we are now beginning to understand time-resolved spatial movements of these membrane proteins (Gibbs et al., 2004; Spector et al., 2010; Rothenberg et al., 2011; Rassam et al., 2015).
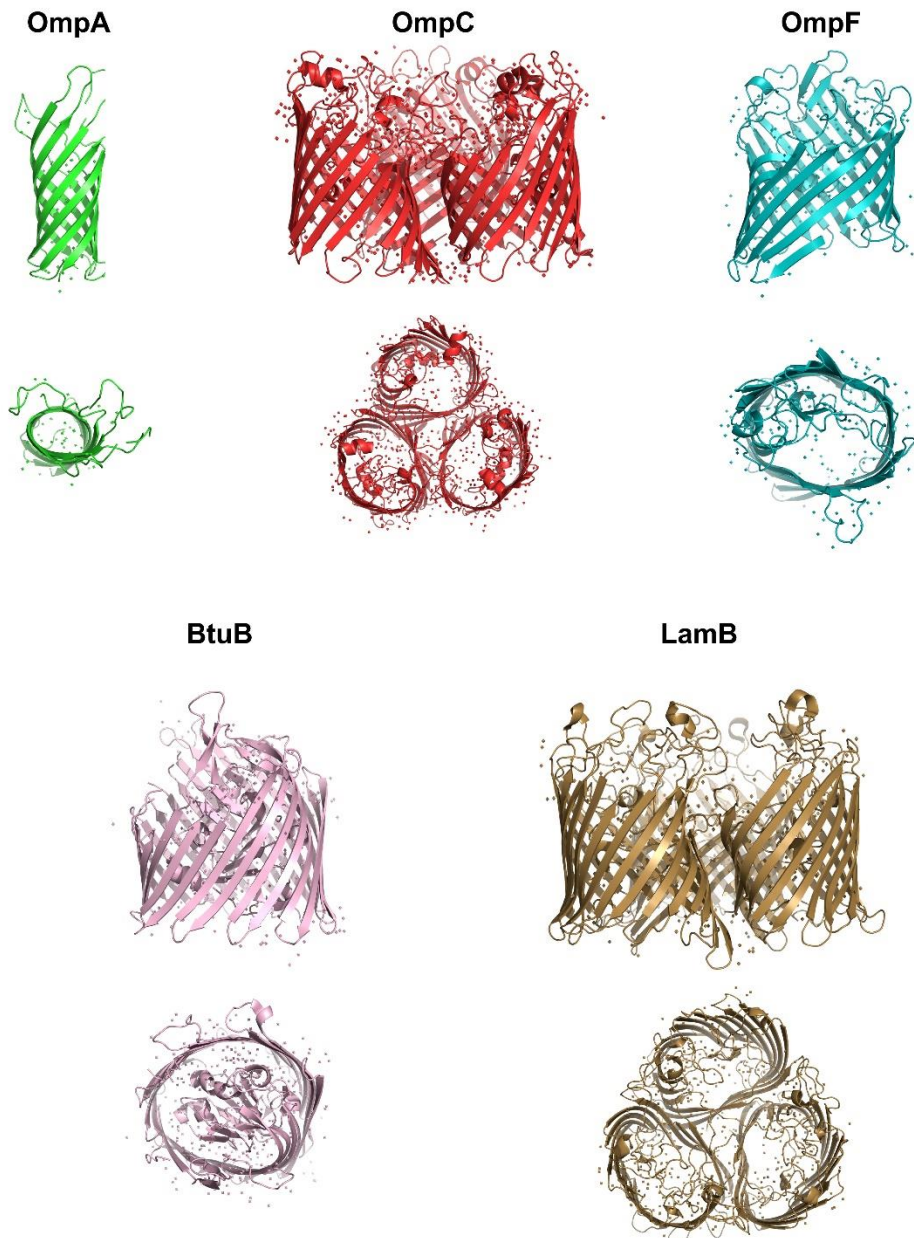
Figure 1.3 Crystal structures of commonly found porins with their extracellular loop domains exposed to the extracellular milieu (side view and top view form the extracellular side accordingly). OmpA is known to be involved in bacterial conjugation. The most abundant porins OmpC and OmpF are known to exists in trimeric forms and facilitate diffusion of small molecules across the membrane. Cobalamin receptor BtuB actively translocates vitamin B12 across the outer membrane, while maltoporin LamB transport maltose across the membrane (PDB: 1bxw, 2j1n, 1mpf, 2guf, 1af6).

LamB is a trimeric porin responsible for maltose uptake in *E. coli* (Schirmer et al., 1995). LamB also serves as the receptor for certain bacteriophages (Chatterjee and Rothenberg, 2012), and has been extensively studied in terms of diffusion dynamics. Using various labelling techniques and different imaging modalities, LamB mobility has been described using parametric measurements such as the short-time diffusion coefficient. In essence, this quantifies the area a molecule inhabits in a per second measurement. LamB displays a short-time diffusion coefficient of $0.15 - 0.06$ $\mu m^2\,s^{-1}$, with each molecule therefore being confined to a space of ~20 nm at the outer membrane (Oddershede et al., 2002; Gibbs et al., 2004; Rothenberg et al., 2011). Similar results have come from studies of other porins. OmpF, for example, was reported to have short-time diffusion coefficients of 0.006 $\mu m^2\,s^{-1}$ (Spector et al., 2010). Similarly, a short-time diffusion coefficient of 0.05 $\mu m^2\,s^{-1}$ was reported for the TonB-dependent receptor BtuB, which facilitates cobalamin uptake (Spector et al., 2010). For both OmpF and BtuB, recent work has suggested that their distribution and relative immobility may be due to non-specific, protein-protein interactions (Rassam et al., 2015). OmpA functions to lock the outer membrane to the under-lying peptidoglycan layer, and it had been expected that this feature alone would dictate the relative immobility predicted for OmpA (Samsudin et al., 2016). However, deletion of the peptidoglycan binding domain of OmpA, did not affect the diffusion coefficient measurements for the β-barrel domain of OmpA (Verhoeven et al., 2013). These and other studies have led to the understanding that, compared to inner membrane proteins, OMPs generally display orders of magnitude slower diffusion dynamics whether or not they are tethered to other cellular structures (Oddershede et al., 2002; Gibbs et al., 2004; Spector et al., 2010; Rothenberg et al., 2011; Ritchie et al., 2013; Verhoeven et al., 2013; Rassam et al., 2015).

Few studies have directly addressed the spatio-temporal aspects of the process of β-barrel assembly into the outer membrane. In one, temporal labelling of LamB appearance on the bacterial cell surface has been studied in elegant work, using detailed computational analysis to reconstruct the first spatio-temporal distribution of OMP biogenesis (Ursell et al., 2012). Employing site specific protein labelling strategy, using Sfp phosphopantetheinyl transferase to covalently label emergent loops of nascent LamB molecules, the appearance and mobility of LamB molecules was monitored through time-lapse fluorescence microscopy. Using inducible pulse-chase expression of LamB, an initial emergence of fluorescent punctae was observed which represents a heterogeneous distribution of fluorescent spots per bacterium. The heterogeneous localization of LamB was due to discrete bursts of insertion of unlabelled new material at discrete sites throughout the outer membrane. The numbers of these punctae is similar to the number of sites estimated in an early EM-based study that captured porin insertion sites in *Salmonella* Typhimurium using ferritin-conjugated OMP-specific antibodies (Smit and Nikaido, 1978). Importantly, FRAP experiments showed that any laterally measurable movement of the OMPs across the bacterial cell surface was dependent on membrane growth and was not diffusional (Ursell et al., 2012). Since LamB also serves as receptor for several bacteriophages (Hancock and Reeves, 1976), fluorescently labelled λ phage tails have also been used to monitor the endogenous distribution of LamB, without plasmid-borne over-expression, and these studies too find it to be driven by cell growth and elongation (Gibbs et al., 2004).

The process of outer membrane biogenesis also depends on OMP turn-over through generational change in an *E. coli* population. A recent study using covalently modified colicins to fluorescently label the TonB-dependent receptors BtuB and Cir elegantly followed this process through TIRFM (Rassam et al., 2015). BtuB and Cir were observed

to be clustered together in "OMP islands", huge rafts with an average size of ~0.5 μm (hundreds to thousands of protein molecules would be encompassed in this island, with little or no interstitial lipid present). Unlike the LamB studies, where new material was delivered at points throughout the cell surface, Rassam *et al.,* suggested that the insertion of new BtuB and Cir into these rafts was only observed in the mid-cell region (Rassam et al., 2015). Irrespective of the site of new material deposition, computer modelling studies (Wang et al., 2008; Ursell et al., 2012; Rassam et al., 2015) have demonstrated that in either scenario, pre-existent OMPs and LPS will always tend to be forced towards poles, and that cell division will ultimately yield an unequal partitioning of membrane materials to create distinct subpopulations of cells, ones having mixed set of old and new material and others with predominantly or exclusively "young" OMPs (Figure 1.4). Within a bacterial population this then creates a range of phenotypes in the OM proteome, and a range of adaptive advantages for individual bacteria to survive and replicate in the environment. In various ways, other studies have demonstrated how "older" elements of the other major cell envelope constituents, LPS and peptidoglycan, are also ultimately retained at cell poles (Kato et al., 1990; Kato et al., 2000; De Pedro et al., 2003; Thiem et al., 2007; Thiem and Sourjik, 2008). *In silico* models have predicted this type of protein clustering and binary partitioning with OMPs. For example, this temporal positioning has been observed to be important in resolving protein aggregates associated with bacterial cell aging, but is also important in positioning chemoreceptor arrays and regulation of cell division (Janakiraman and Goldberg, 2004; Thiem et al., 2007; Lindner et al., 2008; Thiem and Sourjik, 2008).
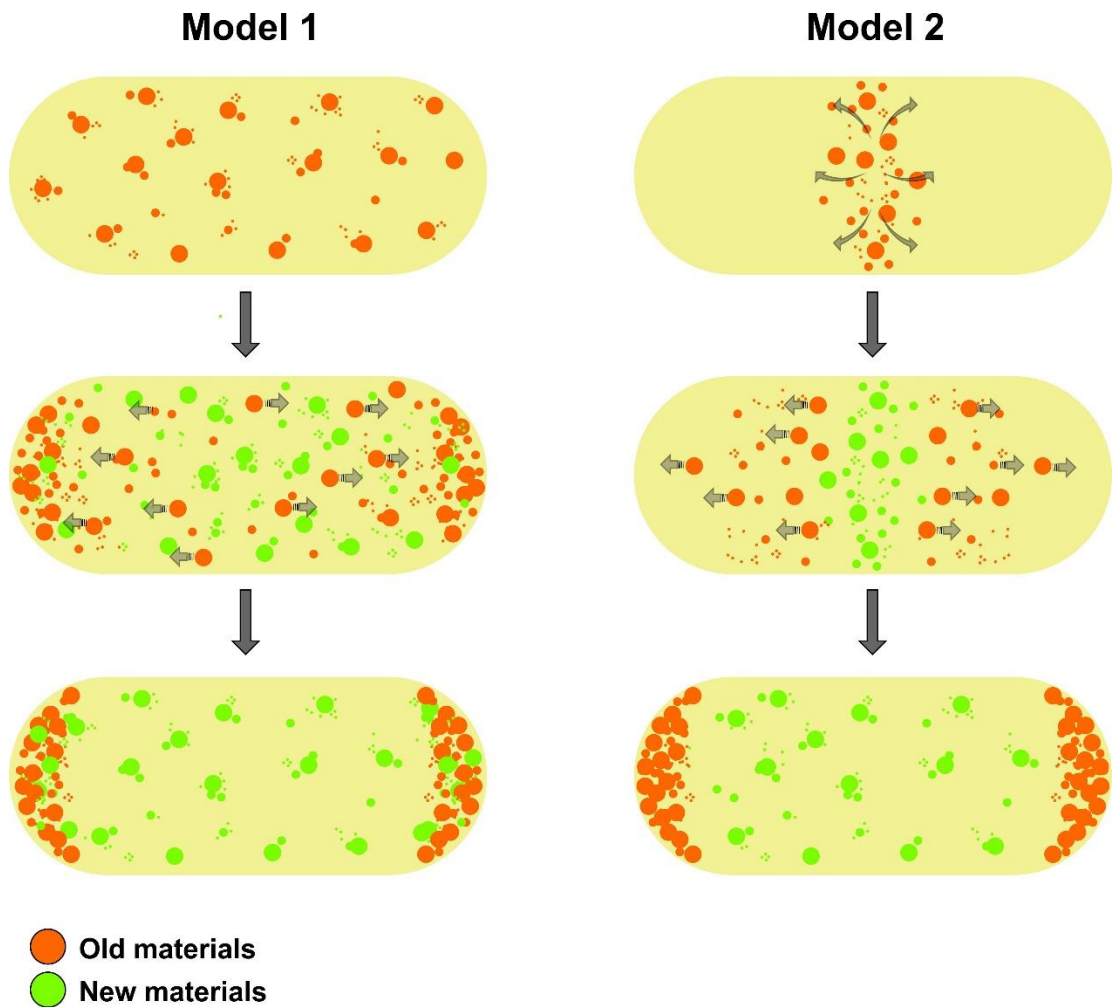
Figure 1.4 Two models depicting insertion of new materials and their distribution across the outer membrane. Model 1 shows the insertion sites for new materials are located heterogeneously across the outer membrane (Ursell et al., 2012). Model 2 suggests new material deposition occurs predominantly at the mid-cell regions (Rassam et al., 2015). In both models, the pre-existent materials (orange) will always tend to be forced towards bacterial cell poles, and the cell division will ultimately yield an unequal partitioning of "new" and "old" membrane materials in their progeny.

1.4.2 Fluorescence imaging of lipopolysaccharides (LPS) at the outer membrane.

In this emerging paradigm of membrane spatial rigidity, it has become clear that the distribution of LPS is also greatly constrained. By fluorescently labelling LPS via the α-mannose moiety of its O-antigen, distinct helical ribbon-like geometric arrangements were observed for LPS on live *E.coli* (Ghosh and Young, 2005). Very low diffusion coefficients reported by FRAP experiments showed that LPS molecules were practically immobile by comparison with the (already very low) OMP diffusion rates (Mühlradt et al., 1973; Schindler et al., 1980). The current hypothesis is that LPS helical ribbons may represent a geometric arrangement important for staging outer membrane biogenesis. Given the high abundance yet constrained spatial distribution of LPS, it is becoming clear that any model for protein transport into or across the outer membrane will need to take into account this spatial information.

1.5 Bacterial secretion systems and membrane protein dynamics through the eyes of super resolution microscopy.

SMLM with its array of fluorescent labelling strategies coupled with advanced microscopy optics and various image analysis algorithms has the capacity to investigate spatial dynamics of macromolecules in bacteria at a nanoscopic resolution, providing unprecedented amount of details in cellular membrane architecture. Aforementioned fluorescent fusion proteins and its wide applicability in fluorescence microscopy to image and track membrane protein trajectories in various biological settings have paved the path to understand how protein-protein interactions can occur in a context as dynamic as the cell surface.

Recent super resolution studies using SMLM have emerged focused on understanding spatial dynamics and localizations of membrane-bound virulence factors and secretion systems in gram-negative bacteria. Based on photo-activated mCherry (PAmCherry) fluorescence fusions, Haas *et al*., was able to characterise three distinct sub-populations of TcpP inner membrane protein, based on their highly heterogeneous diffusion patterns in live *Vibrio cholerae* (Haas et al., 2015). TcpP plays an essential role in the ToxR regulon, which ultimately act as the transcriptional regulator for cholera toxin expression (Childers and Klose, 2007; Haas et al., 2015). Using PALM they were able to assess the changes of TcpP mobility in mutant strains lacking toxR and toxT promoters compared to wild-type strains. Thus, providing new mechanistic insights into the series of transcriptional activation events take place in *Vibrio cholerae* pathogenicity. PAmCherry fluorescence fusion tag approach was further extended to image the localization of Type 4 pili (T4P) component BfpB in enteropathogenic *Escherichia coli* (EPEC) (Lieberman et al., 2012). PALM was able to capture single molecule localization events of BfpB-PAmCherry to provide new evidence for previously undetected non-polar distribution patterns involving T4P biogenesis. These observably diverse sub cellular structures of the secretion system may overall influence pilus function in different bacterial species.

With the versatility of genetically encoded self-labelling enzyme tags (Halo-tag and SNAP-tag), Barlag *et al*., was able to image subunits of T1SS and T3SS in *Salmonella enterica* at a nanoscopic level (Barlag et al., 2016). They have reported diffusion coefficients for SiiF from T1SS and SpaS from T3SS to be 0.008 ± 0.0002 $\mu m^2 s^{-1}$ and 0.055 ± 0.002 $\mu m^2 s^{-1}$ respectively and they appeared to have a clustered distribution at the inner membrane compartment. Another study, using the same genetic labelling strategy, was able to elucidate starch utilization by well-known human gut symbiont *Bacteroides thetaiotaomicron* via the Sus complex (Karunatilaka et al., 2014). The Sus complex

consists of eight sub-units; five outer membrane components (SusCDEFG), two periplasmic components (SusAB) and one inner membrane component (SusR) (Cameron et al., 2012). In the presence of starch molecules, fluorescently tagged SusG, the key lipoprotein component responsible for starch degradation in Sus complex, displayed to have a dominant subpopulation of rapidly diffusing molecules (~60%) at the outer membrane. In this study, the other startling observation was in the presence of simple sugars such as glucose, SusG remained in monomeric or dimeric form, while in the presence of complex sugars, it tends to form molecular aggregates or clusters. These observations may provide new clues on efficient polysaccharide catabolism through Sus complex.

Collectively, these studies have shown the resourcefulness of fluorescent tags and how they can be utilized in super resolution imaging of subunits of membrane protein complexes without drastically altering their original functionality and in turn being faithful to their endogenous interactome *in vivo*.

1.6 Beta-barrel assembly machinery (BAM) complex.

During billions of years of evolution, bacteria have developed a number of different pathways and mechanisms to efficiently secrete proteins across or into their cellular envelops. To adequately accomplish this process, gram-negative bacteria exploit over six different secretion pathways (Dalbey and Kuhn, 2012). Two main pathways are known to translocate OMPs across the IM; SecYEG and TatABC machineries. Lipoproteins are shuttled to the OM via the Lol pathway while OM beta barrel proteins proceed to the beta barrel assembly machinery (BAM) for their final insertion. The process of beta barrel protein biogenesis, assembly and insertion into the hydrophobic lipid bilayer is

thermodynamically unfavourable since there is no potential energy source at the periplasmic-outer membrane space to form hydrogen bonds between the transmembrane segments of beta barrel proteins (Hagan et al., 2011; Fleming, 2015; De Geyter et al., 2016). This seemingly complex set of events is known to be coordinated by the BAM complex (Ruiz et al., 2006; Walther et al., 2009; Tommassen, 2010). It consists of a BamA beta barrel, the key component of BAM machinery that catalyses substrate beta barrel protein insertion and folding through a beta-augmentation mechanism (Voulhoux et al., 2003; Heuck et al., 2011), as well as up to four associated lipoproteins (BamB,C,D and E) (Figure 1.5) (Wu et al., 2005).
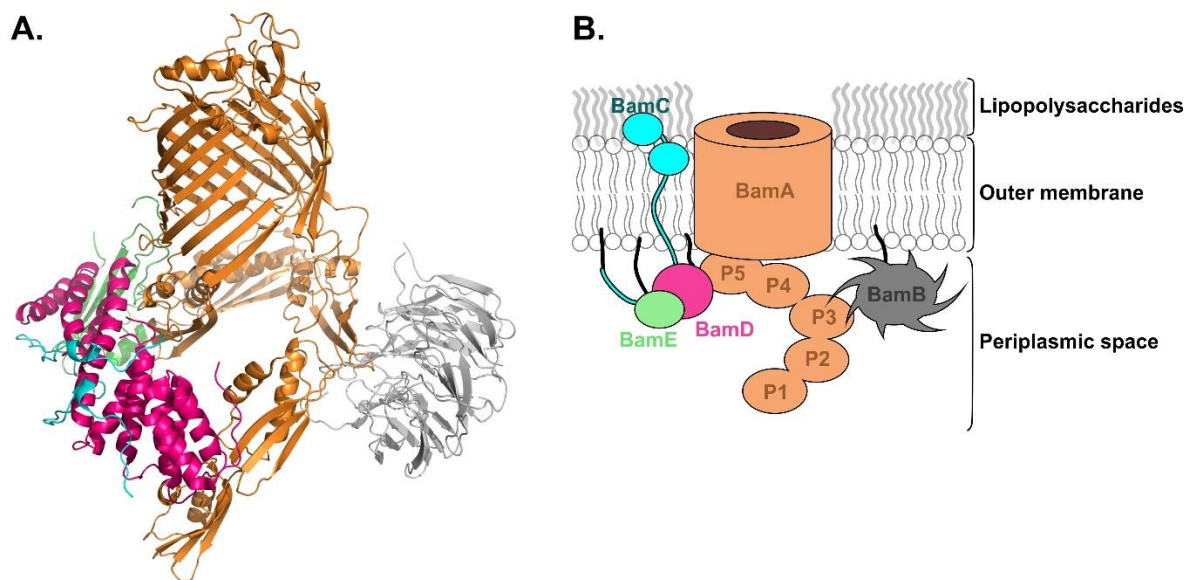
Figure 1.5 Structure of the Beta-barrel assembly machinery (BAM) complex. (A) Crystal structure of the BAM complex (PBD: 5ayw). **(B)** Generalised structure of the BAM complex embedded in the outer membrane. The C-terminus of BamA forms a membrane spanning beta-barrel and the N-terminus has five identical periplasmic extensions known as the Polypeptide Transport Associated (POTRA) domains. All the lipoproteins BamB, BamC, BamD and BamE are lipid anchored to the inner leaflet of the outer membrane. Only BamB and BamD have direct contact with BamA. (A) and (B) have the same colour coding for BAM complex subunits.

1.6.1 Molecular mechanism of beta-barrel protein biogenesis via BAM complex.

Unlike other beta-barrel proteins that populate the outer membrane, the BamA beta-barrel domain displays some unique features. The region of lateral gate opening formed between the first (β1) and last (β16) beta strands of the barrel is known to have unusually low hydrophobic thickness which disorders the surrounding lipid bilayer (Noinaj et al., 2013; Sinnige et al., 2014). By creating these lipid bilayer defects, BamA presumably lowers the energetic barrier to insert newly folded OMPs to the outer membrane. Several different mechanisms have been suggested to explain the complex process of OMP folding and insertion (Kim et al., 2012). To date, perhaps the most plausible mechanism would be the one that describes how BamA beta-barrel serve as a folding template for incoming beta-barrel substrates. This model requires BamA to have conformational changes that would result in opening the beta-barrel by breaking hydrogen bonds and then subsequently forming new hydrogen bonds with the substrates via beta-augmentation. With the recently solved open conformation of BamA beta-barrel structure (Figure 1.6) providing some evidence for this hypothesis, we are now beginning to unravel the sequence of conformational rearrangements that could occur during the event of insertion of nascent beta-barrel proteins at the outer membrane (Bakelar et al., 2016). An extension of this model would be multiple BamA components participating in a multimeric fashion (oligomerise) to achieve more efficient catalysis of beta-barrel protein folding and assembly. However, no prevailing structural biological evidence supports this hypothesis.

Although recent crystal structures of the BAM complex provide snap-shots of different spatial conformations it may occupy to accommodate different substrates (Bakelar et al., 2016; Gu et al., 2016), some of the key events surrounding nascent OM beta barrel protein folding and assembly remains to be elucidated. In particular, demonstrating how the BAM

complex behaves in a membrane environment, interacting with other major outer membrane constituents, needs new means of investigation.

BamA
Close conformation

BamA
Open conformation
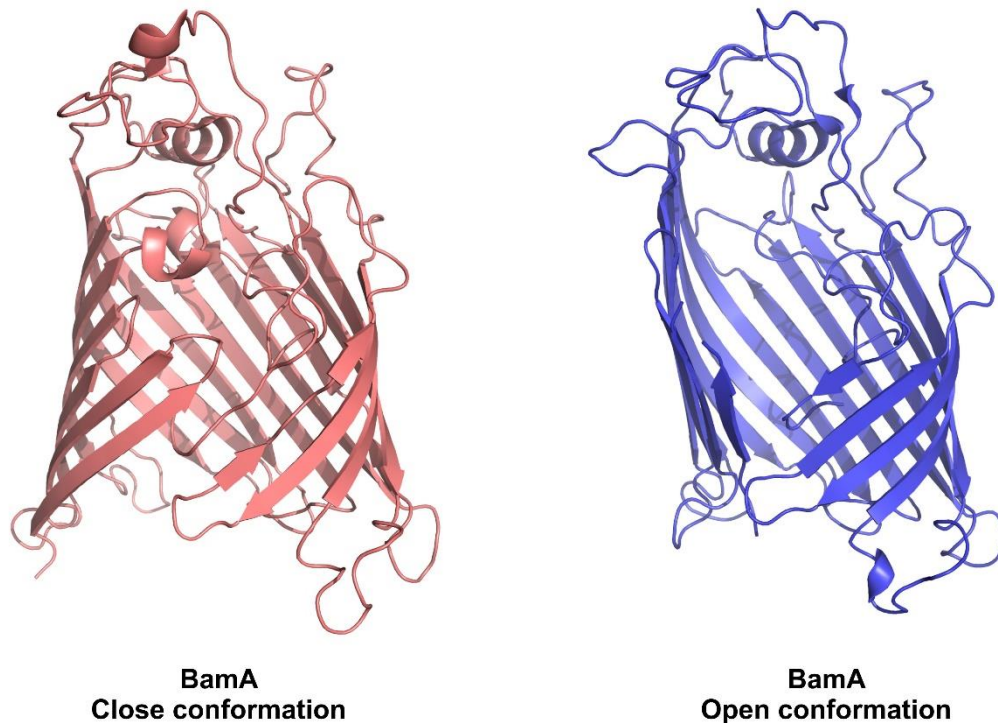
Figure 1.6 Close and Open BamA beta-barrel crystal structure conformations. Left; Close form: PDB 5ayw and Right; Open form: PDB 5ekq. The rotational movement of the first eight strands are observed by comparing close and open forms of the beta-barrel. These conformational rearrangements evidently translate to the conformational changes of the POTRA domains, specifically POTRA-5 (not shown here) (Bakelar et al., 2016; Gu et al., 2016).

1.6.2 BAM complex invokes the spatio-temporal organization of outer membrane constituents.

Discovering membrane heterogeneity through various microscopy experiments have challenged our preconceptions on bacterial cell envelope organization. The "OMP islands" observed by Rassam *et al*., revealed that the BAM complex is co-localized with other substrate OMP clusters (at least, in this case with BtuB and Cir) and remained this way as they diffuse towards cell poles during cell growth and elongation (Rassam et al., 2015).

While these clusters could potentially harbour several other BAM substrates, they may also carry LPS molecules, the most abundant OM constituent. In fact, BAM complex is known to insert LptD, a key element in assembling LPS at the cell surface (Bennion et al., 2010). Reciprocally, LPS is known to facilitate efficient folding of OMPs, such as PhoE (de Cock and Tommassen, 1996). Spatial clusters centering BAM can also cater for biogenesis of various lipoproteins as evident from BamC co-localization within these OMP islands (Rassam et al., 2015). Therefore, it seems that the BAM complex is found at the crossroads of biogenesis pathways of major outer membrane components.

As evident from the heterogeneous localization of a number of different OMPs mentioned in previous sections, the current paradigm of OMP localization follows discrete bursts of OM material insertion events concentrated at the mid-cell region or at random sites throughout the cell surface (Smit and Nikaido, 1978; Wang et al., 2008; Ursell et al., 2012; Rassam et al., 2015). This presumably relates to the number and location of active BAM complexes, which serve to catalyse β-barrel protein assembly into the outer membrane (De Geyter et al., 2016; Plummer and Fleming, 2016; Noinaj et al., 2017). Together, these evidence point towards a model where the BAM complex plays a crucial role, not only in the biogenesis of bacterial cell envelope, but also fashioning the localization characteristics of all major OM constituents.

1.6.3 Outer membrane localization of autotransporters via the BAM complex.

While the picture emerging from BAM at the centre governing spatio-temporal organization of membrane materials is certainly appealing, it also brings into question whether all BAM substrates display similar spatial characteristics when they are inserted at the OM.

Autotransporters (AT) are one of the largest families of secreted proteins in gram-negative bacteria displaying a variety of functions involving pathogenicity (Pallen et al., 2003). In general, AT proteins contain an N-terminal extracellular domain which carries the pathogenic effector function, and a C-terminal beta barrel (autochaperon) domain that resides in the outer membrane (Henderson et al., 2004). Later studies demonstrated the BamA involvement in membrane insertion of autotransporters, suggesting that all ATs are substrates of the BAM complex (Ieva and Bernstein, 2009). While it is tempting to think like other BAM substrates ATs should also follow similar spatial characteristics when they are inserted to the OM, a mounting amount of evidence suggests otherwise. ATs from a wide variety of rod-shape bacteria, including AIDA-I of *E.coli*, IcsA and SepA of *Shigella flexneri*, BrkA of *Bordetella pertussis*, and BimA of *Burkholderia thailandensis*, have been reported to be directly localized to bacterial cell poles when translocated to the cell surface (Charles et al., 2001; Jain et al., 2006; Lu et al., 2015). Indeed, when IcsA, SepA and BrkA were expressed in *E. coli* system, they still migrated to the poles, suggesting there are intrinsic features within the autotransporters programmed to be localization to the cell poles (Jain et al., 2006). Insertion of polarly localized ATs suggest that BAM complex should be actively participating in the assembly processes even at cell poles. This is a mere deviation from Rassem *et al.*, model where BAM complex becomes inactive at cell poles (Rassam et al., 2015). Conversely, at least one autotransporter, Ag43, was localised as covering the whole cell surface without any concentration towards poles (Danese et al., 2000; Kjærgaard et al., 2000). It is important to note that none of these studies have addressed where the integration event took place, nor any dynamics of movement of the autotransporters, but rather visualized their steady-state positioning.

1.7 Thesis outline.

The BAM complex of bacteria is essential for cell viability; it forms the central hub of bacterial outer membrane protein assembly where the transport pathway delivers a number of different proteins to the cell surface. Despite numerous structural biological evidence gathered through crystallography, a gap of knowledge still prevails regarding the protein assembly mechanism deployed by the BAM complex *in vivo*. For instance, in the absence of any potential energy source in the periplasmic space, how does the BAM complex catalyse nascent beta-barrel protein assembly and insertion into the outer membrane? Does a destabilised outer membrane alone can sufficiently provide energy to drive this series of complex events? Are there any plausible mechanisms that have been overlooked?

In this study, I attempted to shed light on some of these unanswered questions through studying the spatio-temporal organization of the BAM complex *in vivo*. To demonstrate, I have used two biological approaches;

(1) Utilizing single molecule localization super resolution microscopy to survey nanoscopic spatio-temporal organization of the BAM complex on *E. coli* cell surface (Chapter 3).

(2) Employing site specific *in situ* photo-crosslinking and cysteine mediated disulphide crosslinking in *E. coli* to determine possible oligomeric states of the BAM complex mediated through its enigmatic subunit BamB which may facilitate more efficient assembly of substrate proteins into the outer membrane (Chapter 4). Essentially, this section attempts to provide more mechanistic insights to the research findings listed in the previous chapter.

Chapter 2, highlights the materials and methods used in super resolution microscopy experiments and *in situ* photo-crosslinking, cysteine mediated disulphide crosslinking experiments in *E. coli* systems.

Chapter 5, introduces a new model for populating beta-barrel proteins into the outer membrane via the BAM complex.

Chapter 2: Materials and Methods

This section categorically lists the general and unique protocols used throughout the thesis. Section 2.1 highlights the optimization carried out for Super resolution microscopy experiments using *E. coli*. Section 2.2 illustrates the protocols employed for protein detection and *in situ* crosslinking experiments. The specific conditions used for the experiments were indicated in the results section in the form of text, figures or in figure legends as appropriate.

2.1 Materials and Methods: Super resolution microscopy.

2.1.1 Bacterial strains and plasmids.

Unless otherwise stated, *E. coli* was grown in LB (1% tryptone, 0.5% yeast extract and 0.5% NaCl) medium containing appropriate antibiotics as necessary (100 mg/ml ampicillin, 30 mg/ml kanamycin and 50 mg/ml chloramphenicol).

All imaging experiments were performed on *E. coli*-K12 BW25113 and isogenic mutants. Isogenic deletion mutants (Δ*bamB*) of *E. coli*-K12 BW25113 were obtained from the Keio collection (Baba et al., 2006) and were validated by PCR, to be certain that the deletion strains contained the kanamycin resistance cassette within the open-reading frame of interest. Plasmids and primers used in this study are described in Table 2.2 and Table 2.3 respectively.

2.1.2 Super resolution imaging: Direct stochastic optical reconstruction microscopy (*d*STORM) setup.

Super Resolution (SR) images were recorded on a custom built *d*STORM (Whelan et al., 2014) using an Olympus IX-71 base equipped with the appropriate fluorescence filter

cubes, 488nm Toptica laser (200mW), 561nm Quantum laser (500mW), 638nm Oxxius laser (150mW), UPlanSApo UIS2 oil-immersion 100x NA 1.4 objective,1.6x magnification changer engaged and an Andor iXon Ultra 897 High Speed EMCCD camera with single photon sensitivity for single molecule detection (Figure 2.1). The final excitation steering mirror and beam expansion lenses were mounted on a translation stage for free adjustment of the HiLo (Highly inclined laminar optical) angle. The system was operated at a HiLo angle appropriate for the respective sample to concentrate excitation power and reduce background fluorescence. Samples were mounted on a manual x,y translation stage to minimize sample drift.

Figure 2.1 Custom build *d*STORM set-up at Monash Micro Imaging facility. The set-up includes Olympus IX-71 base (left image) equipped with the appropriate fluorescence filter cubes (right image) and a high speed EMCCD camera with single photon sensitivity for single molecule detection.

2.1.3 Selecting suitable fluorophores for single colour *d*STORM imaging.

In the presence of thiol compounds such as 2-aminoethanethiol (MEA) or glutathione (GSH) synthetic organic fluorophores become photo-switchable, in which the fluorescence quenching occurs through the formation of a stable non-fluorescent (OFF) state (Heilemann et al., 2009b; Endesfelder et al., 2011). In the applications of single molecule localization microscopy (SMLM), the emitter, apart from being photo-switchable, should also exhibit high brightness or exert a considerably high photon flux for single molecule detection with relatively high localization precision. In addition, it should also display a

low duty cycle (Dempsey et al., 2011). Carbocyanine dye Alexa Flour® 647 is documented to be vastly superior to any other dyes in all the above mentioned characteristics (Heilemann et al., 2005; Rust et al., 2006; Metcalf et al., 2013; Olivier et al., 2013). Thus Alexa Flour® 647 fluorescent dye was used in my super resolution microscopy experiments.

2.1.4 Sample preparation for *d*STORM.

Cells were grown to mid-log phase (O.D. $_{600}$ ~ 0.6) in LB media (Miller) at 37°C with shaking (200 rpm) in Erlenmeyer flasks. Aliquots (500 µL) of cells were collected by centrifugation (4000x g, 5 min, 4°C) and washed twice in PBS before being resuspended in 500 µL of PBS. The cover glass bottom chambers of 8-well plates (Sarstedt®) were coated with 0.01% (v/v) poly-L-lysine (Sigma-Aldrich®) for 10 min at room temperature before excess poly-L-lysine was removed. Afterwards, 200 µL of *E. coli* cells were immobilized in to each coated well chamber. To ensure the formation of a monolayer of bacteria, chamber slides were centrifuged (4000x g, 3 min, 4 $^{\circ}$C) and the excess cell suspension was removed and washed three times briefly with PBS. The monolayer of bacteria was then fixed with a mixture of paraformaldehyde (2% w/v) and glutaraldehyde (0.2% v/v) in PBS for 5 min at 4°C followed by PBS washing steps to remove excess fixatives. Auto-fluorescence was minimized by neutralizing Schiff's bases caused by the glutaraldehyde treatment with the addition of freshly prepared 0.1% (w/v) $NaBH_4$ dissolved in PBS for 15 min, followed by two washing steps with PBS (Clancy and Cauller, 1998). Where applicable the samples were permeabilized either with Digitonin (0.001% or 0.01% w/v in PBS) or TritonX-100 (0.001% or 0.01% v/v in PBS) followed by three washing steps with PBS.

2.1.5 *d*STORM samples immunofluorescent labelling.

The specificity of the anti-BamC antibody was confirmed by the absence of a signal on Δ*bamC* mutants in western blots and in immunofluorescence microscopy (Figures 2.2). The specificity of anti-BamA antibody was confirmed by observing BamA levels expressed in *E. coli* (MC4100A) BamA depletion strain (Dunstan et al., 2015) and by failure to produce fluorescence signal on live *E. coli* cells (Figure 2.3). The Table 2.1 lists the primary and secondary antibodies used in this study. Blocking of non-specific binding sites was achieved with incubation in 5% w/v BSA in PBS for 1 h at room temperature, followed by incubation of antisera diluted to 1:1000 in 5% w/v BSA in PBS, for 1 h mixing by rotary inversion at room temperature. The primary antibodies were then removed and the wells were washed twice with PBS followed by addition of secondary anti-mouse/anti-rabbit IgG-Alexa-647 (ThermoFisher®) conjugated antibody (diluted 1:1000 in 5% BSA in PBS) for 45 min at room temperature. The secondary antibody was then removed and the wells were washed twice with PBS before the samples were stored at 4°C in PBS prior to microscopy imaging.
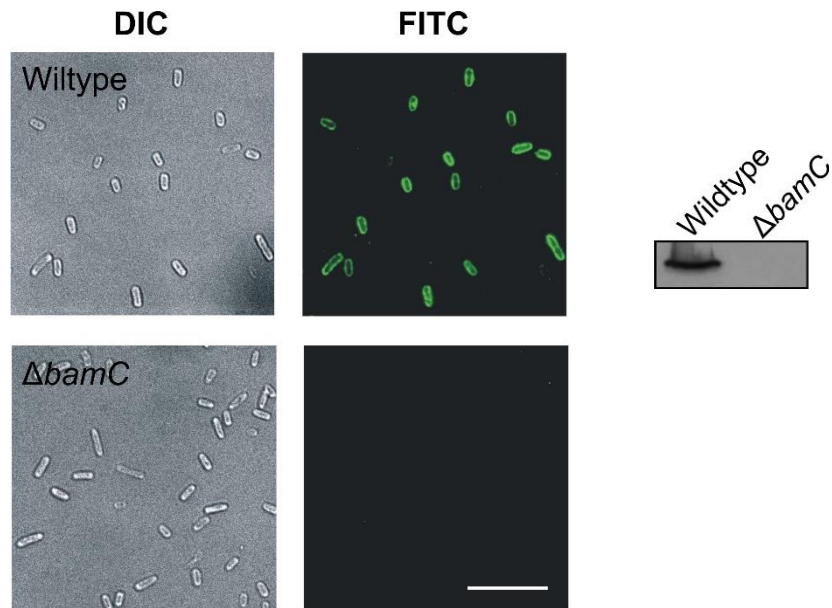
Figure 2.2 Immunofluorescence assessment of *E. coli* BW25113 using antibodies recognizing the C-terminal domain of BamC. At left, the differential interference contrast (DIC) image for a representative field of cells and at the right is the fluorescence image (FITC filter) of antibody staining. Also shown is a control experiment from an isogenic Δ*bamC* mutant strain that lacks BamC. Scale bar 10 μm. In the right, also showing a western blot with whole cell lysates from wildtype and Δ*bamC* mutant, immunostained with anti-BamC antibody.
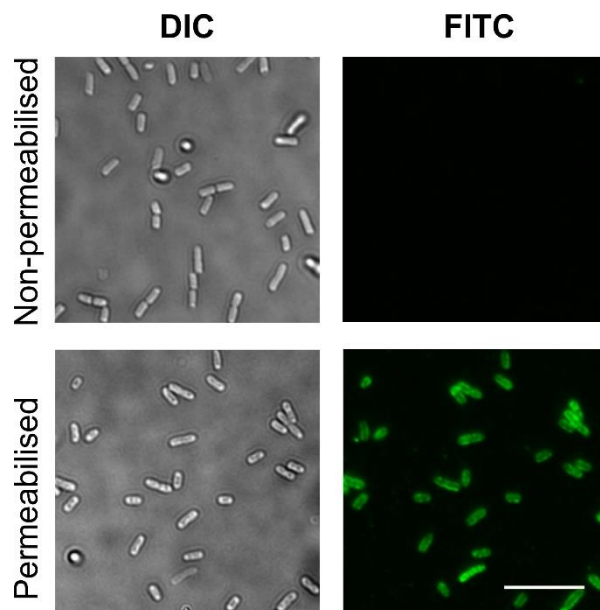
Figure 2.3 Immunofluorescence assessment of *E. coli* BW25113 using antibodies recognizing the N-terminal POTRA domain of BamA. At left, the DIC image for a representative field of cells and at the right is the fluorescence image (FITC filter) of antibody staining. Samples in the upper panels represent intact cells. The lower panel cells were fixed and permeabilized using 0.001% TritonX-100 (see methods section for permeabilization protocol). Scale bar 10 μm.

2.1.6 *d*STORM sample imaging buffer preparation.

Super resolution imaging on Alexa-647 labelled samples was performed in an imaging buffer consisting of TN buffer (50 mM Tris-HCL, pH 8.0, 10 mM NaCl), the oxygen scavenger system GLOX (0.5 mg/mL glucose oxidase; Sigma-Aldrich-G2133, 40 ug/mL catalase; Sigma-Aldrich-C-100 and 10% glucose) and 10 mM MEA (Sigma-Aldrich-M6500). MEA was made as a 1 M stock solution in 50 mM Tris buffer with pH adjusted to 8.0 using KOH.

2.1.7 *d*STORM image acquisition and processing.

Super resolution images collected for the Alexa-647 labelled samples were illuminated continuously with 638 nm laser at an appropriate HiLo angle. After an initial period of < 30 s to drive dyes into the dark state, single molecule blinking time series were acquired for 10,000 frames at an exposure time of 20 ms and an electron multiplying gain of 50 (Figure 2.4). Raw image pixel size with 100x objective and 1.6x magnifier engaged is 100 nm x100 nm.

The acquired data was reconstructed to super resolved images with an out-put pixel size of 10 nm using the open-source software rapi*d*STORM version 3.3.1 (Wolter et al., 2012). Full width of half maximum (FWHM) of the fitting point spread function was set at 350 nm and fitted point spread functions (PSF) with a local signal-to-noise ratio (SNR) < 120 were discarded. Images were first colour coded for temporal appearance of blinks to detect sample drift, then (if applicable) corrected for drift using the linear drift correction available in rapi*d*STORM and exported as 8-bit greyscale images for further image processing. The corresponding localisations files for the SR images were extracted from rapi*d*STORM listing all detected localisations in x,y coordinates for quantification and data analysis.
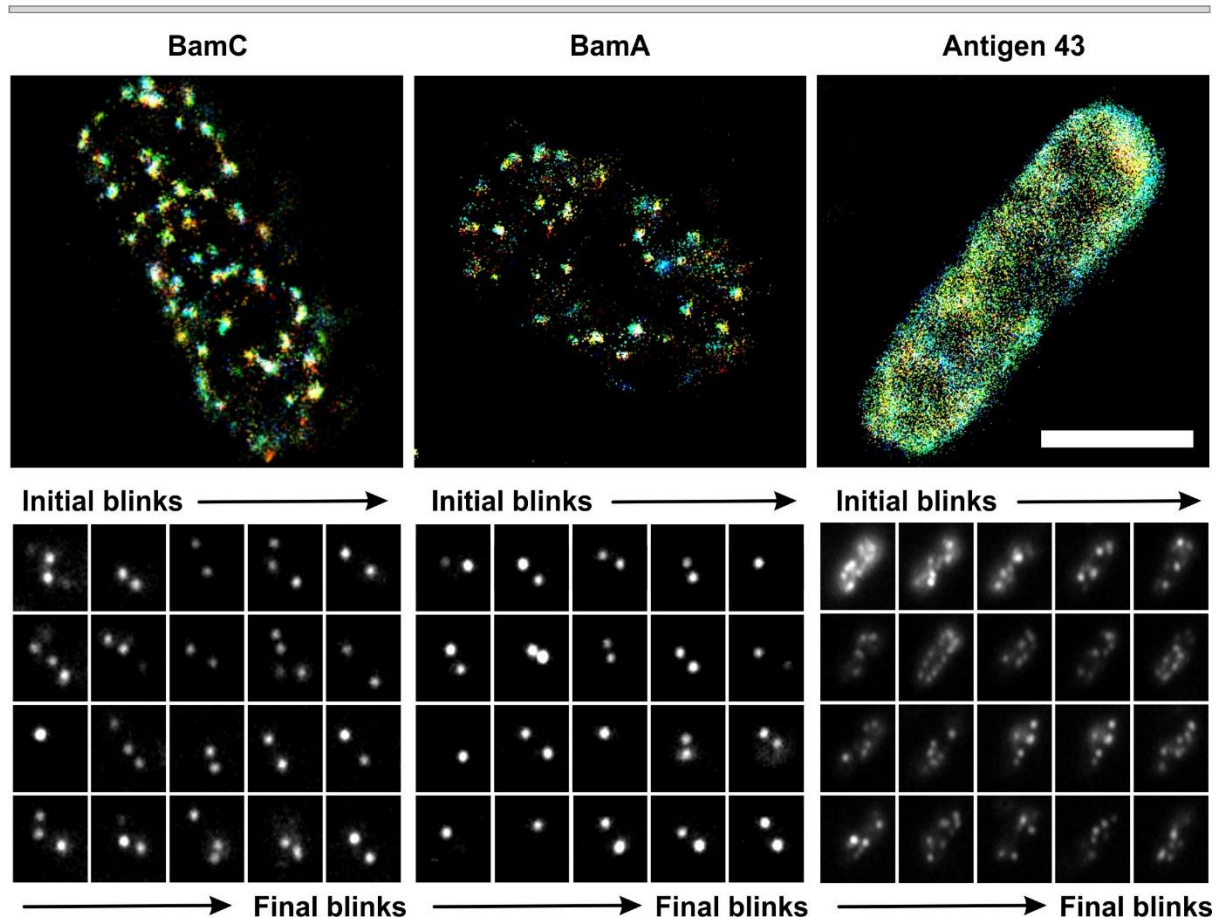
Figure 2.4 Photoswitching events captured through *d*STORM. RapidSTORM reconstructed super resolution images and the corresponding photoswitching events or "blink files" generated for BamC, BamA and Ag43 respectively. Spatially well separated localization events were acquired for 10,000 frames at an exposure of 20 ms. Scale bar 1 μm.

2.1.8 Cluster analysis of Super resolution images.

Cluster analysis of the BAM complex super-resolution data was performed according to the method described by Owen *et al* (Owen et al., 2010). Molecule coordinates from each image were exported from rapi*d*STORM (Wolter et al., 2012) as a text file and imported into the statistical analysis environment R (Ihaka and Gentleman, 1996). These were used to generate Planar Point Pattern (PPP) objects using the *spatstat* package (Baddeley and

Turner, 2005). Cluster analysis was performed in a Region of Interest (ROI) contained to membrane areas parallel to the cover slip to avoid 3D artefacts. ROIs were drawn on reconstructed super-resolution images using the polygon ROI tool in ImageJ (Abràmoff et al., 2004) and the coordinates of the polygon were exported to a tab-delimited file. ROI coordinates were then imported into R and used to create a polygonal *spatstat* window to isolate localisations falling within the ROI.

To analyze overall clustering in a given ROI, Ripley's K-function analysis was performed using the *spatstat Kest* function as:

$$\mathrm{K}(r) = \frac{1}{\lambda^2 A} \sum_{i=0}^{n} \sum_{j \neq i}^{n} \delta_{ij} e(x_i, x_j; r) \quad \text{where} \quad \delta_{ij} = \begin{cases} 1 & if \quad d_{ij} \leq r \\ 0 & if \quad d_{ij} > r \end{cases}$$

dSTORM analysis equation 1

where r is the spatial scale radius, A is the area of the analysis Region of Interest (ROI), λ is the density of localisations, d_{ij} is the distance between two points i and j, and $e(x_i, x_j; r)$ is the edge-correction weighting. Ripley's isotropic edge-correction weighting, as implemented in the *spatstat* package, was used for all analyses in this study.

The Ripley's K-function is defined such that $\lambda \mathrm{K}(r)$ gives the average number of localizations within a circle of radius, r, for a typical point in a point distribution. Under complete spatial randomness (or Poissonian distribution of points), the expected number of localizations within a circle of radius, r, is therefore given by $\lambda \pi r^2$ (i.e., the density of points multiplied by the area of the circle). Hence,

$$\mathrm{K}_{pois}(r) = \pi r^2$$

_d_STORM analysis equation 2

The scaling of $\mathrm{K}(r)$ is dependent upon the area of the enclosing circle (i.e., exponential with respect to r), therefore $\mathrm{K}(r)$ is often transformed to scale linearly with respect to r, yielding the L-function (also known as Besag's transformation):

$$L(r) = \sqrt{\frac{\mathrm{K}(r)}{\pi}}$$

_d_STORM analysis equation 3

Given **Equation 3**, random point distributions have an $L(r)$ equal to r at all values of r. Thus, $L(r)$ distributions in this study have been plotted as $L(r) - r$ versus r, where a random distribution coincides with the x-axis of the plot. A positive $L(r) - r$ value at a given r indicates clustering at that spatial scale, while a negative value indicates a regular distribution or spreading at that spatial scale. Peaks in the $L(r) - r$ distribution indicate the spatial scales at which the highest degree of clustering is observed. A $L(r) - r$ value equal to zero indicates a random distribution of points.

For the generation of cluster maps, the clustering around each detected localization was explored using Getis and Franklin's local version of the Ripley's K-function (Getis and Franklin, 1987);

$$L(r)_i = \sqrt{\frac{A\sum_{j=0}^{n}\left(\dfrac{\delta_{ij}}{n}\right)e\left(x_j, y_j; r\right)}{\pi}} \quad \text{where} \quad \delta_{ij} = \begin{cases} 1 & \text{if} \quad d_{ij} \leq r \\ 0 & \text{if} \quad d_{ij} > r \end{cases}$$

_d_STORM analysis equation 4

In our analyses, a spatial scale $r = 40$nm was used for all analyses. In order to resolve all clusters, this value was set below the r value at which the $L(r)$-r distribution peaked in the overall Ripley's K analysis for BamC, BamA and other proteins described in this study.

A quantitative, pseudo-coloured cluster 'heat' map was then generated by interpolating a surface across the local $L(40)$ values in each analysis ROI using a 10 nm grid and 'v4' surface interpolation algorithm in Matlab. Cluster heat-maps were thresholded at a $L(40)$ value of 69.28 to generate binary cluster maps. This threshold value equates to 3 times greater local molecular density at a spatial scale of $r = 40$ nm compared to a random distribution of points of the same density.

A marker assisted watershed transform was then used to split clusters that were touching each other ('clumped') using the watershed function of the *imager* R package. To determine markers for the watershed transform, a peak picking algorithm was developed to isolate the coordinates of localizations with peak $L(40)$ values i.e., those surrounded by the highest density of other localizations. Briefly, in order for a localisation to be considered have a peak $L(40)$ value, its $L(40)$ value needed to exceed the cluster threshold specified above by at least 10% and be greater than all other localizations within a circle of $r = 24$ nm. Following watershed splitting, objects smaller than 1000 nm² were excluded. Cluster density, nearest neighbor distances (i.e., the distance from the centre of a

cluster to the center of its nearest neighboring cluster) and the proportion of localizations inside clusters were measured using remaining objects. All cluster objects touching the ROI were excluded for measurements of cluster size and diameter, since these could be cropped by the ROI. Source code for an automated version of the cluster analysis procedure described here is hosted as a Git repository and is available at https://github.com/monashmicroimaging/autoclustr.
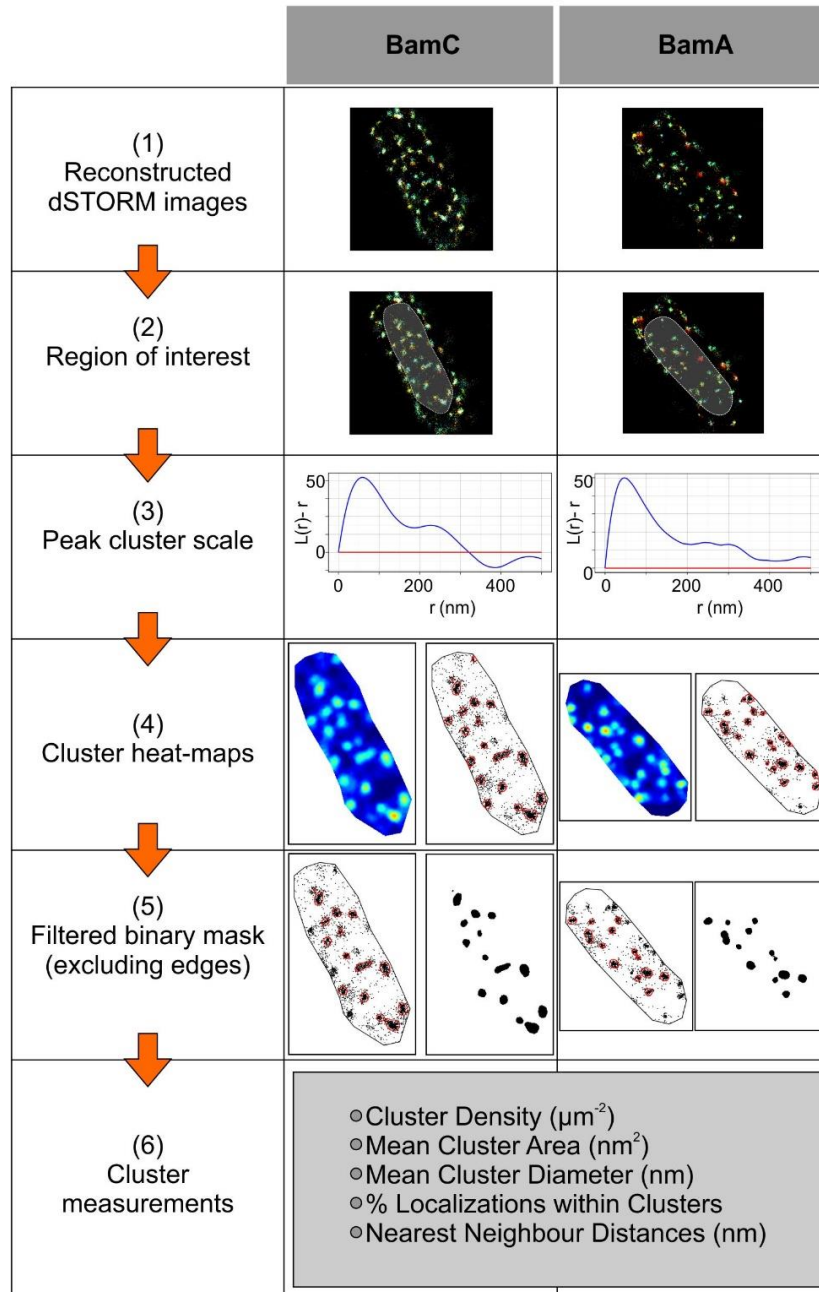
Figure 2.5 Cluster analysis flow chart. (1) Bacteria *d*STORM image is reconstructed from the raw data using rapidSTORM software and all detected localizations are extracted. (2) A region of interest (ROI) is drawn excluding the outer edges to prevent edge effects due to the curvature of the bacterial cells. (3) From all localizations within the ROI a linear version of the Ripley's K function, L(r)-r vs r, is calculated and plotted against the radius r. (4) A cluster heat map is generated over all localizations within the ROI. (5) Using adequate thresholding based on the L(r)-r vs r graph a cluster mask is derived from the heat map. The cluster mask is filtered for clusters at the edge of the ROI to exclude cropped clusters. (6) From the filtered mask additional cluster characteristics such as cluster density, average cluster size, average cluster diameter, proportion of localizations within the clusters and nearest neighboring cluster distances can be calculated. Representative examples are shown for cells stained with anti-BamC and anti-BamA.

2.1.9 3D single molecule localisation microscopy setup, image acquisition and processing.

3D STORM super-resolution imaging was performed on a Vutara SR 350 system (Bruker®) equipped with 4 imaging laser lines (488 nm, 560 nm, 640 nm and 750 nm, all 1 W laser power), one activation laser (405 nm, 100 mW), 60x oil immersion objective, sCMOS Hamatasu Camera Orca Flash 4.0 and quad field module (Orange/Red) for 3D imaging using the biplane approach (Juette et al., 2008; Mlodzianoski et al., 2009). Appropriate PSF calibration files were recorded at the start of each day using multi-colour fluorescent beads.

All dyes were first pumped into the dark state at a laser power of 11 kW/cm^2, the laser power was kept at 11 kW/cm^2 during the imaging process, individual dye molecules were reactivated with low amounts of 405 nm laser light (25 W/cm^2), 405 nm laser power was increased in 25 W/cm^2 intervals over the imaging time to keep the number of detected blinks at approximately the same level. 100 frames were taken for each z-slice (2-3 z-steps), with 20-25 repeats at an exposure time of 10-20 ms. 3D super-resolution image reconstruction was performed using the Vutara 350 SRX Software, where the background threshold was set to 10, a confidence value of 0.8 and the particle size set to 50 nm diameter, which is approximated to the minimum size of primary-secondary antibody complex. Images are displayed with colour relevant to z-depth.

2.1.10 *E. coli* Antigen 43 and LPS fluorescent labelling for biological cluster controls.

Biological cluster controls were used to validate and optimise Cluster analysis procedure. For this purpose, *E. coli* samples were immunofluorescently labelled with anti-Antigen 43 and anti-LPS antibodies (Table 2.1). Both samples interrogated under *d*STORM imaging displayed dense surface coverage in *E. coli* and lacked subtle structural variations such as clusters (Figure 2.7). These super resolution images were then subjected to cluster analysis calculations (see 2.1.8).
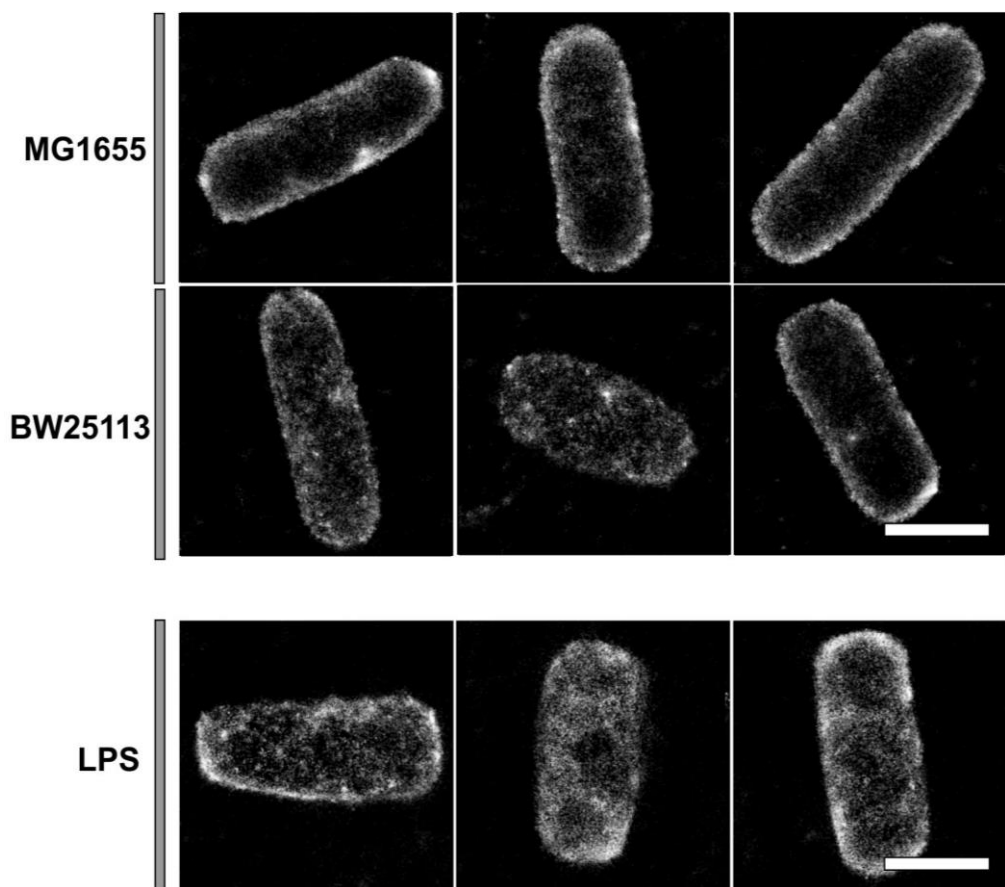
Figure 2.7 *d*STORM images of anti-Ag43 and anti-LPS labelled *E. coli* cells. Super resolution images for Ag43 and LPS distribution showed dense surface coverage lacking distinct structures in the cell surface.

2.1.11 *d*STORM Optimization of imaging different focal planes of *E. coli* cells.

Anti-Ag43 immunostained *E. coli* cells were used to optimise the detection of different focal planes of bacterial cells imaged through *d*STORM. Intensity profiles generated for each focal plane was used to identify the top most layer of bacteria cells (approximated 2D outer membrane).

A.

Top

Bottom

Chamber slide

Top view

Top
Bottom

Bottom view

Y Primary antibody

Y Secondary antibody

▮ Outer membrane

▯ Inner compartments (cytoplasm, inner membrane and periplasm)

B.

Focal Plane

Sample
Cover slip

Top

Middle

Bottom
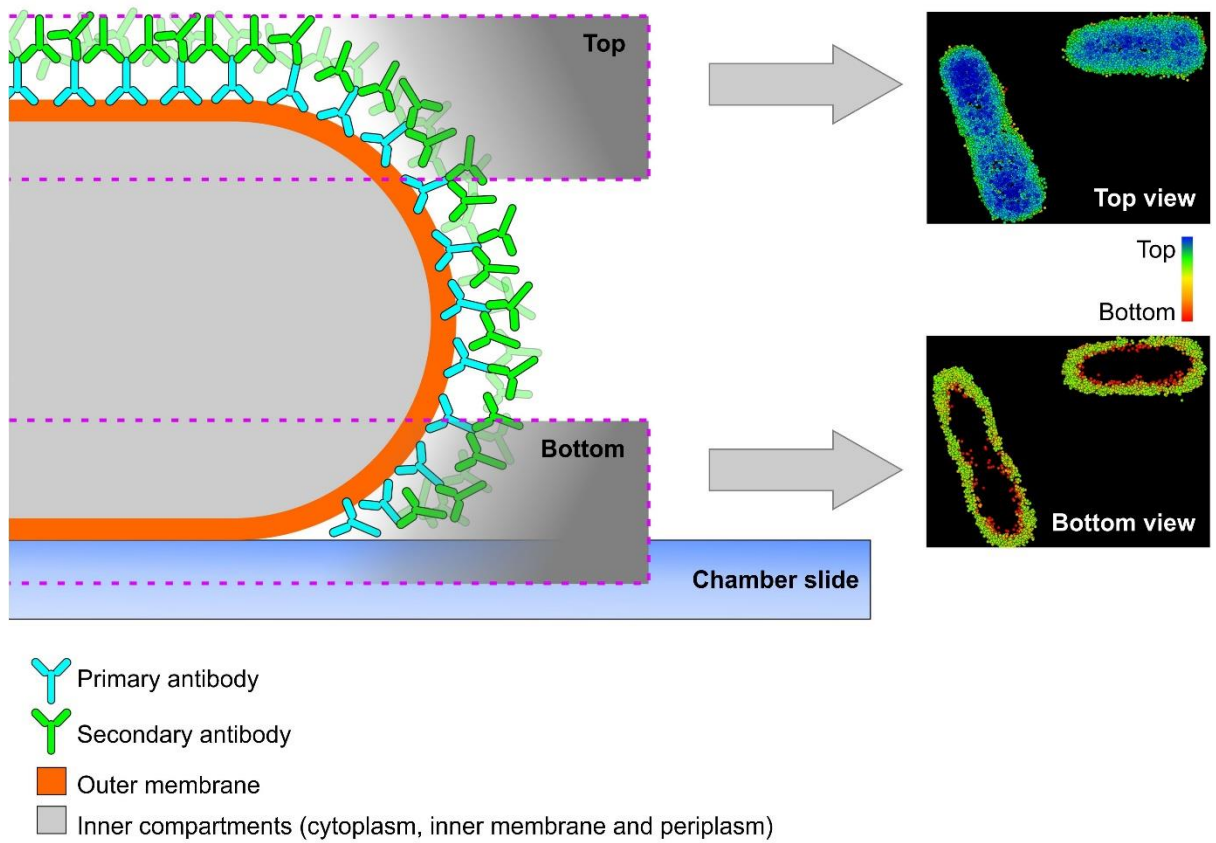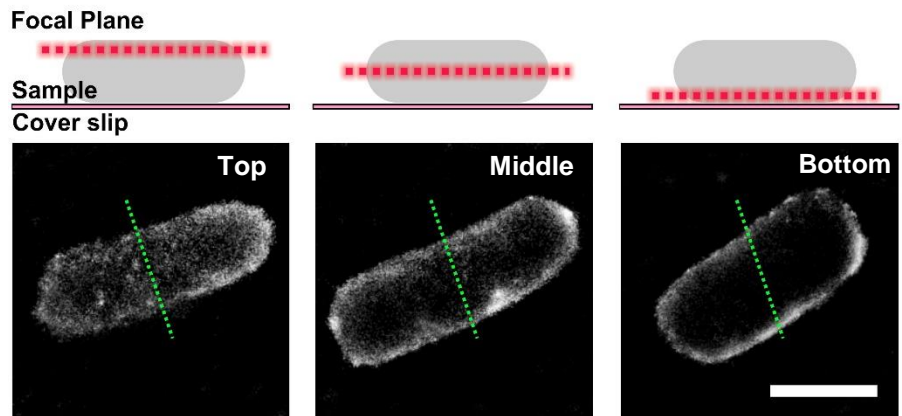
Intensity Profiles (Gray Value)

200
150
100
50
0
0   400   800   1200
Distance (Pixel)

200
150
100
50
0
0   400   800   1200
Distance (Pixel)

200
150
100
50
0
0   400   800   1200
Distance (Pixel)
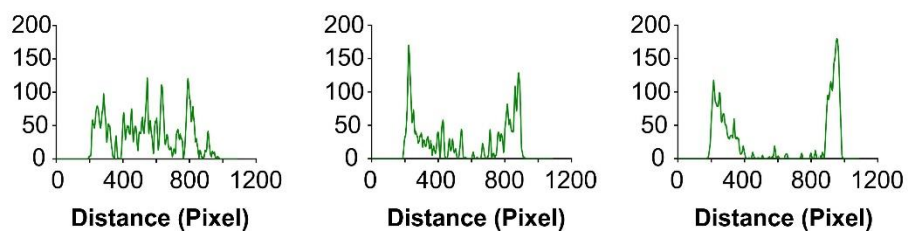
Figure 2.8 *d*STORM imaging of the bacterial outer membrane. (A) Antibody accessibility to membrane surfaces is depicted for an *E. coli* cell. Cut-away section shows antibody access to the outer surface of the outer membrane. For the purpose of clarity, the inner compartments of the cell (periplasm, inner membrane and cytoplasm) are not distinguished. Idealized "top" and "bottom" planes are depicted. The inset figures show actual images of *E. coli* stained with antibodies to Ag43, which correspond to profiles expected for idealized layers, based on the colour profiles from top (blue) to bottom (red). "Top section" images were used for all *d*STORM imaging analysis in this study. **(B)** Anti-Ag43 immunostained *E. coli* cells were used to optimise the detection of different focal planes of bacterial cells and imaged through *d*STORM. Intensity profiles were generated for each focal plane (Left to right; Top, Middle and Bottom focal planes respectively). The highest average Gray values were acquired for Top focal plane and were used for all *d*STORM imaging analysis in this study. Scale bar 1 μm.

2.1.12 Proteinase K assay.

Protease shaving of bacterial cells followed a published procedure (Clements et al., 2009), with the following modifications. *E. coli* BW25113 cells were grown to mid-log phase (O.D. $_{600}$ ~ 0.6) in LB, and 50 μL aliquots were harvested by centrifugation (5 min, 4000 x g) before resuspending the cell pellet in 500 μL of TBS. Digitonin (0.001 % final concentration) and polymyxin B (500 μg/ml final concentration) were added to cells as required and incubated at 4 °C on a rotary wheel for 15 min. Proteinase K (200 μg/ml) was subsequently added to cells and incubated at 4 °C for up to 60 min. At the indicated time points trichloroacetic acid (10% final concentration) was added and samples were incubated on ice for 30 min. Protein pellets were washed twice with 100% acetone (20 min, 25,000 X g), air dried and resuspended in 50 μl of SDS-sample buffer. Samples (35 μL) were analyzed by SDS-PAGE and immunoblotting for BamA (1:10,000), BamC (1:20,000), BamD (1:20,000) and SurA (1:10,000) (Figure 2.9).

–	+	+	+	+	+	Proteinase K
0	0	15	60	15	15	Time (min)
–	+	+	+	–	–	Digitonin
–	–	–	–	+	–	Polymyxin B
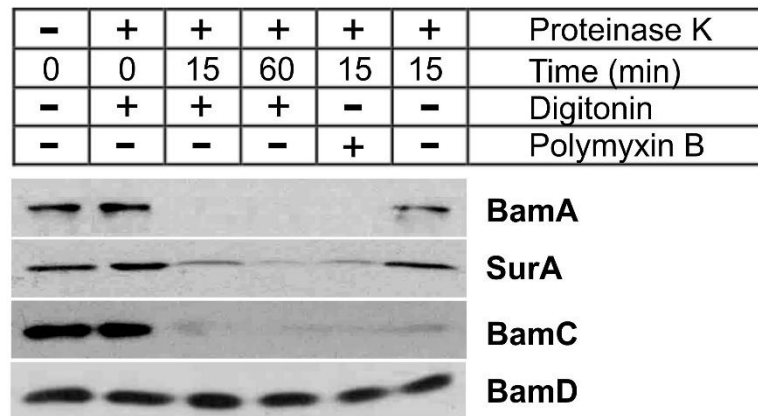
Figure 2.9 Proteinase K assay to optimise detergent permeabilization. *E. coli* BW25113 were treated with buffer or with buffer containing 0.001% (w/v) digitonin, and subjected to treatment with exogenously added Proteinase K for either 15 min or 60 min as indicated. Access of the protease into the periplasm was monitored by SDS-PAGE and immunoblotting with antisera recognizing the surface domains of BamC, the periplasmic POTRA domains of BamA or the periplasmic chaperone SurA. As a control, one sample was treated with polymixin B, a validated compound for solubilizing the outer membrane to proteinase K.

2.1.13 BAM substrate overexpression by Antigen 43.

E. coli BW25113 wild-type cells transformed with pCO2 plasmid (table 2.0) containing the *flu* gene under arabinose inducible promoter (Klemm et al., 2004), was grown in LB media at 37°C with vigorous shaking (200 rpm) till O.D$_{600}$= 0.3 and was induced by the addition of 0.2% L-arabinose. Culture was further incubated at 37°C till the mid-log phase was reached. Overexpression of Antigen 43 was apparent at cellular level with the observed high level of auto-aggregation present in cells and subsequent sedimentation in liquid culture media. Cell culture was pelleted followed by sample preparation for *d*STORM imaging described in section 2.1.4.

2.2 Materials and Methods: *In situ* photo-crosslinking and disulphide crosslinking experiments.

2.2.1 Bacterial strains and plasmids.

Unless otherwise stated, *E. coli* was grown in LB (1% tryptone, 0.5% yeast extract and 0.5% NaCl) medium containing appropriate antibiotics as necessary (100 mg/ml ampicillin, 30 mg/ml kanamycin and 50 mg/ml chloramphenicol). Plasmids and primers used in this study are described in Table 2.2 and Table 2.3, 2.4.

For *in situ* photocrosslinking studies using p-benzoyl-L-phenylalanine (BPA)-expressing alleles of *bamB* required a vector pGEM®-T Easy, where the *bamB* open-reading frame together with 500 bp upstream to include the native promoter elements was amplified by PCR using the primer pair SDG-BamB-Fw and SDG-BamB-Rv. The SDG-BamB-Rv primer was designed to incorporate sequence encoding a His$_6$-tag at the C-terminal end of the *bamB* open-reading frame for recombinant protein detection and Ni-NTA affinity purification purposes. The amplified DNA fragment was purified using the Wizard® SV Gel and PCR Clean-Up System (Promega-A9281) and then subjected to standard A-tailing procedure for blunt-end PCR fragments using *Taq* DNA Polymerase (NEB-M0273S). The A-tailed DNA fragment was then ligated into pGEM®-T Easy open vector. The ligated product, pGEM-T-*bamB-His$_6$*, was verified by DNA sequencing and correctly oriented clones were chosen for further use. BPA alleles were obtained by incorporating amber codons to pGEM-T-*bamB-His$_6$* construct using Quick-change site directed mutagenesis (amber codon primers are listed in Table 2.4). Amber codons were introduced at 40 positions in the *bamB* sequence; only 29 of these were viable for *in situ* photocrosslinking studies in *E. coli* strains. The plasmids encoding viable BPA-containing alleles of BamB

were transformed into the Δ*bamB* mutant stain (*E. coli* BW25113, Keio Collection) harbouring pSup-BpaRS-6TRN (Ryu and Schultz, 2006).

The BamB disulphide mutants were constructed by introducing codons for Cys residues into the *bamB* sequence using Quick-change site directed mutagenesis (primers are listed in Table 2.3).

All other BamB mutant plasmids used in this study were made using Quick-change site directed mutagenesis protocol (primers are listed Table 2.3).

2.2.2 *E. coli* heat-shock transformation.

A 10 µl of the ligation reaction was heat shocked into chemically competent $CaCl_2$ *E. coli* (DH5α) by incubating on ice for 10 minutes. Then heat-shocked at 42°C for 90 seconds immediately followed by incubation in ice for 2 minutes. Afterwards recovered by adding 500 µl of Luria Broth and incubating at 37°C for ~ 1 hour. Cells were then plated onto LB agar plates containing the appropriate antibiotics and incubated overnight at 37°C. If sizeable colonies were not detected within the first 24 hrs, LB agar plates were incubated 30°C for further 24 hrs.

2.2.3 *E. coli* clone screening.

Clones were screened by picking individual colonies into 5 ml of Luria Broth containing the appropriate antibiotic, grown overnight at 37°C or 30°C and their plasmids extracted according Wizard® Plus SV Minipreps DNA Purification protocol (Promega®). Orientation of the clone were tested using appropriate restriction endonuclease digestions. Positive clones were sequenced using the T7 promoter and SP6 primers by the Macrogen® sequencing company Korea. Correct clones were stored at –80°C by adding stationary phase cells to sterile glycerol at a final concentration of 15% (v/v).

2.2.4 Protein detection.

2.2.4.1 Sodium dodecyl sulphate–polyacrylamide gel electrophoresis (SDS-PAGE).

SDS-PAGE was performed under denaturing and reducing conditions. Stacking gels, constituting the upper 20% of the gel, contained 5% (w/v) acrylamide (Biorad Acrylamide:Bis-acrylamide 29:1), 125 mM Tris pH 6.8, 0.01% (w/v) SDS, 0.25 mM EDTA, 0.2% APS (w/v) and 0.1% (v/v) TEMED. Continuous separating gels containing either 14%, 12%, 10% or 8% (w/v) of acrylamide (Biorad Acrylamide:Bis-acrylamide 29:1), 0.375 mM Tris pH 8.8, 0.1% (w/v) SDS, 0.2% APS (w/v) and 0. 1% (v/v) TEMED was used. Gradient separating gels contained the aforementioned separating gel constituents except that an equal volume of acrylamide solutions (5% – 16% (w/v)) were poured using an SG50 Hoefer Gradient pourer in between two glass plates separated by a 0.75 mm spacer and comb. Protein samples were then denatured and disulphide bonds reduced by adding to SDS-PAGE sample buffer and heating to 95°C for 5 minutes prior to loading. The SDS-PAGE gel was fastened to an electrophoresis tank using metal clips. The upper and lower chambers were then filled with Tris glycine SDS-PAGE running buffer (Table 2.5). Samples were loaded into wells using a Hamilton syringe alongside a molecular weight standard (15-30 µl) (GE healthcare LMW-SDS marker kit). 50–100 volts (depending on the % of acrylamide used in the separator gel) was applied and samples were electrophoresed overnight. Proteins were either visualized by staining in Coomassie Blue stain (Table 2.5) with gentle agitation followed by subsequent washes in destain solution (Table 2.5) or detected by western blot as described below.

2.2.4.2 Western blot and immunodetection.

To identify specific proteins from complex cellular fractions, proteins separated by SDS-PAGE were immobilized onto a 0.45 µM polyvinyl difluoride (PVDF) or a 0.45 µM nitrocellulose membrane. Gels were sandwiched in the middle of two sponges and a piece of Whatman® blotting paper, pre-soaked in 0.5 x Western transfer buffer (Table 4.0), and an immobilizing membrane on the side facing the cathode and in direct contact with the gel. PVDF membranes were pre-soaked in 95% methanol prior to a buffer exchange with 0.5 x Western transfer buffer. The sandwich was then transferred to a wet transfer apparatus (Biorad) and electro blotting was performed for 1 hour at 1 amp (constant). Membranes were rinsed with Ponceau stain (Table 4.0) to visualize the molecular weight standards. Membranes were then blocked with 2–5% skim milk powder (w/v) in TBS-T (Table 4.0) for 1 hour, then probed with primary antiserum in 2–5% Skim milk powder (w/v) in TBS-T for 1 hour, washed 3 times in TBS-T then probed with the secondary anti-rabbit or anti-mouse conjugated to Horse-radish Peroxidase (HRP) for 30 mins followed by 3 washes in TBS-T. Proteins were detected by incubating the membrane with freshly mixed electrogenerated chemiluminescence (ECL) solution A and B (1:1) (Table 4.0) then visualized using a Fuji X-ray film and an automated film developer.

2.2.4.3 Sample preparation and protein mass spectrometry characterisation.

Protein was reduced and alkylated prior to an in-solution overnight trypsin digestion (Promega corp., Madison, WI, USA).Trypsin digests were analysed by LC-MS/MS using the QExactive mass spectrometer (Thermo Scientific, Bremen, Germany) coupled online with a RSLC nano HPLC (Ultimate 3000, Thermo Scientific, Bremen, Germany). Samples were concentrated on a 100 μm, 2cm nanoviper pepmap100 trap column with 95% buffer A (0.1% Formic acid) at a flow rate of 15 μl/min. The peptides then eluted and separated with a 50 cm Thermo RSLC pepmap100, 75 μm i.d., 100Å pore size, reversed phase nano

column with a 30 mins gradient of 90% buffer A (0.1% Formic acid) to 25-minutes to 30% B (80% Acetonitrile 0.1% formic acid) and to 40%B to 30 mins, at a flow rate of 300 μl/min. The eluent is nebulised and ionised using the Thermo nano electrospray source with a distal coated fused silica emitter (New Objective, Woburn, MA, USA) with a capillary voltage of 1900 V. Peptides are selected for MS/MS analysis in Full MS/dd-MS^2 (TopN) mode with the following parameter settings: TopN 10, resolution 17500, MS/MS AGC target 1e5, 60 ms Max IT, NCE 27 and 3 m/z isolation window. Underfill ratio was at 10% and dynamic exclusion was set to 15 s. Data from LC-MS/MS run was exported to Mascot generic file format (*.mgf) using proteowizard 3.0.3631 (open source software, http://proteowizard.sourceforge.net) and searched against Swiss-Prot databases using the MASCOT search engine (version 2.4, Matrix Science Inc., London, UK) with all taxonomy selected. The following search parameters were used: missed cleavages, 1; peptide mass tolerance, ± 10 ppm Da; peptide fragment tolerance, ± 0.02 Da; peptide charge, 2+, 3+ and 4+; fixed modifications, carbamidomethyl; Variable modification, oxidation (Met).

2.2.5 Isolation of total membrane fractions from *E. coli*.

A 5 ml overnight starter culture was grown in LB at 37°C from a single colony of *E. coli*. Starter culture was diluted to 1:100 in 400 ml of LB with appropriate antibiotics and was grown until stationary phase (OD$_{600}$ = ~1.0). Cells were pelleted by centrifugation (5 min, 5000 x g, 4°C). Pellet was resuspend in 10mM Tris, pH 7.5 (~200ml). Centrifugation step was repeated and the cell pellet was resuspend in 10 ml TS buffer (10 mM Tris pH 7.5, 0.75 M sucrose). Lysozyme (50 μg/ml) and PMSF (2 mM) was added to break down the peptidoglycan layer and inhibit host serine proteases respectively. EDTA (1.65 mM, pH7.5) was added to destabilise the outer membrane for cell lysis. Cells were broken down

using an Avestin Emulsiflex (2-3 passes at ~15,000 psi). After emulsification, the cell lysate was subjected to centrifugation (15,000 x g, 20 min, 4 °C) to remove any cell debris. The supernatant fractions were then subjected to ultracentrifugation (38,000 rpm, 45 min, 4°C, 70.1 Ti rotor) and pelleted the total membranes fractions at the bottom of the tubes. Membrane pellets were resuspended in 400 µL of TES buffer (3.3 mM Tris pH 7.5, 1.1 mM EDTA, 0.25 M sucrose) using a douncer. Finally, the total membranes fractions were snap freeze in liquid nitrogen for storage at -80 °C.

2.2.6 Blue Native-polyacrylamide gel electrophoresis (BN-PAGE)

2.2.6.1 Gradient gel preparation for BN-PAGE

Native protein complexes were resolved by BN-PAGE, essentially as previously described (Schägger and von Jagow, 1991) using 1.5 mm spacers and combs and gel plates. Stacking gels constituting the upper 20% contained 3.5% (w/v) acrylamide [Biorad (#161-0149) Acrylamide:Bis-acrylamide 37.5:1], in BN-PAGE gel buffer (1 x) (Table 2.5). Separating gels constituting the lower 80% of the gel contained a 6–12% gradient of acrylamide [Biorad (#161-0149) Acrylamide:Bis-acrylamide 37.5:1]. The acrylamide gradient made in BN-PAGE gel buffer (1 x) and equal volumes of each 5% and 16% acrylamide gel gradient solutions (~7 mL each), where the 12% acrylamide solution contained 10% (v/v) glycerol. The gradient was poured using a SG50 Hoefer Gradient pourer after the addition of 100 µl of 20% APS and 10 µl TEMED per 10 mL of gel solution (i.e. 0.2% APS and 0.1% TEMED final concentration). Gels were fastened to a gel tank using bull dog clips then pre-cooled at 4°C.

2.2.6.2 Sample preparation for BN-PAGE.

After determining the concentration of the total membrane isolates per gel lane (~ 10 μg), 10% of n-Dodecyl β-D-maltoside (DDM) was added to a detergent to protein ratio of 4:1. Afterwards, ACA750 buffer (750 mM amino caproic acid, 50 mM Bis-Tris pH 7.4, 0.5 mM EDTA) was added to a final volume of 20 μL. Total membrane isolates were then incubated for ~20 mins on ice. Finally, prior to BN-PAGE, 5 μL of 5 x Native PAGE loading buffer (Table 2.5) was added.

2.2.6.3 Electrophoresis conditions.

The BN-PAGE cathode buffer (Table 2.5) was gently overlaid on top of samples then BN-PAGE anode buffer (Table 2.5) was added to the bottom chamber. Protein complexes were then electrophoresed at 100 V overnight at 4°C. The next day once the dye front had entered the separating gel, the voltage was then turned up to 13 mA. To minimize the transfer of Coomassie brilliant blue G-250 onto the membrane during western transfer, when the dye front had reached ≥ half way down the separating gel, the cathode buffer was replaced with fresh cathode buffer lacking Coomassie brilliant blue G-250.

2.2.6.4 Western blot.

Protein complexes resolved by BN-PAGE were transferred to 0.45 μm PVDF by western blot as per 2.2.4.2, except for the following alterations i) 1x western transfer buffer instead of 0.5x was used, ii) gels were soaked in 1 x SDS-PAGE Tris-glycine running buffer for ~5 minutes prior to transfer, iii) protein complexes were transferred for 1.5 hours at 1 amp (constant) and marker proteins were visualized by briefly soaking the PVDF membrane in Coomassie blue stain then washed thoroughly with destain. Markers were traced onto the membrane then residual Coomassie was removed by rinsing in 100% methanol.

2.2.7 Bioinformatic methods.

2.2.7.1 Gene synteny predictions.

The protein sequence of the *E. coli* K-12 (MG1655) gene annotated as *bamB* (*yfgL*) was used to search the STRING v10.5 database for putative functional protein partners. The required confidence score was set at a medium confidence level (0.400). String line thickness represents the strength of the supporting data. The maximum number of interactions to display was set to no more than 10 for the 1st and 2nd shell.

2.2.7.2 Multiple sequence alignment of BamB homologs.

All 21 Uniprot protein sequences considered for the BamB Multiple Sequence alignment had been previously reviewed. Multiple sequence alignment was carried out using Clustal Omega online tool (http://www.ebi.ac.uk/Tools/msa/clustalo/). The graphic was generated using Jalview (Version: 2.10.1) (Noinaj et al., 2011). The conserved columns with the highest score were indicated by "*" (Score = 11). Columns with a score of 10 contain mutations (but all other properties were conserved) and were marked with a "+". The calculation were based on AMAS method of multiple sequence alignment analysis (Livingstone and Barton, 1993).

2.2.8 BamB *in situ* photocrosslinking.

Stationary phase culture of *E. coli* BW25113 Δ*bamB*::Kan harbouring pGEM-T-*bamBX-His6* and pSup-BpaRS-6TRN grown in LB containing 100 mg/ml ampicillin, 30 mg/ml kanamycin and 50 mg/ml chloramphenicol was sub-cultured into LB medium (100 mL) containing 100 mg/ml ampicillin, 30 mg/ml kanamycin, 50 mg/ml chloramphenicol and 1 mM BPA and grown for 6 h at 30°C with shaking (200 rpm). BPA was prepared as a 1 M stock solution in 1 M NaOH, before addition to the LB medium.

Half of the *E.coli* culture (50 mL) was transferred to a 90 mm sterile petri dish and was UV irradiated (365 nm) for 10 mins at a distance of 5 cm from the UV lamp (Type B-100AP UV lamp). The rest of the culture was transferred to a 50 mL Falcon tube covered with aluminium foil. Both UV (+) and UV (-) cultures were harvested by centrifugation (4000x g, 10 min, 4 °C). The *E. coli* cell pellets were then solubilized with 1% SDS buffer (50 mM Tris-HCl [pH8.0], 150 mM NaCl and 1% SDS) and diluted with 0.5% TritonX-100 buffer (50 mM Tris-HCl [pH8.0], 150 mM NaCl and 0.5% TritonX-100). Crosslinked products were then affinity purified with Ni-NTA agarose and eluted with Elution buffer (50 mM Tris-HCl [pH8.0], 150 mM NaCl, 0.5% TritonX-100 and 400 mM imidazole-HCl [pH8.0]). The elute fractions were subjected to TCA precipitation and then analysed by SDS-PAGE followed by immunoblotting.

2.2.9 BamB disulphide crosslinking.

The protocol described by Noinaj et al., (2014) was adapted to monitor disulphide crosslink formation in BamB mutants (Noinaj et al., 2014b). Cultures grown to stationary phase were harvested by centrifugation (4000x g, 10 min, 4 °C). The whole cell lysates of Cys incorporated BamB mutants were resolved using SDS-PAGE under non-reducing conditions (no DTT) followed by immunoblotting with anti-BamB antibody. To enhance disulphide crosslinking, cells were supplemented with 100 μM of Copper (II) sulfate and incubated at 37°C for 30 min with the reaction buffer (20 mM Tris-HCl, pH 7.5 and 100 mM NaCl). To disrupt the disulphide bonds in the samples, a resuspended cell pellet in PBS was supplemented with 50 mM DTT and incubated for 30 mins in RT. This suspension was then TCA precipitated and resuspended in DTT free loading buffer (2x) and resolved using SDS-PAGE.

Table 2.1 Primary and secondary antibodies.

Antibody	Type	Epitope source and specificity	Host	Source
Anti-BamA	Polyclonal	Raised against BamA POTRA domain regions in *Escherichia coli*	Mouse	Gifted from S. Buchanan Laboratory at NIH
Anti-BamA	Polyclonal	Raised against full length of BamA in *Escherichia coli*	Rabbit	Laboratory stock
Anti-BamB	Polyclonal	Raised against full length of BamB in *Escherichia coli*	Rabbit	Laboratory stock
Anti-BamC	Polyclonal	Raised against full length of BamC in *Escherichia coli*	Mouse	Gifted from S. Buchanan Laboratory at NIH
Anti-BamC	Polyclonal	Raised against full length of BamC in *Escherichia coli*	Rabbit	Laboratory stock
Anti-BamD	Polyclonal	Raised against full length of BamD in *Escherichia coli*	Rabbit	Laboratory stock
Anti-BamE	Polyclonal	Raised against full length of BamE in *Escherichia coli*	Rabbit	Laboratory stock
Anti-Ag43(α)	Polyclonal	Raised against Ag43α domain in *Escherichia coli*	Rabbit	Gifted from M. Schembri Laboratory at University of Queensland
Anti-LPS	Monoclonal	Raised against whole *E. coli* J5 cells	Mouse	Abcam® ab35654
Anti-SurA	Polyclonal	Raised against SurA *Escherichia coli*	Rabbit	Gifted from K. Tokatlidis
Anti-MalE	Polyclonal	Raised against Maltose binding protein in *Escherichia coli*	Rabbit	Laboratory stock
Anti-F1-β	Polyclonal	Raised against F1-ATPase β subunit in *Saccharomyces cerevisiae*	Rabbit	Laboratory stock
Goat anti-Rabbit IgG (H+L) Alexa Fluor® 647 conjugate.	Polyclonal	Rabbit IgG	Goat	ThermoFisher® A-21245
Goat anti-Mouse IgG (H+L) Alexa Fluor® 647 conjugate.	Polyclonal	Mouse IgG	Goat	ThermoFisher® A-21235

Table 2.2 Plasmids

Plasmid name	Expressed Protein	Promoter	Vector backbone	Primers used	Cloning site/ method	Template DNA source/ Reference
pGEM-T-*bamB-His₆*	BamB-Cterm-His₆	Native	pGEM®-T Easy	SDG-BamB-Fw SDG-BamB-Rv	A-tailing	*E. coli*-K12 BW25113 genomic DNA
pGEM-T-*bamB(K90X)-His₆*	BamB(K90X)-Cterm-His₆	Native	pGEM®-T Easy	SDG-BamB-(K90X)-Fw SDG-BamB-(K90X)-Rv	Quick change mutagenesis	pGEM-T-*bamB-His₆*
pGEM-T-*bamB(D138X)-His₆*	BamB(D138X)-Cterm-His₆	Native	pGEM®-T Easy	SDG-BamB-(D138X)-Fw SDG-BamB-(D138X)-Rv	Quick change mutagenesis	pGEM-T-*bamB-His₆*
pGEM-T-*bamB(S193X)-His₆*	BamB(S193X)-Cterm-His₆	Native	pGEM®-T Easy	SDG-BamB-(S193X)-Fw SDG-BamB-(S193X)-Rv	Quick change mutagenesis	pGEM-T-*bamB-His₆*
pGEM-T-*bamB(L244X)-His₆*	BamB(L244X)-Cterm-His₆	Native	pGEM®-T Easy	SDG-BamB-(L244X)-Fw SDG-BamB-(L244X)-Rv	Quick change mutagenesis	pGEM-T-*bamB-His₆*
pGEM-T-*bamB(K90A)-His₆*	BamB(K90A)-Cterm-His₆	Native	pGEM®-T Easy	SDG-BamB(K90A)-Fw SDG-BamB(K90A)-Rv	Quick change mutagenesis	pGEM-T-*bamB-His₆*
pGEM-T-*bamB(K90S)-His₆*	BamB(K90S)-Cterm-His₆	Native	pGEM®-T Easy	SDG-BamB-(K90S)-Fw SDG-BamB-(K90S)-Rv	Quick change mutagenesis	pGEM-T-*bamB-His₆*
pGEM-T-*bamB(D138A)-His₆*	BamB(D138A)-Cterm-His₆	Native	pGEM®-T Easy	SDG-BamB-(D138A)-Fw SDG-BamB-(D138A)-Rv	Quick change mutagenesis	pGEM-T-*bamB-His₆*
pGEM-T-*bamB(D138S)-His₆*	BamB(D138S)-Cterm-His₆	Native	pGEM®-T Easy	SDG-BamB-(D138S)-Fw SDG-BamB-(D138S)-Rv	Quick change mutagenesis	pGEM-T-*bamB-His₆*
pGEM-T-*bamB(K90C)-His₆*	BamB(K90C)-Cterm-His₆	Native	pGEM®-T Easy	SDG-BamB-(K90C)-Fw SDG-BamB-(K90C)-Rv	Quick change mutagenesis	pGEM-T-*bamB-His₆*
pGEM-T-*bamB(D138C)-His₆*	BamB(D138C)-Cterm-His₆	Native	pGEM®-T Easy	SDG-BamB-(D138C)-Fw SDG-BamB-(D138C)-Rv	Quick change mutagenesis	pGEM-T-*bamB-His₆*
pGEM-T-*bamB(L192S,L194S,R195A)-His₆*	BamB(L192S,L194S,R195A)-Cterm-His₆	Native	pGEM®-T Easy	SDG-BamB-(triple mutant)-Fw SDG-BamB-(triple mutant)-Rv	Quick change mutagenesis	pGEM-T-*bamB-His₆*
pSup-BpaRS-6TRN	BpaRs and	N/A	N/A	N/A	N/A	Ryu and Schultz, 2006

	amber suppressor tRNA					
pCO2	Ag43	*ara* promoter	pBAD	N/A	N/A	Klemm et al., 2004

Table 2.3 Primers for plasmid constructs

Primer name	Sequence 5'->3'
SDG-BamB-Fw	CCATCAGGTTGATTCTGCACG
SDG-BamB-Rv	TTAGTGGTGATGGTGATGATGACGTGTAATAGAGTACACGGTTCC
SDG-BamB(K90A)-Fw	GCGGATGATGGCGCGGAAATCTGGTCT
SDG-BamB(K90A)-Rv	AGACCAGATTTCCGCGCCATCATCCGC
SDG-BamB-(K90S)-Fw	GCGGATGATGGCAGCGAAATCTGGTCT
SDG-BamB-(K90S)-Rv	AGACCAGATTTCGCTGCCATCATCCGC
SDG-BamB-(D138A)-Fw	CTGAATACCAGCGCGGGTACTGTGGCA
SDG-BamB-(D138A)-Rv	TGCCACAGTACCCGCGCTGGTATTCAG
SDG-BamB-(D138S)-Fw	CTGAATACCAGCAGCGGTACTGTGGCA
SDG-BamB-(D138S)-Rv	TGCCACAGTACCGCTGCTGGTATTCAG
SDG-BamB-(K90C)-Fw	GCGGATGATGGCTGCGAAATCTGGTCT
SDG-BamB-(K90C)-Rv	AGACCAGATTTCGCAGCCATCATCCGC
SDG-BamB-(D138C)-Fw	CTGAATACCAGCTGCGGTACTGTGGCATGG
SDG-BamB-(D138C)-Rv	CCATGCCACAGTACCGCAGCTGGTATTCAG
SDG-BamB-(triple mutant)-Fw	CCTTCGAGCTCTAGCGCGGGCGAGTCTGCGCCGACA
SDG-BamB-(triple mutant)-Rv	CGGCGCAGACTCGCCCGCGCTAGAGCTCGAAGGCATATC

Table 2.4 Primers for BPA introduction into BamB

Primer Name	Amber codon position (X)	BamBX-Forward Primer (5'->3')	BamBX-Reverse Primer (5'->3')
SDG-BamB-(F42X)-Fw & Rv	42	GTTGAAAACCAGTAGACGCCGACCACG	CGTGGTCGGCGTCTACTGGTTTTCAAC
SDG-BamB-(S51X)-Fw & Rv	51	GCGTGGAGCACTTAGGTTGGTAGCGGC	GCCGCTACCAACCTAAGTGCTCCACGC
SDG-BamB-(S54X)-Fw & Rv	54	ACTTCCGTTGGTTAGGGCATTGGCAAC	GTTGCCAATGCCCTAACCAACGGAAGT
SDG-BamB-(D69X)-Fw & Rv	69	CCGGCACTGGCGTAGAACGTTGTCTAT	ATAGACAACGTTCTACGCCAGTGCCGG
SDG-BamB-(N70X)-Fw & Rv	70	CCGGCACTGGCGGACTAGGTTGTCTATGCCAGCG	CGCTGCATAGACAACCTAGTCCGCCAGTGCCGG
SDG-BamB-(A86X)-Fw & Rv	86	GGTTTAGTAAAAGCGCTGAATTAGGATGATGGCAAAGAAATCTGG	CCAGATTTCTTTGCCATCATCCTAATTCAGCGCTTTTACTAAACC
SDG-BamB-(D87X)-Fw & Rv	87	TTAGTAAAAGCGCTGAATGCGTAGGATGGCAAAGAAATCTGGTCT	AGACCAGATTTCTTTGCCATCCTACGCATTCAGCGCTTTTACTAA
SDG-BamB-(D88X)-Fw & Rv	88	GTAAAAGCGCTGAATGCGGATTAGGGCAAAGAAATCTGGTCTGTC	GACAGACCAGATTTCTTTGCCCTAATCCGCATTCAGCGCTTTTAC
SDG-BamB-(G89X)-Fw & Rv	89	AAAGCGCTGAATGCGGATGATTAGAAAGAAATCTGGTCTGTCAGC	GCTGACAGACCAGATTTCTTTCTAATCATCCGCATTCAGCGCTTT

SDG-BamB-(K90X)-Fw & Rv	90	GCGGATGATGGCTAGGAAATCTGGTCT	AGACCAGATTTCCTAGCCATCATCCGC
SDG-BamB-(S94X)-Fw & Rv	94	GGCAAAGAAATCTGGTAGGTCAGCCTGGCCGAG	CTCGGCCAGGCTGACCTACCAGATTTCTTTGCC
SDG-BamB-(E99X)-Fw & Rv	99	GTCAGCCTGGCCTAGAAAGATGGCTGG	CCAGCCATCTTTCTAGGCCAGGCTGAC
SDG-BamB-(W103X)-Fw & Rv	103	GAGAAAGATGGCTAGTTCTCTAAAGAG	CTCTTTAGAGAACTAGCCATCTTTCTC
SDG-BamB-(G119X)-Fw & Rv	119	TCTGGCGGTGTGACCGTGTCTTAG GGGCATGTCTACATTGGCAGC	GCTGCCAATGTAGACATGCCCCTAAGACAC GGTCACACCGCCAGA
SDG-BamB-(S137X)-Fw & Rv	137	CAGGTTTACGCGCTGAATACCTAG GATGGTACTGTGGCATGGCAA	TTGCCATGCCACAGTACCATCCTAGGTATTC AGCGCGTAAACCTG
SDG-BamB-(D138X)-Fw & Rv	138	CTGAATACCAGCTAGGGTACTGTGGCA	TGCCACAGTACCCTAGCTGGTATTCAG
SDG-BamB-(G139X)-Fw & Rv	139	TACGCGCTGAATACCAGCGATTAG ACTGTGGCATGGCAAACTAAA	TTTAGTTTGCCATGCCACAGTCTAATCGCTG GTATTCAGCGCGTA
SDG-BamB-(T140X)-Fw & Rv	140	GCGCTGAATACCAGCGATGGTTAG GTGGCATGGCAAACTAAAGTC	GACTTTAGTTTGCCATGCCACCTAACCATCG CTGGTATTCAGCGC
SDG-BamB-(A142X)-Fw & Rv	142	AATACCAGCGATGGTACTGTGTAG TGGCAAACTAAAGTCGCGGGT	ACCCGCGACTTTAGTTTGCCACTACACAGTA CCATCGCTGGTATT
SDG-BamB-(D159X)-Fw & Rv	159	CCGGTGGTCAGCTAGGGTCTGGTGTTA	TAACACCAGACCCTAGCTGACCACCGG

SDG-BamB-(D178X)-Fw & Rv	178	CTGAACGAAGCTTAGGGCGCTGTCAAA	TTTGACAGCGCCCTAAGCTTCGTTCAG
SDG-BamB-(S193X)-Fw & Rv	193	ATGCCTTCGCTCTAGTTGCGTGGCGAG	CTCGCCACGCAACTAGAGCGAAGGCAT
SDG-BamB-(G196X)-Fw & Rv	196	CTCTCTTTGCGTTAGGAGTCTGCGCCG	CGGCGCAGACTCCTAACGCAAAGAGAG
SDG-BamB-(F204X)-Fw & Rv	204	CCGACAACGGCTTAGGGTGCGGCCGTC	GACGGCCGCACCCTAAGCCGTTGTCGG
SDG-BamB-(E222X)-Fw & Rv	222	GCAGTGCTGATGTAGCAGGGCCAGATG	CATCTGGCCCTGCTACATCAGCACTGC
SDG-BamB-(D242X)-Fw & Rv	242	TCTACCGAAATTTAGCGTCTGAGCGAT	ATCGCTCAGACGCTAAATTTCGGTAGA
SDG-BamB-(L244X)-Fw & Rv	244	GAAATTGACCGTTAGAGCGATGTTGAC	GTCAACATCGCTCTAACGGTCAATTTC
SDG-BamB-(N255X)-Fw & Rv	255	CCCGTCGTTGTTTAGGGCGTTGTTTTC	GAAAACAACGCCCTAAACAACGACGGG
SDG-BamB-(R273X)-Fw & Rv	273	GCGCTTGATCTGTAGAGTGGTCAGATT	AATCTGACCACTCTACAGATCAAGCGC
SDG-BamB-(G293X)-Fw & Rv	293	TTCATCGTCGACTAGAATCGCATCTAT	ATAGATGCGATTCTAGTCGACGATGAA
SDG-BamB-(R295X)-Fw & Rv	295	GTCGACGGCAATTAGATCTATCTGGTC	GACCAGATAGATCTAATTGCCGTCGAC

SDG-BamB-(D321X)-Fw & Rv	321	TGGACACAAAGCTAGCTGCTGCATCGC	GCGATGCAGCAGCTAGCTTTGTGTCCA
SDG-BamB-(H324X)-Fw & Rv	324	AGCGATCTGCTGTAGCGCCTGCTGACT	AGTCAGCAGGCGCTACAGCAGATCGCT
SDG-BamB-(N334X)-Fw & Rv	334	CCGGTGCTGTATTAGGGCAACCTGGTG	CACCAGGTTGCCCTAATACAGCACCGG
SDG-BamB-(E352X)-Fw & Rv	352	TGGATTAACGTCTAGGATGGTCGTTTC	GAAACGACCATCCTAGACGTTAATCCA
SDG-BamB-(S364X)-Fw & Rv	364	CAAAAAGTTGATTAGTCCGGTTTCCAG	CTGGAAACCGGACTAATCAACTTTTTG
SDG-BamB-(D375X)-Fw & Rv	375	CCGGTTGCCGCTTAGGGCAAACTGCTG	CAGCAGTTTGCCCTAAGCGGCAACCGG
SDG-BamB-(K377X)-Fw & Rv	377	GCCGCTGACGGCTAGCTGCTGATCCAG	CTGGATCAGCAGCTAGCCGTCAGCGGC

Table 2.5 Buffers and solutions

Name	Components
BN-PAGE gel buffer (3x)	75 mM Bis-Tris, pH 7.0, 600 mM ε-amino n-caproic acid
BN-PAGE marker	0.6 mg ml^{-1} ferritin, 0.6 mg ml^{-1} catalase, 0.5 mg ml^{-1} BSA in BN-PAGE loading dye
BN-PAGE anode buffer (10x)	500 mM Bis-Tris/HCl pH 7.0
BN-PAGE cathode buffer (10x)	500 mM Tricine pH 7.0, 150 mM Bis-Tris, For a 1x working solution; 100 mL of 10x BN-PAGE cathode buffer, 0.02% Coomassie brilliant blue G-250, 0.05% DDM
BN-PAGE loading dye	5% Coomassie brilliant blue G-250, 500 mM ε-amino n-caproic acid, 100 mM Bis-Tris pH 7.0
BN-PAGE DDM buffer	1% DDM, 20 mM Tris-Cl pH 7.4, 0.1 mM EDTA, 50 mM NaCl, 10% glycerol (v/v)
Coomassie Blue Stain	0.1% Coomassie blue, 20% ethanol, 7.5% acetic acid
Destain	40% ethanol, 7.5% acetic acid
DNA loading dye (6x)	0.25% (w/v) bromophenol blue, 40% sucrose
ECL solution 1	First dissolve 200 mg luminal in 4.5 ml DMSO (solution A) then in a separate tube dissolve 35 mg pCoumaric acid in 2.5 ml DMSO (solution B). Then add both solutions A and B to 250 ml of 100 mM Tris pH 9.35
ECL solution 2	Add 30 µl of 30% H_2O_2 to 250 ml of 100 mM Tris pH 9.35
Luria Broth (LB) (1L)	10 g tryptone, 5 g yeast extract, 5 g NaCl, pH 7.0
Lysis buffer	1.5 mM EDTA, pH 7.5
Phosphate Buffered Saline (PBS) (1L of 10x)	80 g NaCl, 2 g KCl, 14.4 g Na_2HPO_4, 7 g KH_2PO_4, pH to 7.4 then autoclave. (1x = 137 mM NaCl, 2.7 mM KCl, 100 mM Na_2HPO_4, 2 mM KH_2PO_4)
Ponceau stain	10% acetic acid, 5% ponceau stain
SDS-PAGE Tris-glycine running buffer (10 x)	30.3 g Tris, 71.3 g Glycine, 5 g SDS make up to 1L
SDS-PAGE Tris-glycine stacking buffer (8 x)	1 M Tris pH 6.8, 0.08% SDS, 2 mM EDTA
SDS-PAGE Tris-glycine separating buffer (4 x)	1.5 M Tris pH 8.8, 0.4% SDS, 2 mM EDTA
SDS-PAGE sample buffer (Laemmli buffer)	50 mM Tris-Cl pH 6.8, 1% SDS, 10% glycerol, 100 mM DTT, 0.005% bromophenol blue
TAE (1L of 50x)	242 g Tris base, 57.1 glacial acetic acid, 100 ml 0.5 M EDTA, filter solution

Tris-buffered saline (TBS) (10 x)	200 mM Tris-HCl pH 7.5, 1.25 M NaCl
Tris-buffered saline – Tween (TBS-T)	1 x TBS, 0.2% Tween
Western transfer buffer (4 L of 10x)	570 g glycine, 120 g Tris.
Western transfer buffer (10% methanol) (4 L of 1x)	400 mL of 10 x Western transfer buffer, 400 ml of methanol, dH $_2$ O to 4 L. (for BN-PAGE transfer)
Western transfer buffer (10% methanol) (4 L of 0.5x)	200 mL of 10 x Western transfer buffer, 400 ml of methanol, dH $_2$ O to 4 L. (for SDS-PAGE transfer)

Chapter 3: Super-resolution imaging of protein assembly precincts on bacterial cell surfaces.

3.1 Introduction

In gram-negative bacteria, the outer membrane is the external surface of the cell. Abundant proteins in the bacterial outer membrane are β-barrels that can form pores for small molecule exchange (such as OmpF, OmpC, LamB etc) and facilitated diffusion channels (such as the TonB-dependent receptors BtuB, CirA, FhuA, etc) . Many of these proteins are oligomeric and their assembly depends on the BAM complex. The architecture of the BAM complex is understood from crystal structures of the individual components BamA (Noinaj et al., 2013), BamB (Heuck et al., 2011; Kim and Paetzel, 2011; Noinaj et al., 2011), BamC (Kim et al., 2011), BamD (Kim et al., 2011; Sandoval et al., 2011) and BamE (Knowles et al., 2011), along with crystal structures of the BAM complex and from interactive surfaces mapped through genetics and fusion protein approaches (Malinverni et al., 2006; Vuong et al., 2008; Rigel et al., 2012; Bakelar et al., 2016; Bergal et al., 2016; Gu et al., 2016; Han et al., 2016). The current model for the quaternary structure of the BAM complex proposes that each BamA molecule binds one molecule of each of the other BAM subunits, with BamC exposed on the outer face of the outer membrane and BamB, BamD and BamE exposed in the periplasmic space between the outer and inner (cytoplasmic) membrane (Hagan et al., 2010b; O'Neil et al., 2015).

Two recent studies have used surface imaging of intact *Escherichia coli* to address the spatially-important aspects of outer membrane protein movements. Theriot and colleagues used *in situ* labelling of nascent LamB molecules to record the initial appearance of this β-barrel protein in the outer membrane (Ursell et al., 2012). Statistical analysis of the confocal imaging data suggested that the sites of insertion for LamB were randomly

distributed across the outer membrane of the *E. coli* cells. Further, the data showed that there was little if any movement of the assembled LamB β-barrels by lateral diffusion, but rather that assembled LamB was forced across the surface of *E. coli* by continuing insertion of new material into the outer membrane (Ursell et al., 2012). Conversely, in a study aimed at understanding the turn-over of β-barrel proteins, Rassam *et al.,* used total-internal reflection fluorescence microscopy (TIRFM) and molecular dynamics simulations on two abundant β-barrel proteins, BtuB and OmpF, to demonstrate protein-rich rafts formation due to promiscuous protein-protein interactions between these abundant proteins (Rassam et al., 2015). This study concluded that insertion of these proteins might occur in a spatially constrained zone at the midpoint of the cell. Given these differing conclusions on where and how β-barrel proteins are inserted into the outer membrane, I sought to directly assess the spatial distribution of the BAM complex in intact *E. coli* cells. For this I utilized new developments in super-resolution imaging technology to interrogate the bacterial cell biology at a nanoscale (Gahlmann and Moerner, 2014).

3.2 Results

3.2.1 Detection of BamC in *E. coli* cell surface.

The BAM complex is a nanomachine that spans the outer membrane with an ovoid shape of cross-sectional diameter ~8 nm to ~10 nm (O'Neil et al., 2015). The C-terminal helix grip domains of BamC are exposed on the bacterial cell surface (Figure 3.1) (Webb et al., 2012; O'Neil et al., 2015). From quantitative proteomic studies each of the subunits of the BAM complex are found in the outer membrane at similar abundance (~200-400 copies of each per cell) (Wisniewski and Rakus, 2014). BamC is expressed on the surface of all of the cells in a population of *E. coli*, as judged by immunofluorescence staining (Figure 3.2, upper panel). A strain of *E. coli* in which the *bamC* gene was deleted served as a negative control to validate the fluorescence signal specific to BamC (Figure 3.2, lower panel). Controls were also established to assess the fluorescence labelling specific to the surface exposed epitopes of BamC (Figure 3.3).
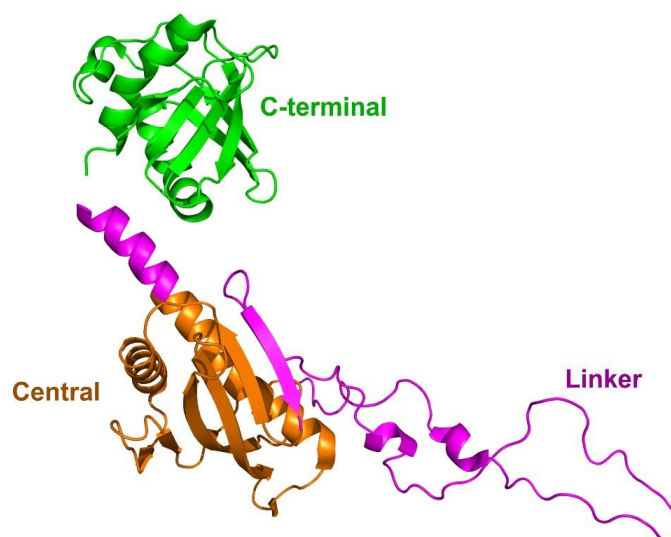
Figure 3.1 Crystal structure of BamC (PDB: 5d0q). The overall structure of BamC represents two helix grip domains with the central one connected to the C-terminal one by an α-helical linker. The C-terminal helix grip domain was shown to be exposed (partially or fully) on to the bacterial cell surface (Webb et al., 2012; O'Neil et al., 2015).
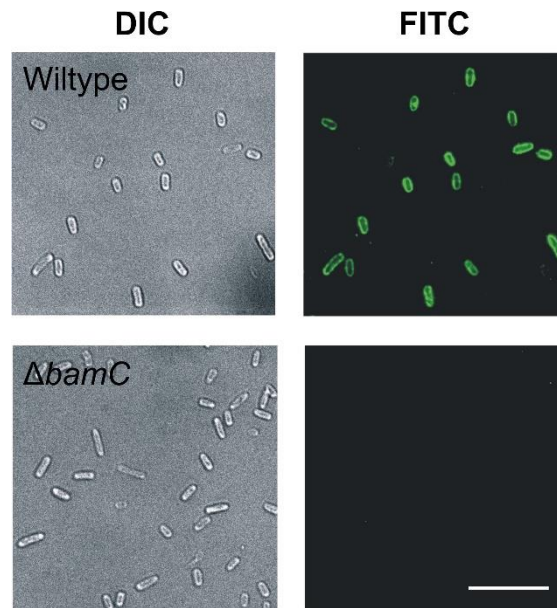
Figure 3.2 Immunofluorescence assessment of *E. coli* BW25113 using antibodies recognizing the C-terminal domain of BamC. At left, the Differential interference contrast (DIC) image for a representative field of cells and at the right is the fluorescence image (FITC) of antibody staining. Also shown is a control experiment from an isogenic Δ*bamC* mutant strain that lacks BamC. Scale bar 10 μm.
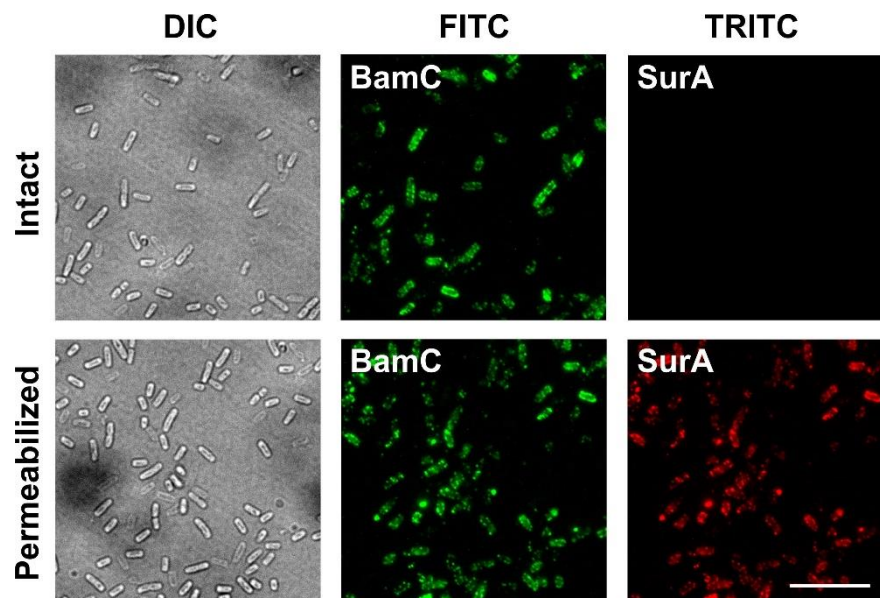
Figure 3.3 Immunofluorescence detection of BamC on the cell surface of *E. coli* BW25113. Upper panels represent intact bacterial cells and lower panel shows permeabilized cells. Both samples were stained with anti-BamC (secondary antibody Alexa fluor® 488) and anti-SurA (secondary antibody Alexa fluor® 594) antibody. SurA periplasmic protein was only detected in the TRITC panel of the permeabilized cell sample, confirming the BamC protein detection on the cell surface in the intact cells.

3.2.2 Super resolution imaging of BamC.

Conditions were established to use *d*STORM for super-resolution imaging of *E. coli* (see Chapter 2, section 2.1). The detection of outer membrane proteins in this system provides data on slices through an *E. coli* cell. Microscope was adjusted to image and capture the top most layer of bacterial cells (i.e. focal plane furthest away from the coverslip but within the specimen. More details in Chapter 2, section 2.1.11) to reduce background noise.
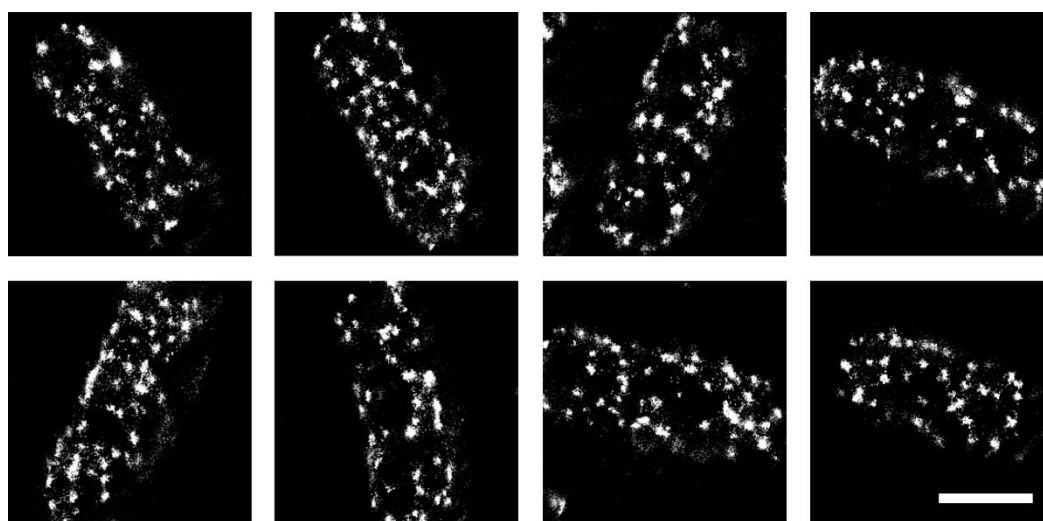
Figure 3.4 BamC of BAM complex exists as localised clusters at the outer membrane of *E. coli*. Single molecule localization imaging of BamC across the *E. coli* BW25113 cell surface. Scale bar 1 µm.

Across the bacterial cell surface, *d*STORM imaging of BamC showed a clustered distribution with no apparent concentration to the septum or polar regions (Figure 3.4). Cluster analysis algorithms were then used to quantify and analyse these signals (see Chapter 2, section 2.1.8). Plots of L(*r*)-*r* vs *r* showed the radius in which the highest degree of clustering ("peak cluster scale") can be observed for the spatial distribution. For BamC this was calculated to be ~ 50 nm (Figure 3.5-A). The cluster density figures showed 10.94 ± 0.4 clusters of BamC per square micrometre of cell surface (all calculated cluster measurements were summarised in Table 3.1).

A.

Region of interest (ROI) Heat-map Filtered mask
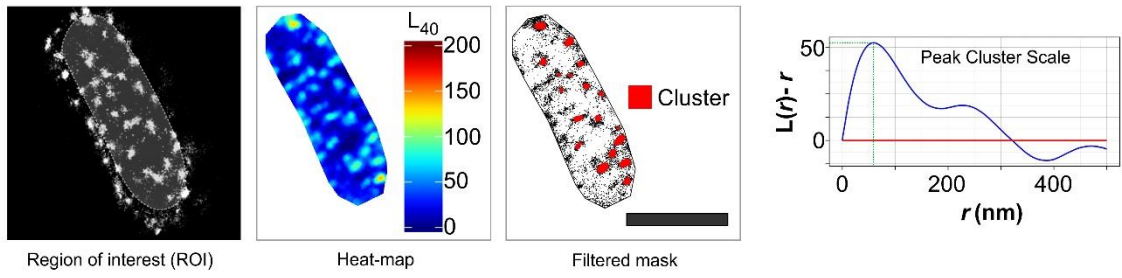
B.
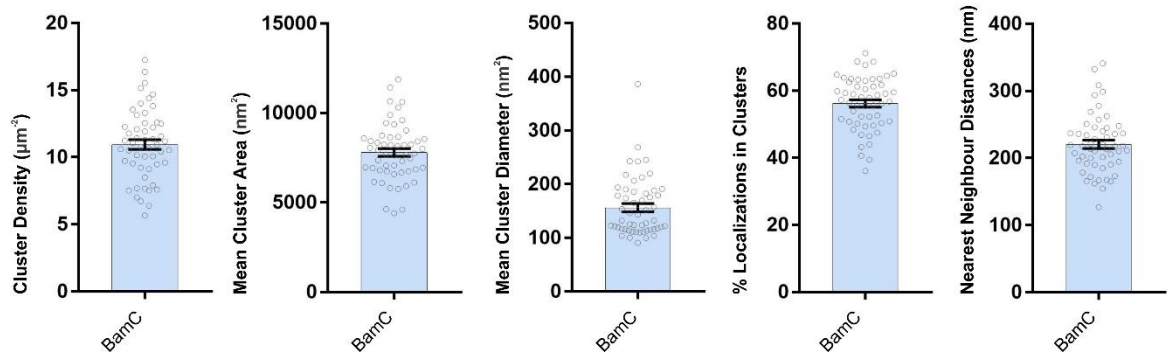
C.
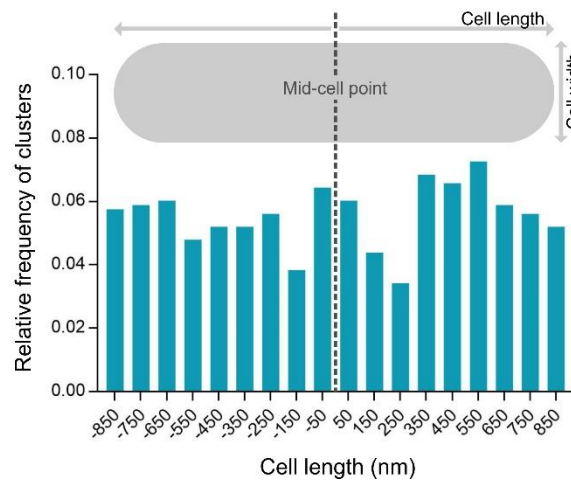
Figure 3.5 Cluster analysis of the BAM complex. (A) From left to right; selected area of rapi*d*STORM reconstructed super resolution image (ROI), Heat-map generated for the corresponding area (degree of clustering "L_{40}" increase from blue to red), edge effects filtered binary mask showing detected clusters within the threshold limits in red and plots of L(r)-r vs r showing the peak cluster scale of ~50 nm (random Poisson distribution in red and BamC distribution in blue). Scale bar 1 µm. **(B)** Cluster analysis data for BamC represented as combined bar graph and scatter plot; Cluster density, Mean Cluster area, Mean cluster diameter, Percentage of localizations captured within clusters and Nearest neighbour distances respectively. Error bars shown as mean ± SEM. **(C)** Histogram showing the relative frequency of BamC clusters against the cell length.

To generate a three dimensional view of the BamC distribution on the cell surface, a Vutara 350 imaging system was used for video-rate, single-molecule localization microscopy. These scans confirmed that BamC clusters are present across the surface of the *E. coli* cell (Juette et al., 2008; Mlodzianoski et al., 2009), with no concentration in mid-point or polar regions (Figure 3.6). Measurements based on the frequency of clusters along the length axis of an *E. coli* cell showed that BamC has a random spatial distribution across the cell surface (Figure 3.5-C).
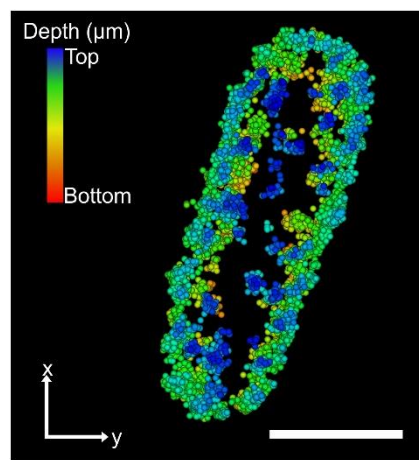
Figure 3.6 BamC surface distribution using 3D single molecule localization super resolution imaging (Vutara®). Anti-BamC single probe immunofluorescence is shown in the "x,y" dimension as a representation of the depth of signal through the z-dimension. Scale bar 1 μm.

3.2.3 Accessing periplasmic space for the spatial assessment of BamA subunit.

A majority of the molecular mass of the BAM complex is exposed to the periplasm. To validate that the distribution of BamC indeed represents the distribution of the BAM complex, I established conditions in which *d*STORM could be applied to interrogate the bacterial periplasmic space. BamA, the core component of the BAM complex is composed of five N-terminal polypeptide transport associated (POTRA) domains exposed to the periplasmic space and a C-terminal beta barrel domain embedded at the outer membrane. Fluorescent labelling of the POTRA domains and imaging through super resolution microscopy provides further information of the BAM complex distribution in this cellular compartment compared to the outer membrane.

Titration experiments using BamC spatial clusters as a standard were undertaken with detergents to provide limited permeabilization of the lipid phase of the outer membrane to allow access of the antibodies into the periplasm. With these titrations I was able to determine that the treatment with 0.001% digitonin or 0.001% TritonX-100 did not disturb BamC cluster parameters (cluster density, diameter or area) across the cell surface (Figure 3.7).
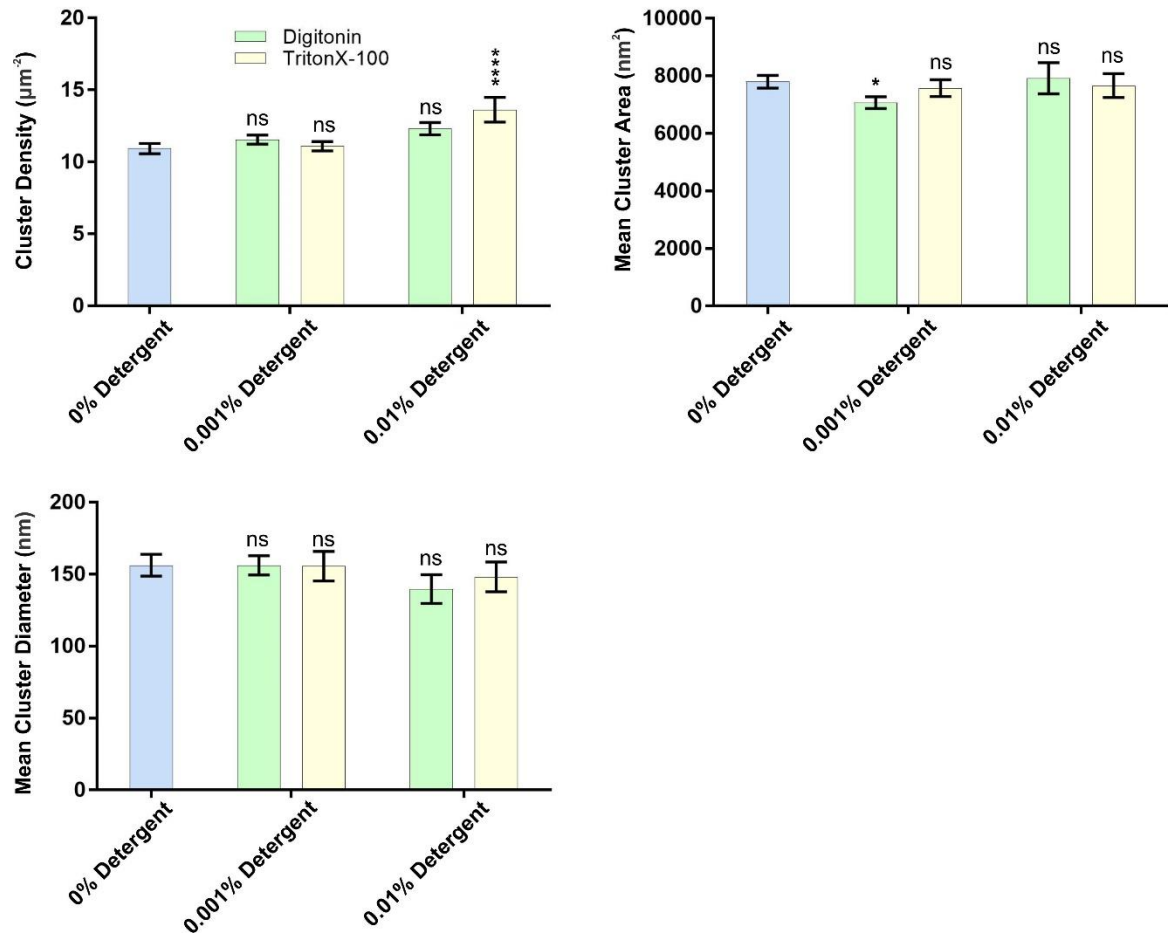
Figure 3.7 Detergent solubilisation effects on the spatial localisation of the BamC clusters. A sample of *E. coli* was treated with the indicated concentrations (w/v) of detergent (Digitonin or TrtitonX-100) and then analyzed by *d*STORM using antibodies recognizing BamC. Calculations were made for Cluster density, Cluster area, and Cluster diameter. By these parameters, either 0.001% Digitonin or 0.001% Triton X-100 was found to minimally perturb the distribution of BamC surface localization. These two detergent can have differential effects on membrane protein complexes (and both should be trialled in future studies on other membrane protein complexes). Statistical significance reported by P values (unpaired t-test) were calculated in comparison with the wildtype (detergent free) BamC: ns = P > 0.05, * = P ≤ 0.05, ** = P ≤ 0.01, *** = P ≤ 0.001, **** = P ≤ 0.0001.

3.2.4 Super resolution imaging of BamA-POTRA domains.

The detergent permeabilization protocol I developed provided means to detect the distribution of BamA by *d*STORM, using an antibody that recognizes the periplasmic (POTRA) domain of BamA (Figure 3.8). Super resolution imaging of BamA showed a similar clustered distribution to that of BamC. Spatial distribution analysis calculated these BamA clusters to have a mean diameter of 130.2 ± 9.1 nm (using 0.001% digitonin to permeabilize the outer membrane) (Figure 3.8).
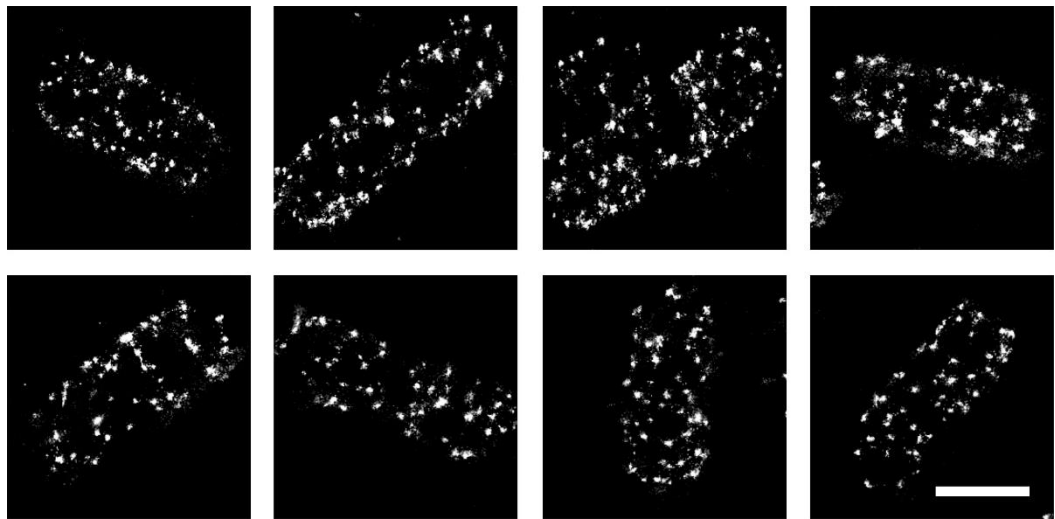
Figure 3.8 Single molecule localization imaging of BamA in the periplasmic space of *E. coli*. Similar to BamC, the BamA subunit of the BAM complex exists as localised clusters at the outer membrane of *E. coli*. Scale bar 1 μm.
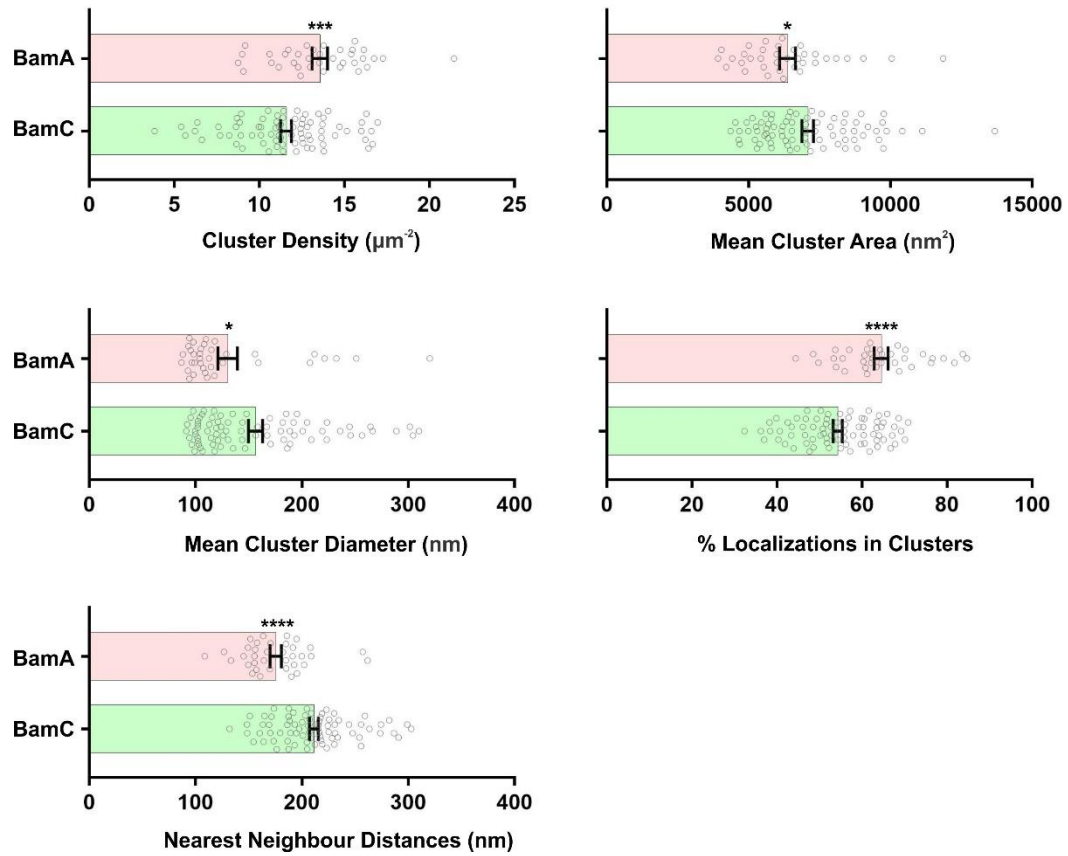
Figure 3.9 Cluster analysis of BamA and BamC in detergent solubilised *E. coli* cells. Samples of *E. coli* treated with 0.001% digitonin were immunostained with either anti-BamC, or with an antibody raised against the POTRA domain of BamA. Comparisons of cluster parameters were shown for BamC and BamA. Error bars shown as mean ± SEM. Statistical significance reported by P values (unpaired t-test) were calculated in comparison with the detergent solubilised BamC : ns = P > 0.05, * = P ≤ 0.05, ** = P ≤ 0.01, *** = P ≤ 0.001, **** = P ≤ 0.0001.

3.2.5 Investigating spatio-temporal characteristics of BAM clusters in the absence of endogenous protein synthesis.

In principle, the BAM complex clusters could be driven by the high rates of protein assembly that occur in log-phase of cell growth, where protein synthesis rates are maximal and the flux of nascent polypeptides destined for insertion into the outer membrane is therefore maximal. Alternatively, the clusters might represent an intrinsic property of how neighboring BAM complexes can sit together in the outer membrane. To investigate these scenarios, I analysed the effects of the antibiotic rifampicin. This antibiotic inhibits bacterial protein transcription, thereby blocking endogenous protein synthesis in *E. coli*. Hence, inhibiting membrane protein assembly (Stenberg et al., 2007; Stubenrauch et al., 2016).

E. coli BW25113 wild-type cells grown to mid-log phase in LB media were treated with the addition of rifampicin (200 µg/mL) for 1 h at 37°C with vigorous shaking (200 rpm). Live cell sample preparation was carried out using 8-well cover glass bottom chambers (Sarstedt®) as described above. Prior to cellular fixation, live-dead staining of *E.coli* cells was performed (LIVE/DEAD BacLight Bacterial Viability Kit, Molecular Probes™) (Figure 3.10). Dead cell controls were prepared using heat treatment (Oliver et al., 1990; Li et al., 2014). Olympus IX-81 inverted fluorescence microscope equipped with Olympus Cell^M software was used to visualize cell samples using the 100X objective with FITC and TRITC filters. The results showed even after 1 h of rifampicin treatment *E. coli* cells remained viable for further experiments.
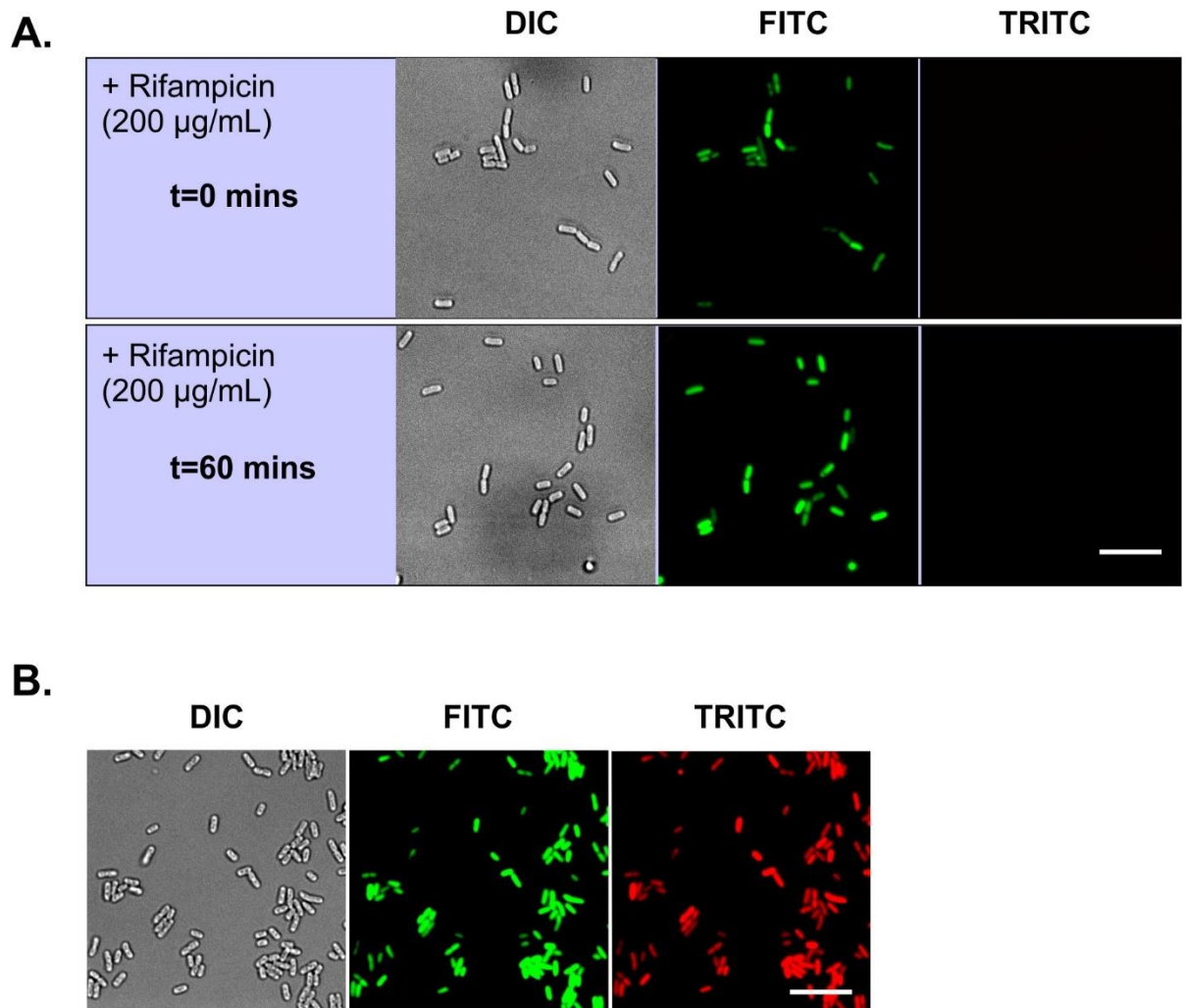
Figure 3.10 Viability assay performed on cells treated with protein transcriptional inhibitor Rifampicin. (**A**) Live-Dead[TM] staining of *E. coli* after rifampicin treatment for 0'- 60'. (**B**) Dead cell control was used in which the *E. coli* cells was incubated at 90°C. Green = live cells, Red = dead cells. Scale bar 10 µm.

Super resolution imaging of rifampicin treated cells (Figure 3.11) demonstrated a decrease in size of BAM complex clusters in the absence of ongoing protein synthesis. Cluster analysis showed the average diameter and area of BAM complex clusters was diminished by ~20% from its original wildtype level (Figure 3.12). Interestingly, the average cluster density was increased to 14.65 ± 0.4 μm^{-2} and the average nearest neighbour distances between clusters were decreased by ~20% (see Table 3.1 for complete list of statistical

figures). These observations could be explained by large BAM clusters dissociating to form smaller remnant clusters under rifampicin inhibited protein synthesis.
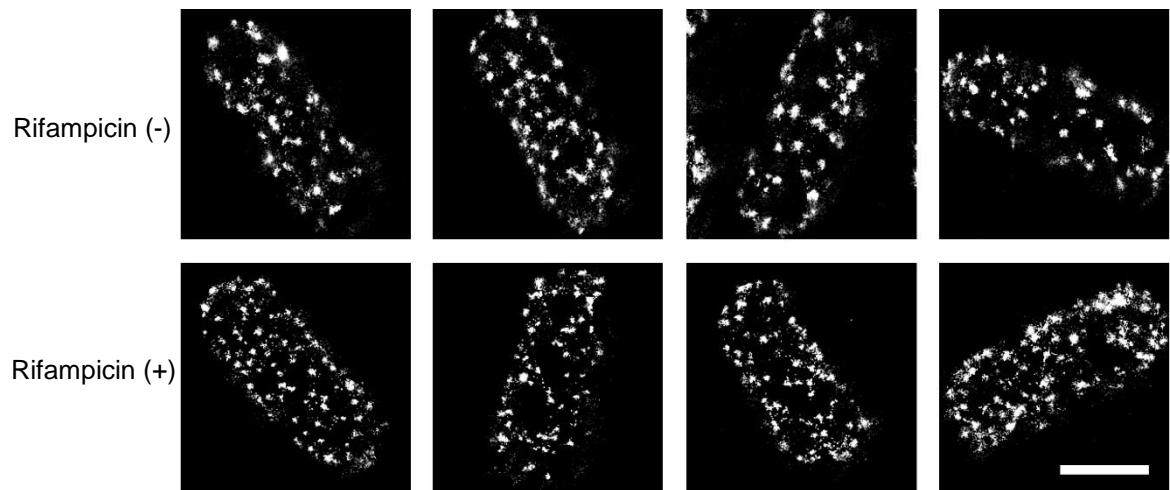
Figure 3.11 Single molecule localization imaging of BamC in *E. coli* treated with rifampicin. *E. coli* treated with or without rifampicin for 60 minutes. Scale bar 1 µm.
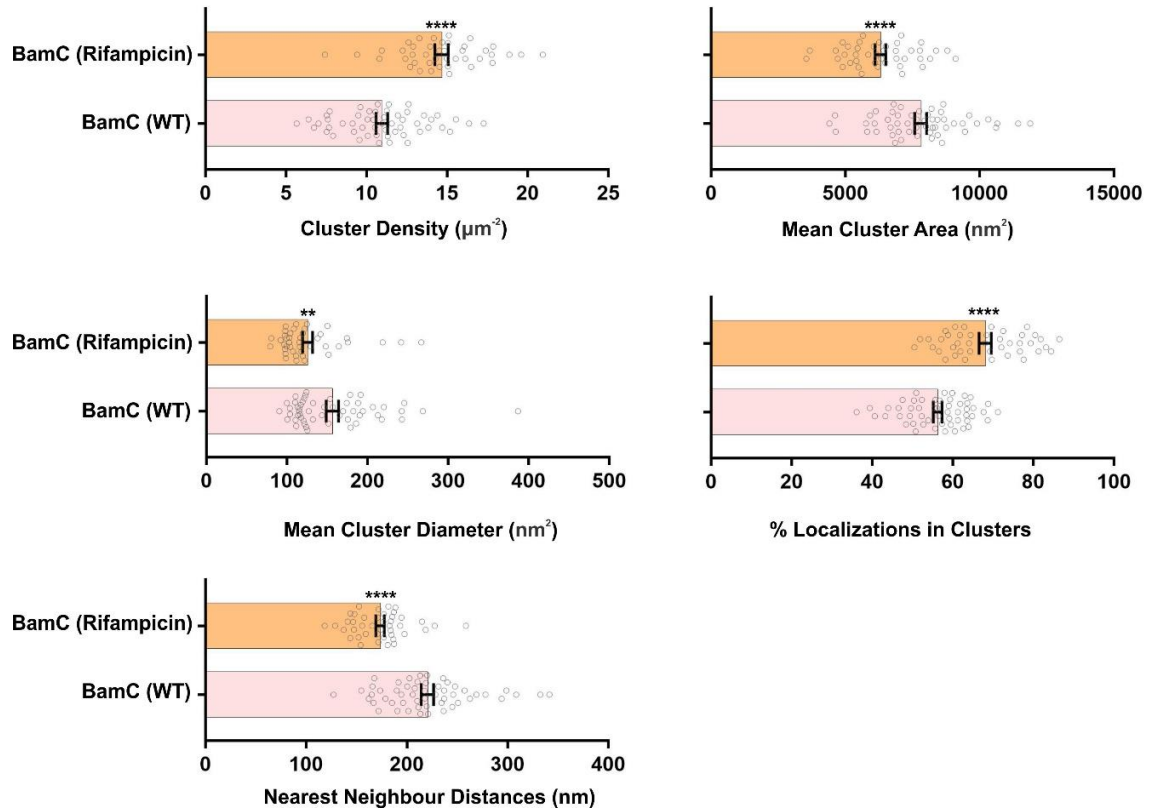
Figure 3.12 Cluster analysis of BamC in *E. coli* treated with rifampicin. Comparison of BamC cluster parameters where *E. coli* samples treated with or without Rifampicin for 60'. Error bars shown as mean ± SEM. Statistical significance reported by P values (unpaired t-test) were calculated in comparison with the Wildtype: ns = P > 0.05, * = P ≤ 0.05, ** = P ≤ 0.01, *** = P ≤ 0.001, **** = P ≤ 0.0001.

3.2.6 Mapping surface localization of a monomeric β-barrel protein (Antigen 43) using super resolution microscopy.

The BAM clusters I observed through *d*STORM are unlike the distribution of other outer membrane proteins visualized recently by TIRFM (Rassam et al., 2015). To map the surface distribution of a monomeric outer membrane protein by *d*STORM imaging the β-barrel protein Ag43 was visualised. Ag43 is a surface-exposed adhesin projecting up to 10 nm from the surface of *E. coli*, with a cross-sectional diameter of ~3.5 nm (Figure 3.13). Expression of Ag43 is phase-variable, meaning that in any given population of cells only a

proportion will be actively expressing Ag43 (Owen et al., 1996; van der Woude and Henderson, 2008).

To allow for the unpredictable outcome of phase variable expression, confocal microscopy experiments were conducted to monitor Ag43 expression within a given *E. coli* population. As judged by immunofluorescence staining of our lab stock of *E. coli* K-12 strains BW25113 and MG1655 showed 20% and 28% expression of Ag43 respectively (Figure 3.14). Using an isogenic strain of *E. coli* in which the *flu* gene encoding Ag43 was deleted, no Ag43 expression was detected, which validated the immunofluorescence signals as being specific to Ag43 (Figure 3.15).
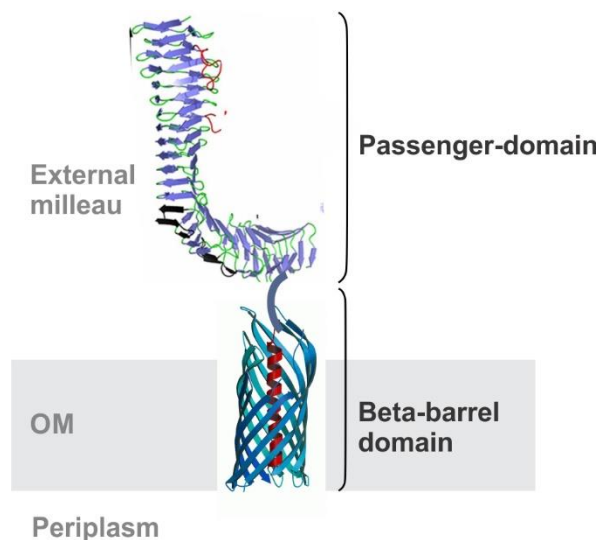
Figure 3.13 Topology of the autotransporter Antigen 43. The passenger domain extends up to 100 Å from the cell surface and mediates cellular auto-aggregation (Heras et al., 2014). The antibody used for the detection in the *d*STORM imaging were raised to the Ag43 passenger domain.
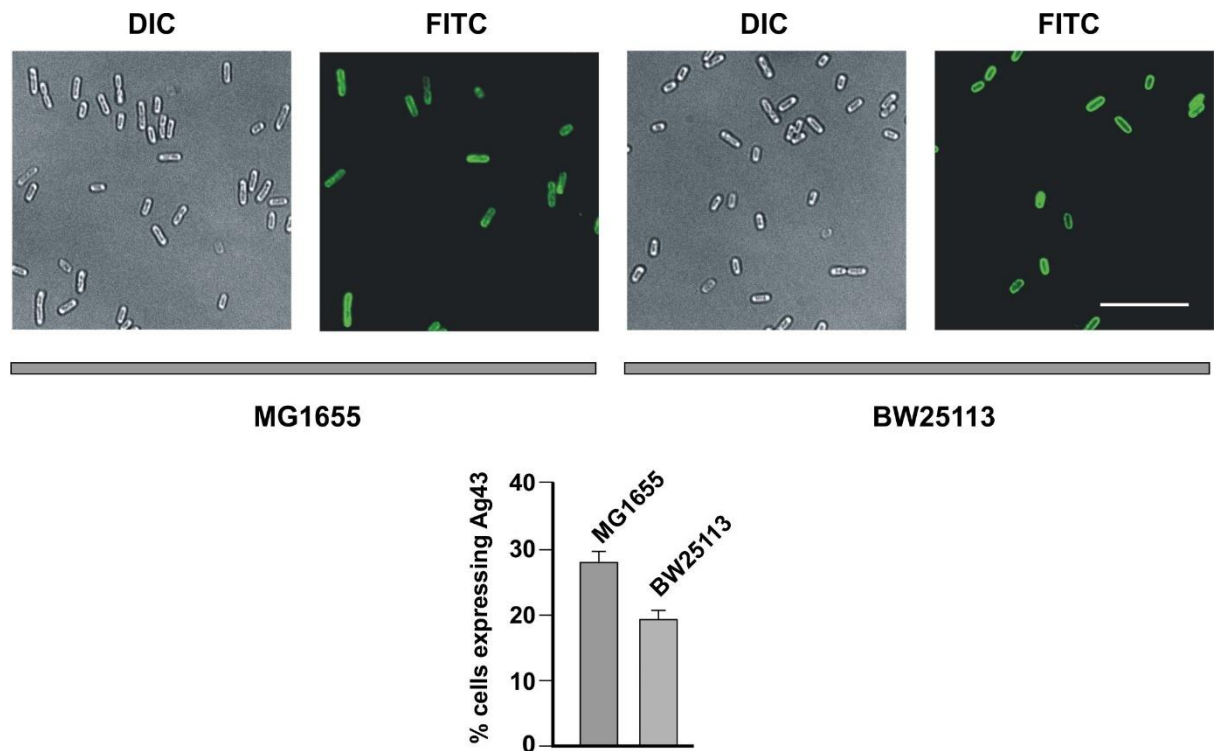
Figure 3.14 Expression and distribution of Ag43 on the cell surface of *E. coli*. Phase-variable expression of Ag43 was monitored by immunofluorescence and cell-counting. In 1000 cells of either MG1655 or BW25113, our lab stocks showed 18-28% of cells were positive for Ag43 staining.
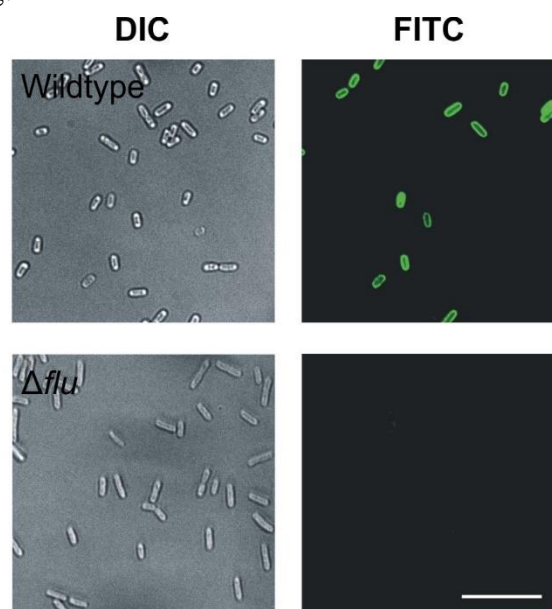
Figure 3.15 Immunofluorescence assessment of *E. coli* BW25113 using antibodies recognizing the α-domain of Ag43. Upper panel: at left is the DIC image for a representative field of cells, at right is the fluorescence image of antibody staining. Lower panel shown is a control experiment from an isogenic Δ*flu* mutant strain that lacks Ag43.

The *d*STORM data from immunostaining for Ag43 (Figure 3.16) and 3D reconstructed images generated using the Vutara 350 imaging system (Figure 3.17) revealed a uniform distribution of Ag43 on bacterial surface. Mapping the distribution of Ag43 also showed it to be comparable to the distribution of the lipopolysaccharide (LPS) matrix of the outer membrane (Figure 3.16), with both distributed similarly to the pattern described by Rassam *et al*., for OmpF and BtuB. This is in stark contrast to the tightly clustered localization of the BAM complex (Figure 3.18).
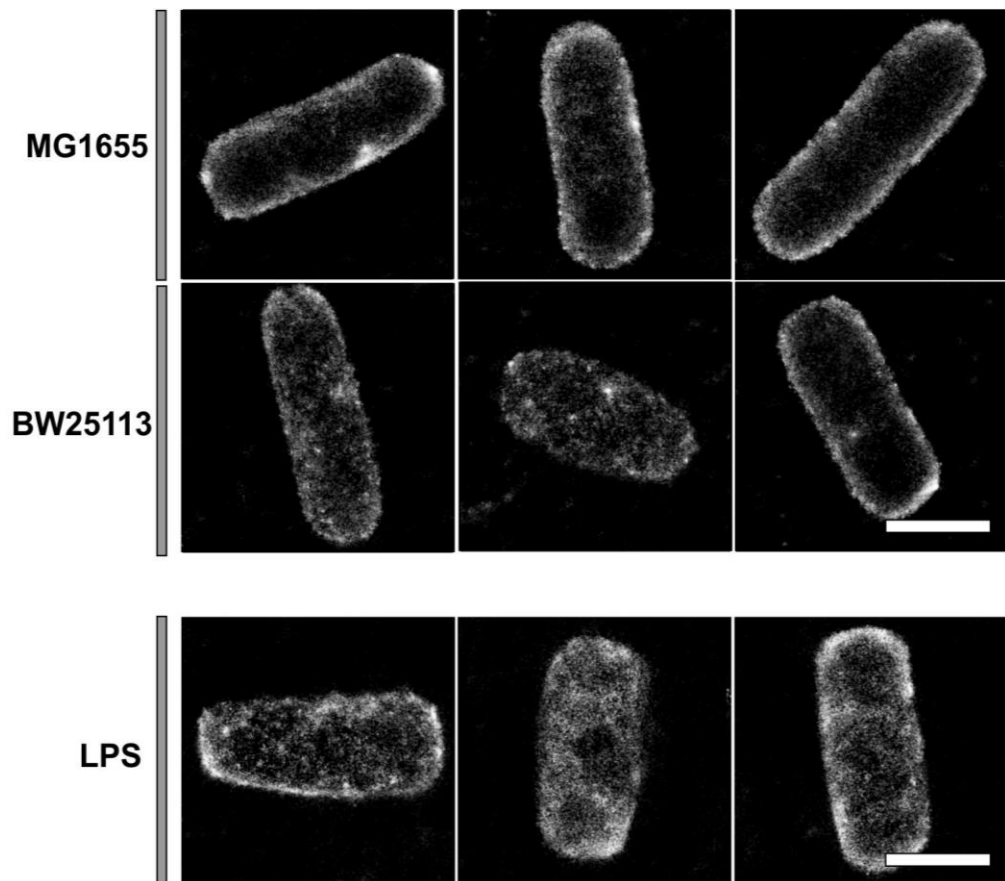
Figure 3.16 *d*STORM images of anti-Ag43 and anti-LPS labelled *E. coli* cells. Super resolution images for Ag43 and LPS distribution showed dense surface coverage lacking distinct structures in the cell surface.
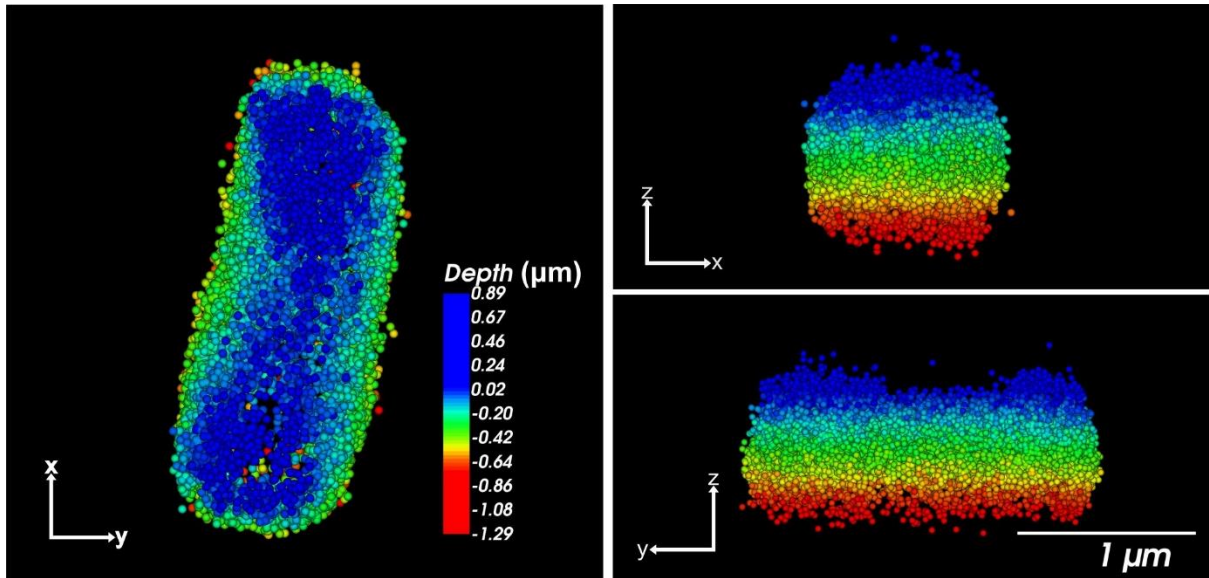
Figure 3.17 Antigen 43 surface distribution using 3D single molecule localization super resolution imaging (Vutara®). Anti-Ag43 single probe immunofluorescence shown in the "x,y" dimension coloured for the depth of signal through the z-dimension. Scale bar 1 μm.
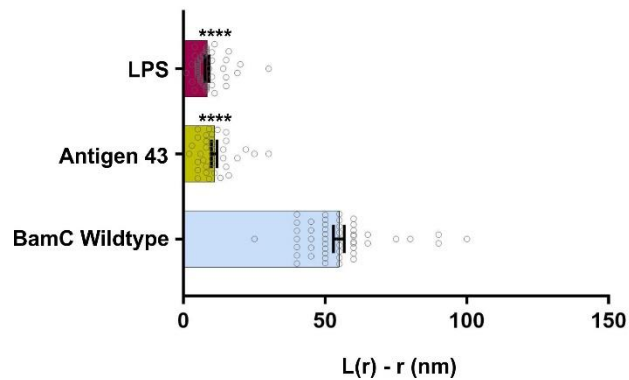
Figure 3.18 Peak cluster scale L(r)-r calculations for Ag43 and LPS, compared to those for BamC (Wildtype). Error bars shown as mean ± SEM. Statistical significance reported by P values were calculated in comparison with the BamC Wildtype: ns = P > 0.05, * = P ≤ 0.05, ** = P ≤ 0.01, *** = P ≤ 0.001, **** = P ≤ 0.0001.

3.2.7 The role played by lipoprotein subunits of BAM complex in maintaining BAM clusters on the surface of *E. coli*.

In bacteria such as *E. coli,* the BAM complex is a nanomachine formed from the integral protein BamA and four peripheral lipoproteins: BamB, BamC, BamD and BamE. BamA is itself a β-barrel, and the reversible pairing of β-strands 1 and 16 in BamA was proposed to serve as the catalytic site for the insertion of substrate OMPs into the outer membrane (Noinaj et al., 2013; Noinaj et al., 2014a), and yet this region of BamA does not sit stably in the lipid-phase of the outer membrane (Noinaj et al., 2013). I speculate that a cluster of BamA molecules could be structurally relevant, as it would provide a proteinaceous environment to help stabilise this bilayer-disrupting region of BamA. For some bacterial oligomeric surface proteins, more than one BAM complex would be required to assemble their final structure, thus interactions that would stabilise BAM complex protomers into higher-order clusters would be functionally relevant as well. However, the canonical structure of the BAM complex precludes these generalised promiscuous β-barrel interactions that have been measured for other β-barrels (Rassam et al., 2015), with any BAM:BAM interactions needing to be mediated at least in part through the periplasmic domains, the most expansive part of the BAM complex (O'Neil et al., 2015).

3.2.7.1 BamB subunit is essential to maintain BAM complex clusters.

The BamB subunit is a β-propeller that is a plausible candidate to mediate BAM:BAM interactions (Figure 3.1). β-propeller structures have been previously shown to serve as molecular Velcro to hold together unit complexes into super-complexes, such as is seen in the coatamer coat around secretory vesicles (Miller, 2013) and the membrane-attached lattice of the nuclear pore complex (Leksa and Schwartz, 2010). Structurally, each of the eight blades in the BamB propeller has four antiparallel β-strands, with the outermost β-

strand in each blade possibly serving as a binding surface to interact with a β-strand in a partner protein. Depending on the angular disposition of the POTRA domains of BamA, this bottom face of BamB would be exposed radially in a way that might enable BAM:BAM contacts between neighbours.

Deletion of BamB has no effect on the levels of the other components of the BAM complex (Palomino et al., 2011) (Figure 3.19), and yet *d*STORM analysis of these Δ*bamB* mutants showed less clustering of the BAM complex in the absence of BamB (Figure 3.20). There is a significant difference in the cluster density and in the proportion of BAM complexes found within clusters in these Δ*bamB* mutants (Figure 3.21). The mean cluster density for the BAM complex is diminished from 9.60±0.3 per μm-2 (wild-type) to 6.00±0.5 per μm-2 (Δ*bamB*) and, strikingly, only 19.07±2% of BAM complexes are found in clusters in the absence of BamB.
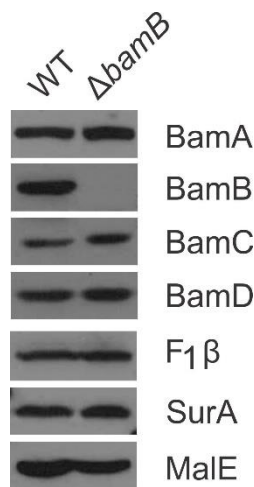
Figure 3.19 Δ*bamB* outer membrane proteome. Total cell extracts from wild-type *E. coli* and Δ*bamB* mutants were subject to SDS-PAGE and immunoblotting with the indicated antisera (Outer membrane BamABCD, periplasmic SurA and MalE, and inner membrane protein F1-β).

ΔbamB
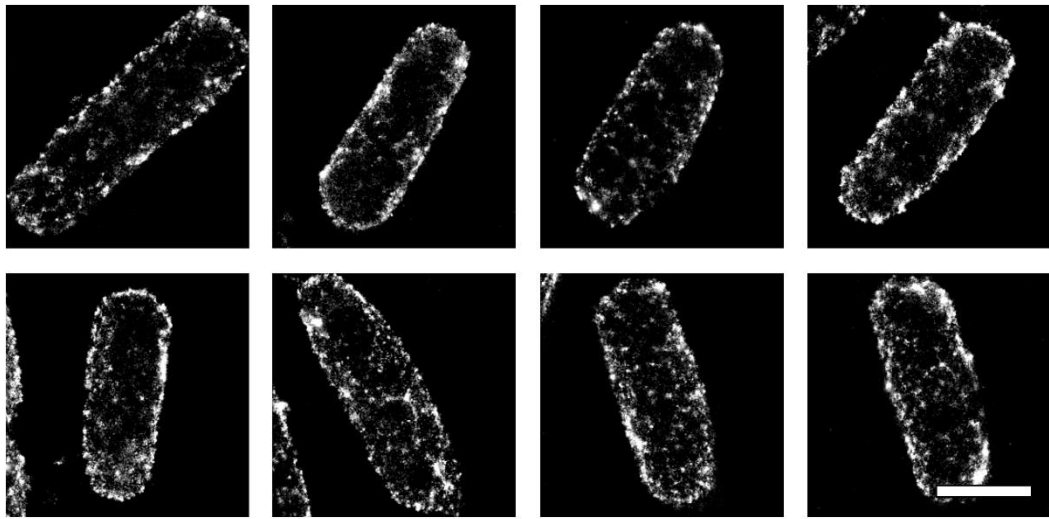
Figure 3.20 Single molecule localization imaging of BamC in *E. coli* Δ*bamB* mutants. RapidSTORM reconstructed super resolution images of BamC distribution in representative Δ*bamB* mutant cells. Scale bar 1 µm.

This phenotype of the Δ*bamB* mutants was complemented by low copy number (pACYC-Duet-*bamB*) (Stubenrauch et al., 2016) and high copy number (pGEM-T-*bamB-His₆*) plasmid expression of recombinant BamB (Figure 3.20B and 2.23). Cluster analysis performed on *d*STORM images confirmed that these complemented samples indeed showed average cluster measurements of cluster density, cluster area, cluster diameter and percentage localizations in clusters close to the wildtype BAM clusters levels (Figure 3.21 and 3.22). The nearest neighbour distances were calculated to be approximately the same across all the samples.

ΔbamB, pACYC-bamB
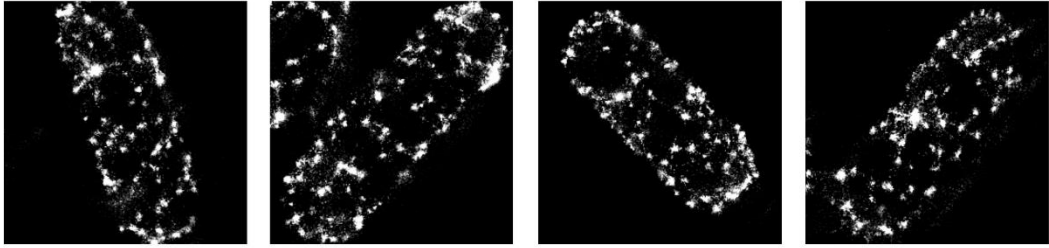
ΔbamB, pGEM-T-bamB
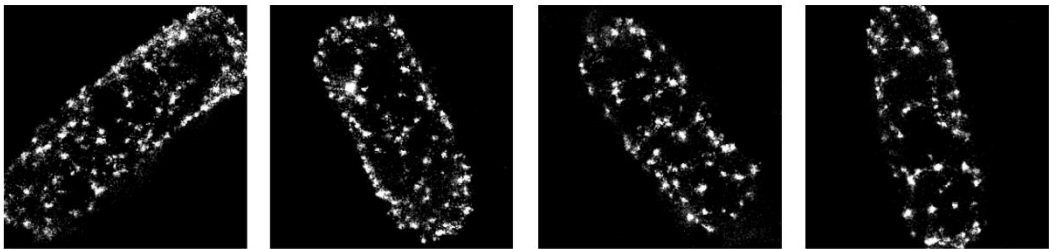
ΔbamB, pGEM-T-bamB(L192S,L194S,R195A)
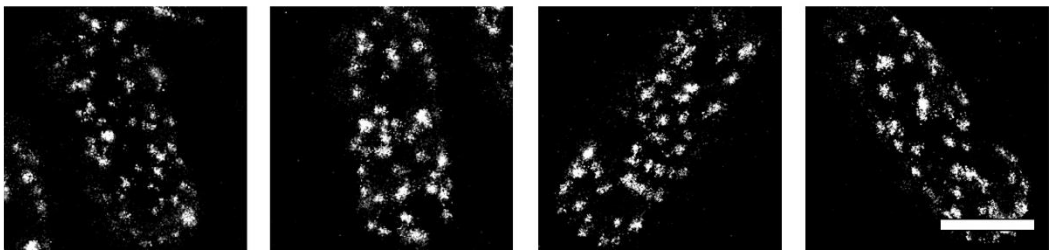
Figure 3.21 Single molecule localization imaging of ΔbamB E.coli microscopy phenotype complementation. *d*STORM imaging of BamB complementation using plasmids expressing recombinant *bamB* (see methods). Scale bar 1 µm. All *d*STORM images are shown at the same exposure level to facilitate comparison.
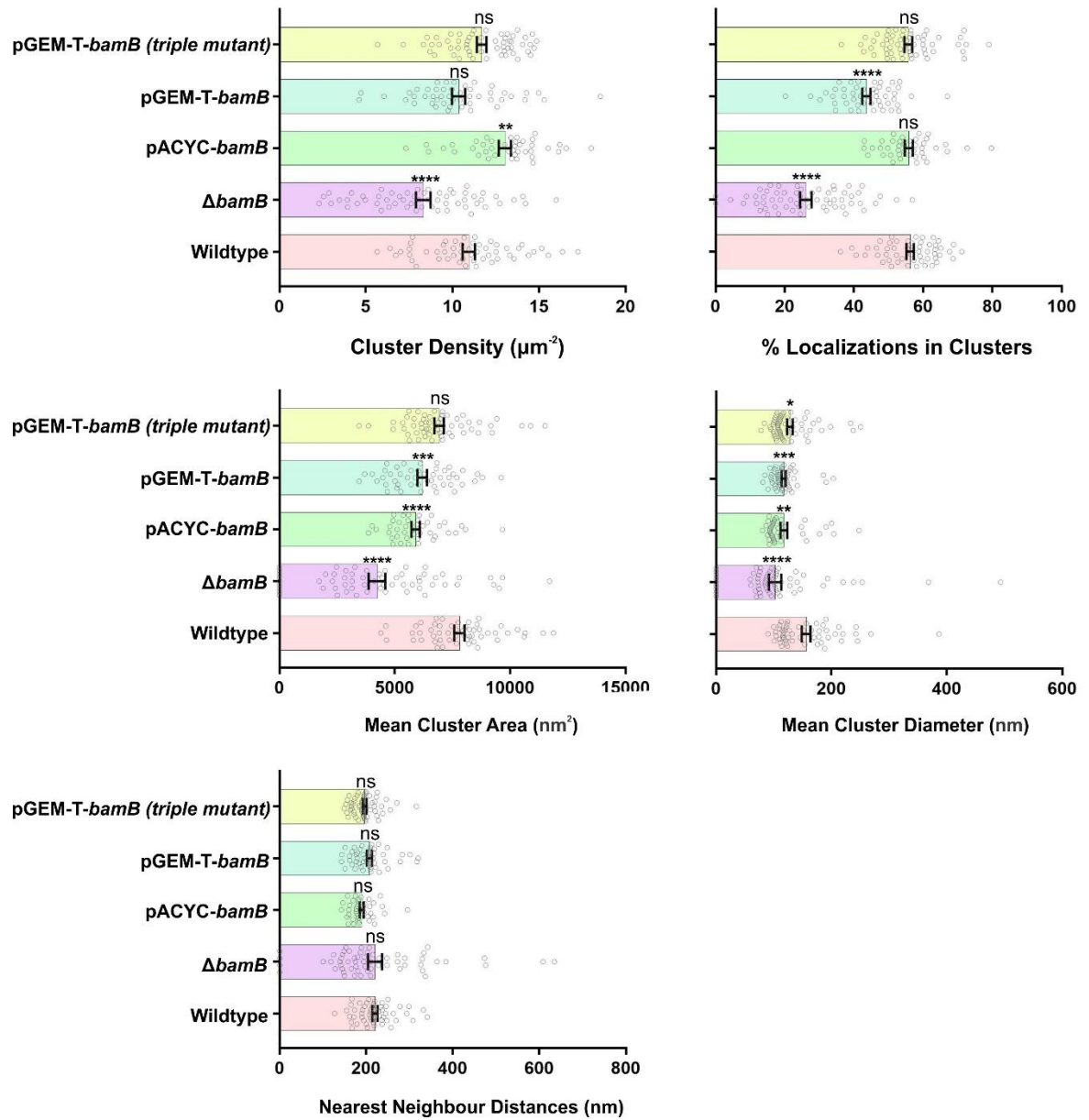
Figure 3.22 Cluster analysis of BamC in *E. coli* Δ*bamB* mutants. Cluster analysis comparing BamC distribution in wild type *E. coli*, Δ*bamB* mutant and *bamB* complementation. (*L192S,L194S,R195A)* = (Triple mutant). Error bars shown as mean ± SEM. Statistical significance reported by P values were calculated in comparison with the BamC Wildtype: ns = P > 0.05, * = P ≤ 0.05, ** = P ≤ 0.01, *** = P ≤ 0.001, **** = P ≤ 0.0001.
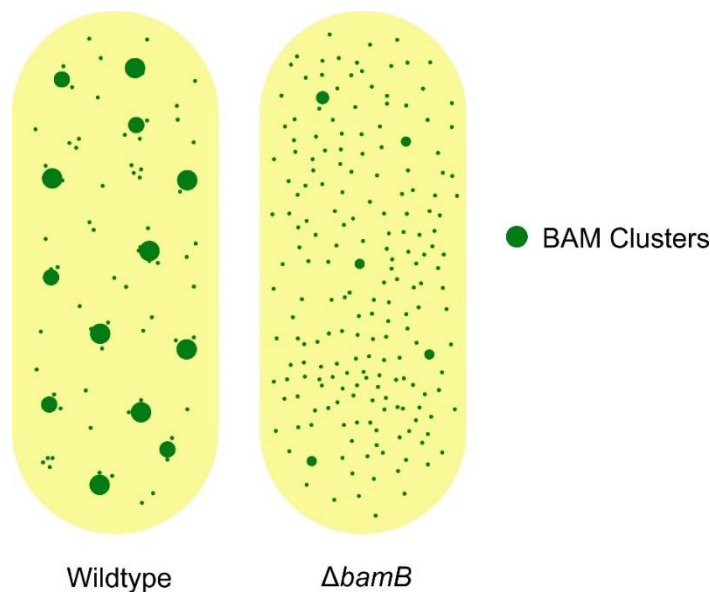
Figure 3.23 Schematic diagram showing BAM complex clustering levels in wildtype cells and in Δ*bamB* mutants. The large green spots represent BAM complex clusters and the small green spots represent induvial BAM complexes and/or remnant BAM complex clusters.

If in fact these interactions are being mediated through BamB, a defective BamA-BamB interaction should closely mimic the Δ*bamB* microscopy phenotype where BAM clustering has been significantly diminished. Using co-immunoprecipitation of BamA with histidine tagged BamB variants, Vuong *et al*., suggested that a triple mutation in BamB: L192S, L194S and R195A (*bamB*-triple mutant) results in a defective BamA-POTRA-BamB propeller interaction, creating a "*bamB*-null phenotype" (Vuong et al., 2008). In attempt to further investigate our hypothesis, I used the afore-mentioned *bamB*-triple mutant as a control (Plasmid information Table 2.0). BN-PAGE analysis carried out on total membranes isolated from *bamB* mutants revealed that the *bamB*-triple mutant partially, though not completely restored BamB interactions with the detergent solubilised BAM complex.

Super resolution imaging of Δ*bamB* mutant complemented *bamB*-triple mutant plasmid showed a significant level of BAM clustering similar to wildtype levels (Figure 3.21 and 3.22). This further indicated that BamA-BamB interactions are still occurring in the membrane environment, i.e. that mutations L192S, L194S and R195A in BamB did not completely abolished these interactions.
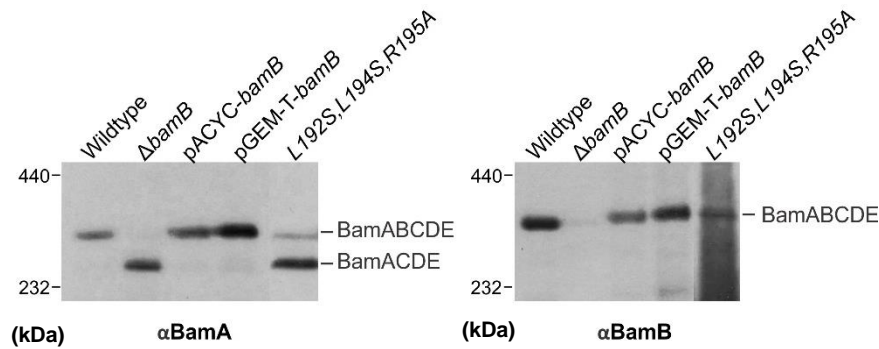
Figure 3.24 BamB plasmid expression in *E. coli* BW25113 Δ*bamB* mutants. BN-PAGE/Immunoblot detection using anti-BamA and anti-BamB showing BamB plasmid expression levels in *E. coli*-K12 BW25113 Δ*bamB* mutants. Holocomplex of BAM (BamABCDE) was detected at a higher molecular weight than the BAM complex lacking BamB subunit (BamACDE).

3.2.7.2 BamE subunit is non-essential to maintain BAM complex clusters.

BamE is the smallest lipoprotein subunit in the BAM complex. It is non-essential, though its absence causes defects in OMP assembly and membrane permeability (Sklar et al., 2007; Lewis et al., 2008). Recent crystal structure of the BAM complex showed BamE interacts with BamA, BamC, BamD, but not BamB (Bakelar et al., 2016; Gu et al., 2016). Curiously, BamE also exists in monomeric and dimeric forms when not in the BAM complex (Albrecht and Zeth, 2011; Kim et al., 2011). Other studies have suggested BamE functions to recruit phosphatidylglycerol to aid OMP assembly (Endo et al., 2011; Knowles et al., 2011).

*d*STORM imaging performed on *E. coli* Δ*bamE* mutants fluorescently labelled with anti-BamC showed similar BAM clustering patterns to those observed in wildtype cells (Figure 3.24). Further, cluster analysis did not show any significant differences between wildtype and Δ*bamE* BAM clustering, except for the mean cluster area (reduced by 30%) and the proportion of localizations within clusters (reduced by 37.3%) (Figure 3.25). This led me to conclude that BamE did not play a significant role in organizing BAM complex clusters at the cell surface of *E. coli*.
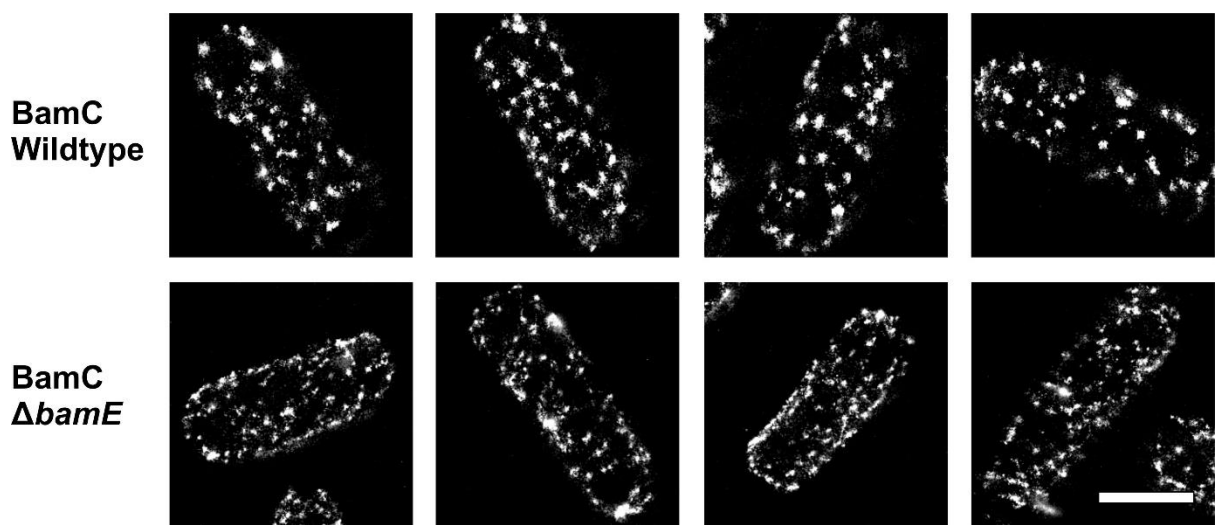
Figure 3.25 Single molecule localization imaging of BamC in *E. coli* Δ*bamE* mutants.
BamC clustering in Δ*bamE* was similar to Wildtype pattern. Scale bar 1 μm.
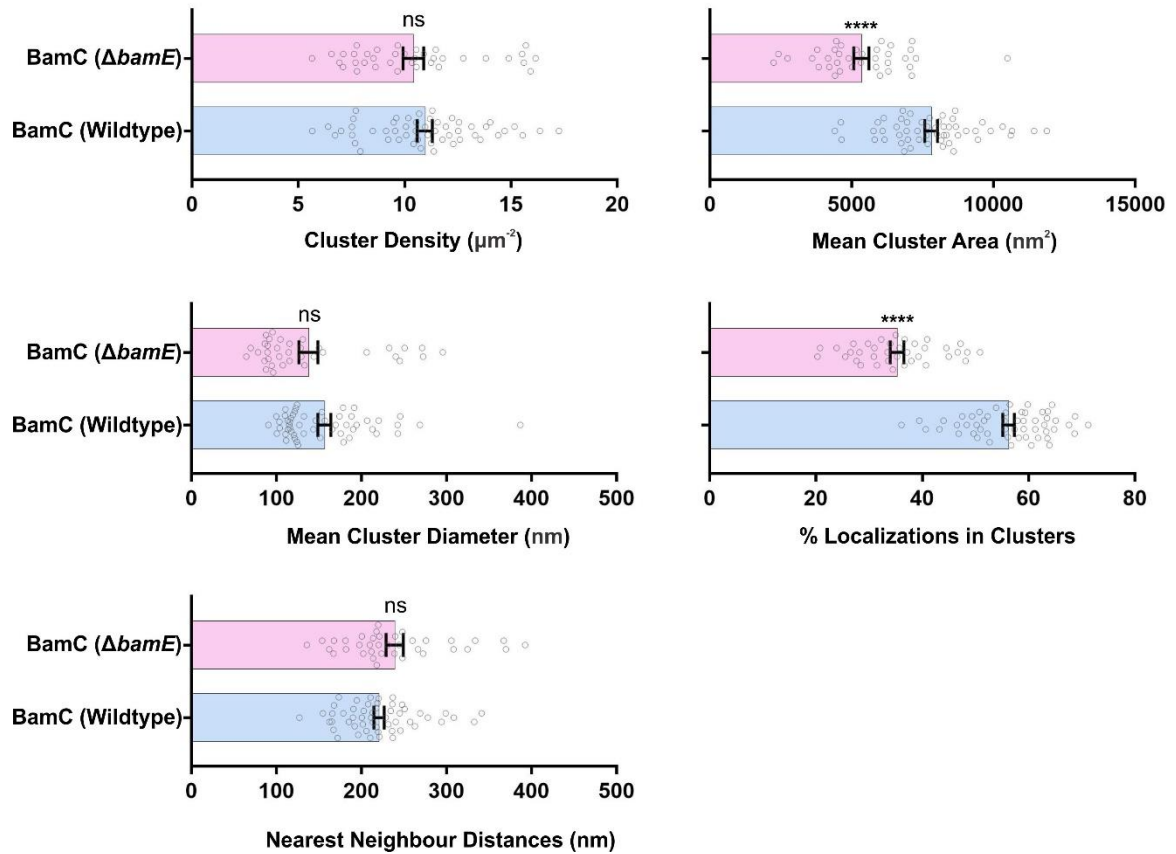
Figure 3.26 Cluster analysis of BamC in *E. coli* Δ*bamE* mutants. Error bars shown as mean ± SEM. Statistical significance reported by P values were calculated in comparison with the BamC Wildtype: ns = P > 0.05, * = P ≤ 0.05, ** = P ≤ 0.01, *** = P ≤ 0.001, **** = P ≤ 0.0001.

3.3 Discussion

With the current super resolution microscopy data it was apparent that the observed clusters represent the distribution of the BAM complex across the *E. coli* cell surface. Given the approximate number of each BAM subunit [~300 per cell; (Wisniewski and Rakus, 2014)], the average surface area of an *E. coli* cell [~6 μm^2; (Sundararaj et al., 2004)] and the number of BAM clusters observed by *d*STORM imaging (~10 per μm^2), I suggest that there are several BAM complexes located within each cluster.

In light of super resolution microscopy evidence collected here from *E. coli* mutants lacking non-essential BAM complex lipoprotein subunits (BamB and BamE), I conclude that BamB subunit plays a more crucial role in maintaining BAM clusters than BamE. This was evident from the dramatically reduced number of BAM clusters observed in Δ*bamB* mutants of *E. coli*. Hypothetically, in creating these clusters, BAM:BAM interactions that were mediated through BamB may take place in two ways. If, like Sec13 (Miller, 2013) and other architecturally important β-propeller proteins, BamB sits at the vertices of BAM:BAM clusters then the β-strand interactions would occur in two ways. BamB can interact with another neighbouring BamB subunit or a BamA subunit in proximity via the POTRA domain region (Figure 3.27).
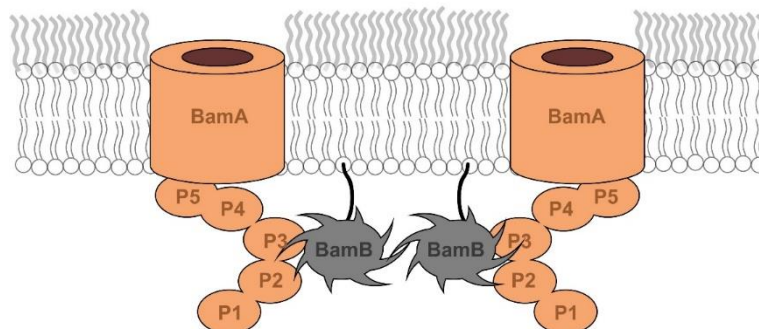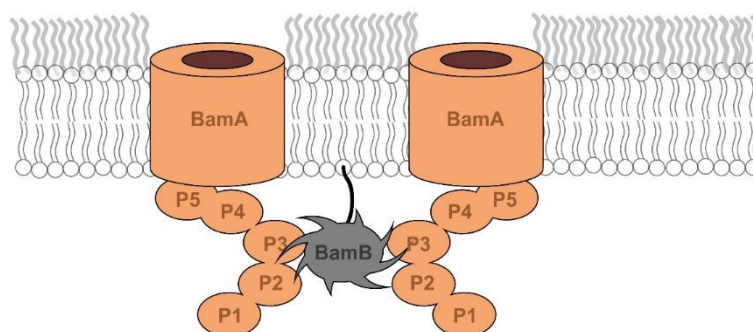
Figure 3.27 Hypothetical model depiction of BAM:BAM interactions mediated through BamB. In model 1, BAM:BAM interactions occur through two neighbouring BamB molecules. Model 2 requires only one BamB subunit and the participation of a neighbouring BamA POTRA domain to mediate these interactions.

3.4 Conclusion

I conclude that the clusters visualized by super-resolution microscopy are an intrinsic property of the BAM complex culminating in assembly precincts in the outer membrane. These precincts of β-barrel protein assembly are situated across the cell surface, and provide a means by which β-barrel proteins are populated into the outer membrane to ultimately congregate into rafts that move (Rassam et al., 2015), forced by membrane growth (Ursell et al., 2012), towards the bacterial cell poles.
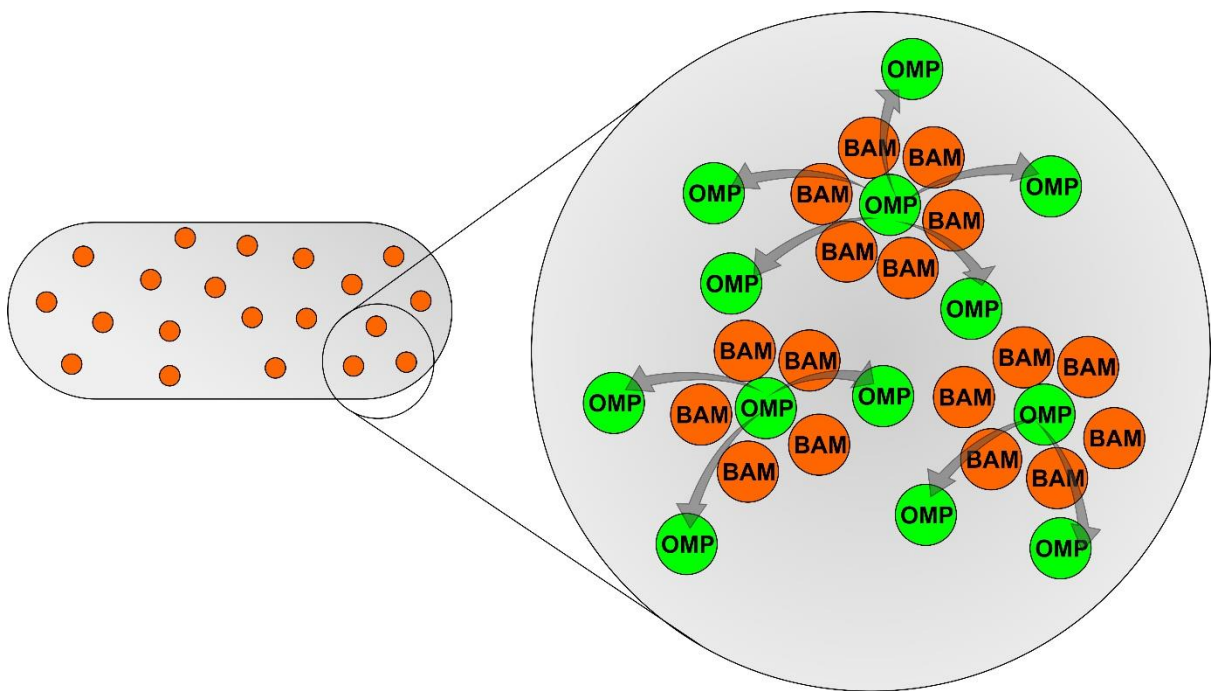
Figure 3.28 BAM complex assembly precincts in the outer membrane. Left; *E. coli* bacterium showing spatial clusters of BAM complexes at the cell surface. Right; magnified view of the spatial clusters showing the Protein Assembly Precincts formation at the outer membrane.

The putative BAM:BAM interactions mediated by BamB may be important in coordinating the activities of several BAM complex protomers spatially because (i) several BAM complexes work in collaboration on a single molecule of substrate, and/or (ii) the assembly of oligomeric substrates require a spatially constrained system to deliver the individual sectors for the oligomeric β-barrel structure (Selkrig et al., 2014). Cluster

analysis showed that the BAM complex clusters grow when outer membrane protein synthesis is at maximal. This is a visual proof that the precincts are active in protein assembly.

Finally, this nanoscale interrogation of the BAM complex *in situ* suggests a new model whereby bacterial outer membranes contain highly organized assembly precincts to drive integral protein assembly, a cellular process that needs to occur in the absence of chemical energy sources such as ATP. For in-depth analysis, these nanoscopic observations should also be validated by mutagenesis, biochemical and structural biological studies. In the next chapter I have used a combination of these approaches to provide more evidence to support the current paradigm of supramolecular assembly of the BAM complex in *E. coli* outer membrane.

Table 3.1 Key statistical figures from BAM cluster analysis.

Sample	Sample size (N)	Average cluster density (μm^{-2})	Average Mean cluster area (nm^2)	Average Mean cluster diameter (nm)	Average % localizations within clusters	Average nearest neighbour distances (nm)
BamC (Wildtype)	53	10.94 ± 0.4	7801 ± 221.2	156.3 ± 7.5	$56.22 \pm 1.1\%$	220.4 ± 6.0
BamC (0.001% digitonin)	77	11.56 ± 0.3	7074 ± 202.5	156.3 ± 6.7	$54.24 \pm 1.1\%$	211.1 ± 4.2
BamC (0.001% tritonX-100)	42	11.10 ± 0.3	7582 ± 292.5	155.7 ± 10.2	$53.70 \pm 1.3\%$	212.4 ± 5.9
BamC (rifampicin)	42	14.65 ± 0.4	6303 ± 200.4	125.5 ± 6.2	$68.01 \pm 1.5\%$	173.2 ± 4.2
BamC (ΔbamB::Kan)	61	8.316 ± 0.4	4232 ± 353.7	102.2 ± 10.7	$26.11 \pm 1.6\%$	220.6 ± 16.0
BamC (ΔbamB::Kan, pACYC-Duet-bamB)	41	13.02 ± 0.4	5906 ± 180.9	117.5 ± 6	$55.83 \pm 1.1\%$	189.5 ± 4.6
BamC (ΔbamB::Kan, pGEM-T-bamB-His₆)	48	10.36 ± 0.4	6193 ± 205.3	117.3 ± 3.5	$43.58 \pm 1.2\%$	207.2 ± 6.0
BamC (ΔbamB::Kan, pGEM-T-bamB(L192S,L194S,R195A)-His₆	57	11.69 ± 0.3	6927 ± 202.6	127.9 ± 4.8	$55.68 \pm 1.1\%$	196.5 ± 4.1
BamA (0.001% digitonin)	46	13.54 ± 0.4	6363 ± 278.7	130.2 ± 9.1	$64.45 \pm 1.6\%$	175.3 ± 5.2
BamA (0.001% tritonX-100)	48	12.13 ± 0.4	7184 ± 289.3	155.8 ± 9.3	$65.32 \pm 1.6\%$	155.8 ± 9.3

$\pm$ Standard Error of Mean (SEM)

Sample size, n > 40

Chapter 4: Characterisation of non-canonical BamB interactions with BAM complex components in *E. coli* using *in situ* crosslinking methods.

4.1 Introduction.

As briefly introduced in previous sections, BamB is a non-essential sub component of the BAM complex. The structure of BamB from *E. coli* has been solved and found to be an 8-blade beta-propeller containing WD-40 repeat motifs (Heuck et al., 2011; Kim and Paetzel, 2011; Noinaj et al., 2011). Proteins containing WD-40 domains are known to serve as protein-protein or protein-DNA interaction platforms in cellular processes (Xu and Min, 2011). From crystal structure and genetic data, BamB is known to have direct interactions with BamA (Malinverni et al., 2006; Kim et al., 2007; Kim and Paetzel, 2011; Jansen et al., 2015; Chen et al., 2016).

From recent work, there are many independently solved crystal structures of BamB from *E. coli*, *Moraxella catarrhalis* and *Pseudomonas aeruginosa*, all showing similar beta-propeller architectures (Albrecht and Zeth, 2011; Heuck et al., 2011; Kim and Paetzel, 2011; Noinaj et al., 2011; Jansen et al., 2012; 2015; Chen et al., 2016; Gu et al., 2016; Han et al., 2016)(PDB:4IMM). Each propeller blade consists of four anti-parallel β-strands. This highly symmetric protein is asymmetrically decorated by circumferential loops extending from the top and the bottom face of BamB. Top face loops are much longer (5-19 residues) than the bottom face (~3 residues), and are known to be involved in joining the adjacent blades of the propeller. To be consistent with convention, these are here and after known as interconnecting loops – IL (Heuck et al., 2011). Interestingly, some of the most conserved residues among BamB homologs are located in these loops (Kim et al.,

2007; Gatzeva-Topalova et al., 2008; Knowles et al., 2008; Noinaj et al., 2011; Dong et al., 2012; O'Neil et al., 2015). Electrostatic potentials indicate that BamB has a predominantly negatively charged surface, with the central core of the propeller having the highest density of electronegative residues (Chen et al., 2016).
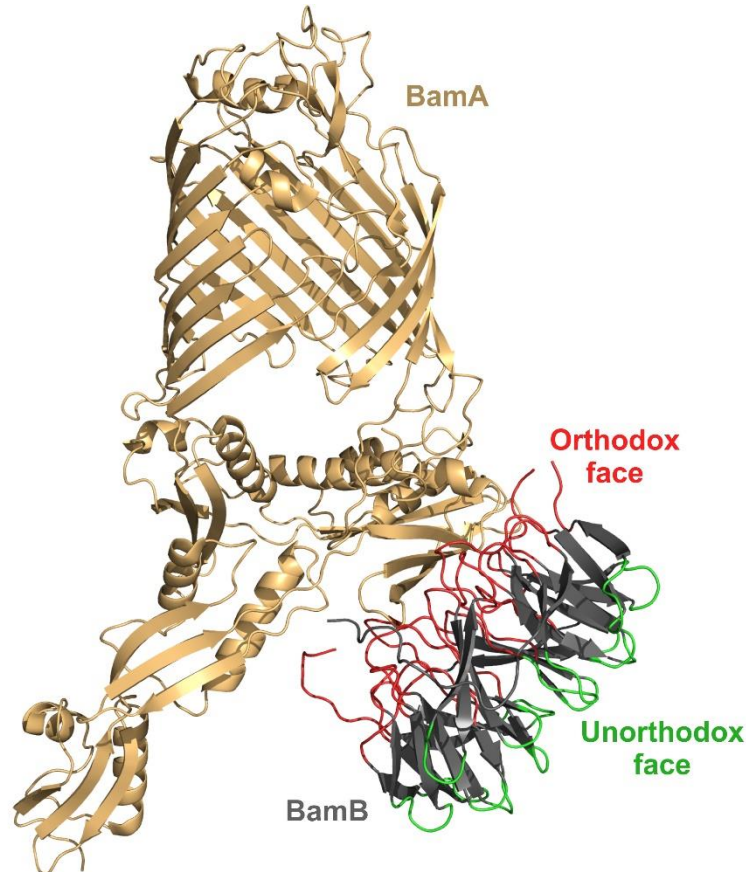
Figure 4.1 BamA-BamB crystal structure (PDB: 5ayw). BamB interacts with BamA-POTRA domains through the orthodox face loops (colour coded in red). Interaction interface opposing the POTRA domains is known as the unorthodox face of BamB (green).

BamA, the core component of the BAM complex, has five N-terminal POTRA domains exposed to the periplasmic space and this domain interact with BamB. Each of the five POTRA domains have similar 3-stranded beta sheet elements (Kim et al., 2007; Gatzeva-Topalova et al., 2008; Zhang et al., 2011). They function like scaffold to mediate

interactions between other sub components of the BAM complex. BamA has been shown to directly interact with BamB and form BamAB sub-complex, which can be purified and reconstitute back to form the holo BAM complex with BamCDE sub complex *in vitro* (Hagan et al., 2010b). Mutagenesis studies have shown POTRA3-5 are important for *E. coli* cell viability and also to maintain interactions with BamB (Kim et al., 2007; Dong et al., 2012). Further, these studies were able to identify BamA-BamB interactions through BamB residues L192, L194, R195, D246 and D248 (Vuong et al., 2008; Chen et al., 2016), with these critical residues located in IL4 and IL5. High B-factor values reported for these regions indicate their highly flexible nature within the BamB structure (Noinaj et al., 2011). Conversely, residues D241 and L247 in BamA-POTRA3 has been reported to be essential in maintaining interactions with BamB (Kim et al., 2007). Superposition of current POTRA domain crystal structures (PDB: 2QCZ, 3EFC and 4K3B) indicates a potential for dynamic movement, with POTRA1-3 being the most flexible regions in the periplasmic space (Chen et al., 2016). Additionally, Dong *et al*., used affinity isolation assays to show that POTRA1-2 do not greatly contribute to BamA-BamB interactions (Dong et al., 2012). Nonetheless, conformations seen in crystal structure PDB: 3EFC suggests that POTRA2 may also be involved in interactions with BamB (Gatzeva-Topalova et al., 2008). Due to its considerably high distance (~40 Å) from BamB, direct interactions with POTRA4-5 is not plausible. Protein docking simulations also suggested the plausibility of BamB IL4 binding with BamA-POTRA3 (Noinaj et al., 2011).

Collectively, the current literature suggests that residues in BamA-POTRA3 and BamB IL4-IL5 are highly relevant in the formation of BamAB sub-complex. Given that BamA-POTRA domains contain 3-stranded beta sheets and each propeller blade in BamB is composed of four anti-parallel β-strands, it seems likely that these interactions are mediated by a beta-augmentation mechanism, in which each propeller blade serve as a

binding surface to a single POTRA domain (Gatzeva-Topalova et al., 2008; Kim and Paetzel, 2011). It is noteworthy to mention that BamA-BamB interactions could also be stabilised via electrostatic interactions, as the BamA-POTRA3 contains an electropositive patch that complements the predominantly electronegative BamB IL4 and IL5 (Figure 4.2) (Noinaj et al., 2011).

Although not essential for bacterial cell viability, BamB is known to be important in maintaining steady-state level of OMPs such as OmpA, OmpF and LamB, and mutants lacking BamB have also been reported to show increased sensitivity to antibiotics (Ruiz et al., 2005; Wu et al., 2005; Charlson et al., 2006). In *in vitro* assays of BAM complex function, the absence of BamB impaired the activity of essential components, BamA and BamD in their catalysis of LptD-LptE assembly (Hagan et al., 2010a; Hagan and Kahne, 2011). Periplasmic chaperons like SurA are known to facilitate nascent outer membrane protein folding in the assembly process. In the absence of SurA or BamB, altered efficiencies have been observed in the outer membrane assembly for two proteins LamB and FimD (Ureta et al., 2007; Palomino et al., 2011). While single SurA or BamB deletion strains showed partial reduction in beta-barrel assembly, simultaneous deletions of BamB and SurA leads to a synthetic lethal phenotype (Ureta et al., 2007). Despite their functional overlaps in OMP assembly, direct BamB-SurA interactions have not been observed. Although BamA-SurA interactions have been reported, they seem to be independent of BamB and considered to be involved in a docking step leading to a substrate handover directly from SurA to BamA-POTRA domains (Bennion et al., 2010). Moreover, loss of BamB does not affect these BamA-SurA interactions. It is therefore apparent that BamB assists the assembly of beta-barrel proteins at a stage in the process independent of SurA, and does not involve direct contact with SurA. Nonetheless, latent stage interactions of BamB has also been reported. Ieva *et al*., studies showed BamB and BamD are in

proximity to the beta-barrel domain of autotransporter EspP, only after the cleavage of N-terminal passenger domain (Ieva et al., 2011). These interactions imply that BamB functions at later stages of OMP assembly, but the significance of these interactions in OMP assembly remains elusive.
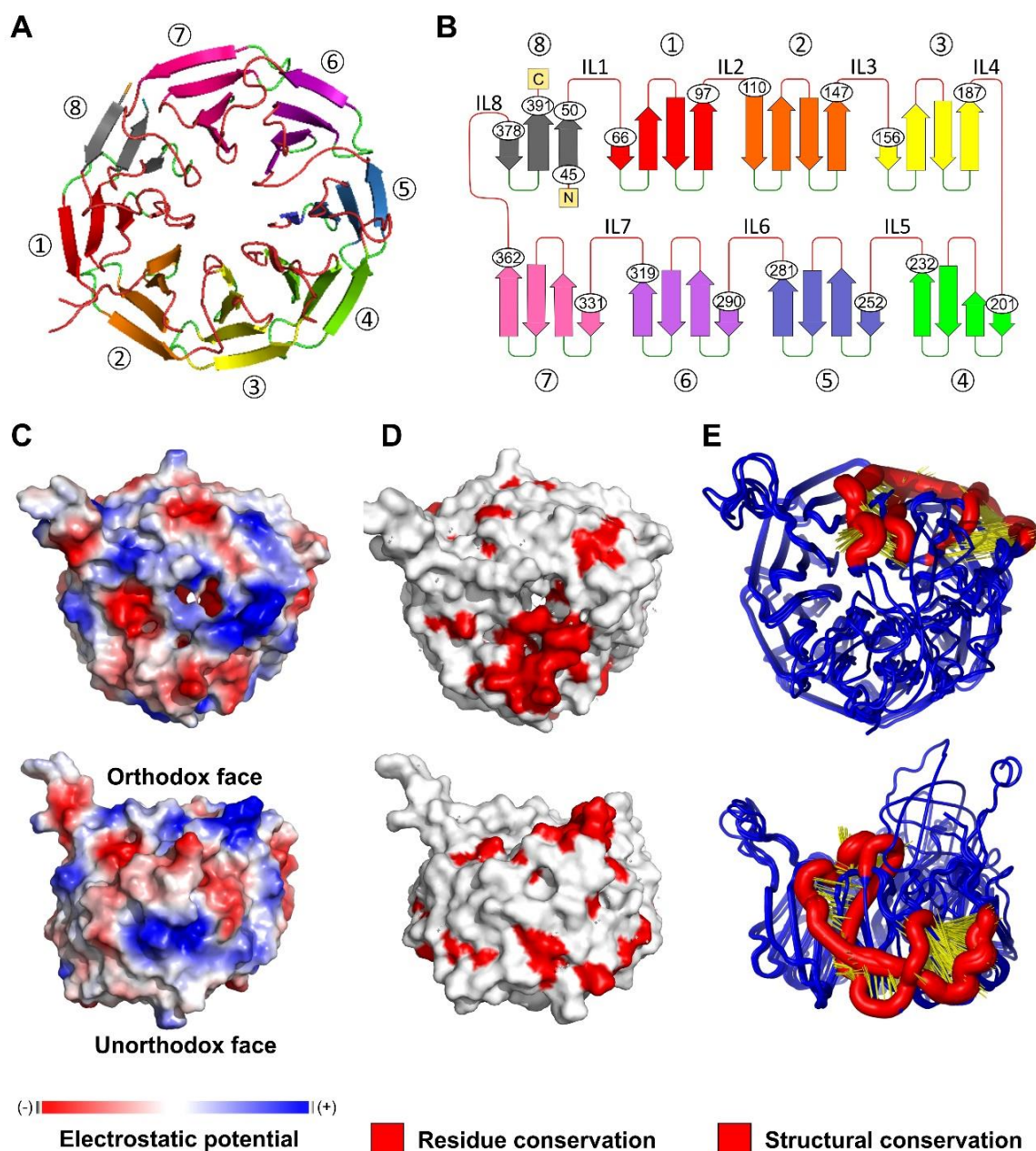
Figure 4.2 BamB β-propeller crystal structure characteristics (PDB: 5ayw). (A) Colour coded (1)-(8) propeller blades in the BamB. **(B)** Topology diagram of BamB based on the crystal structure. Inter-connecting loops (IL1-IL8) and orthodox (Red) and unorthodox (Green) face loop residues. **(C)** Electrostatic potential surface map of BamB. **(D)** Conserved residues (red) mapped onto BamB crystal structure surface. **(E)** Mapping structurally conserved regions in BamB, based on structural alignment of current BamB crystal structures (PDB: 3P1L, 3PRW, 3Q7M, 3Q7N, 3Q7O, 2YH3, 2Q54).
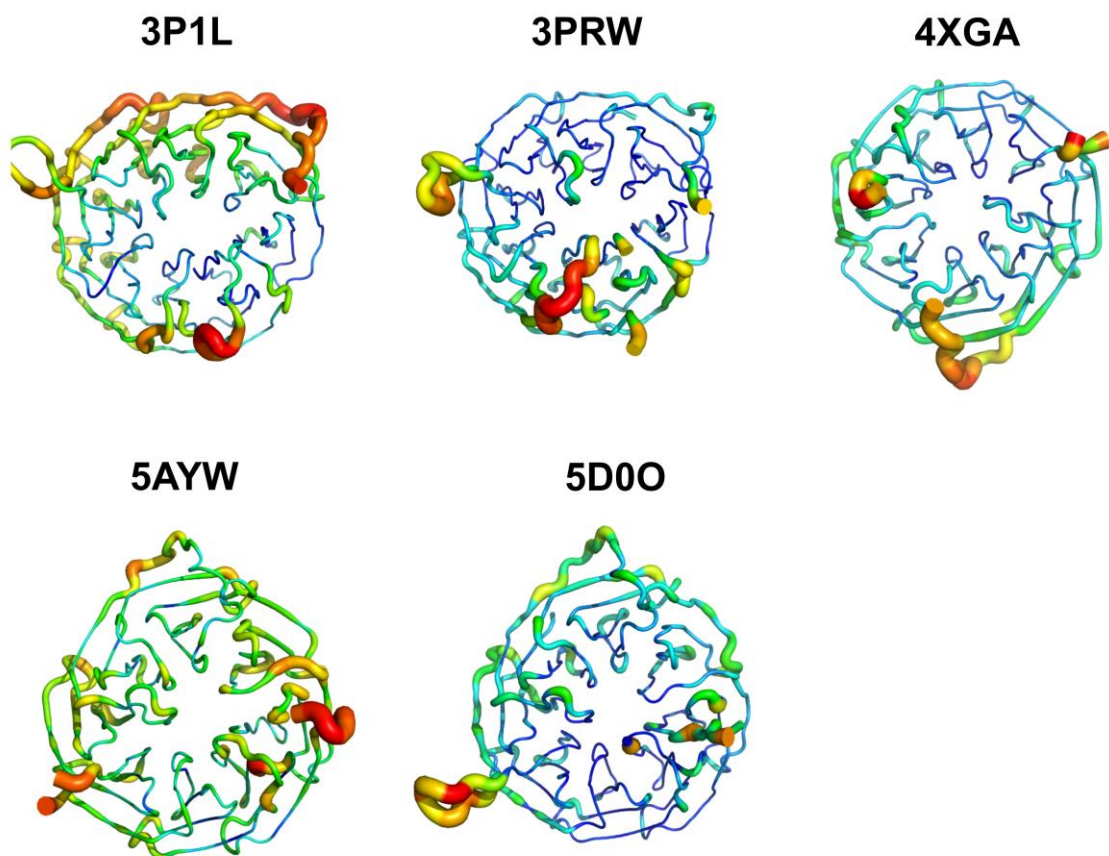
Figure 4.3 B-factor putty representation of BamB crystal structures. IL2, IL5 and unorthodox face short loop 87-89 showed the highest recorded B-factors. However, this is not consistent with all the crystal structures.

Apart from the biochemically defined role in OMP biogenesis, BamB is also known to have indirect roles in bacterial pathogenicity. For example, in *Salmonella enterica*, Δ*bamB* mutants have a defect in type III secretion system expression affecting the virulence function (Fardini et al., 2007). More recently, BamB has been implicated to have a role in facilitating type-1 fimbriae production and cell adherence during *Klebsiella pneumoniae* infection (Hsieh et al., 2016).

In light of the current literature, it is apparent that BamB has direct interactions with BamA, and functions to enhance the OMP assembly process. As a result of this key functions, the absence of BamB can lead on to a number of pleiotropic phenotypes

including inefficient beta-barrel protein assembly at the outer membrane, changes in the outer membrane permeability causing increased susceptibility to antibiotics, impaired expression of secretion systems affecting bacterial virulence, as well as the spatial organization of the BAM complex on the cell surface of *E. coli* (see Chapter 3). The question remains, whether these phenotypes are directly influenced by impaired BamA-BamB interactions (Namdari et al., 2012).

In Chapter 3, I described the existence of BAM complex cluster precincts on *E. coli* cell surface using super resolution microscopy. I also uncovered the essential role played by BamB lipoprotein subunit in organizing these precincts. A model was proposed whereby BamB mediates these BAM:BAM cluster interactions through two neighbouring BamB molecules and/or by BamB interactions with the POTRA domain of a neighbouring BamA. Such interactions have not been reported in previous studies. In this section, by taking the advantage of genetic code expansion tools and site directed mutagenesis approaches, I sought to investigate these non-canonical interactions in the BamB-propeller that might mediate BAM:BAM interactions *in vivo* which in turn may illustrate the formation of BAM complex clusters in the outer membrane.

4.2 Results

4.2.1 Mapping conserved residues onto BamB crystal structure (Bioinformatics).

A multiple sequence alignment of BamB homologs from 21 species of Proteobacteria species was performed as described in Chapter 2, section 2.2.7. Residues having a conservation score of 7 or above were mapped onto the secondary protein structure of BamB, followed by mapping onto the 3-dimensional structure.
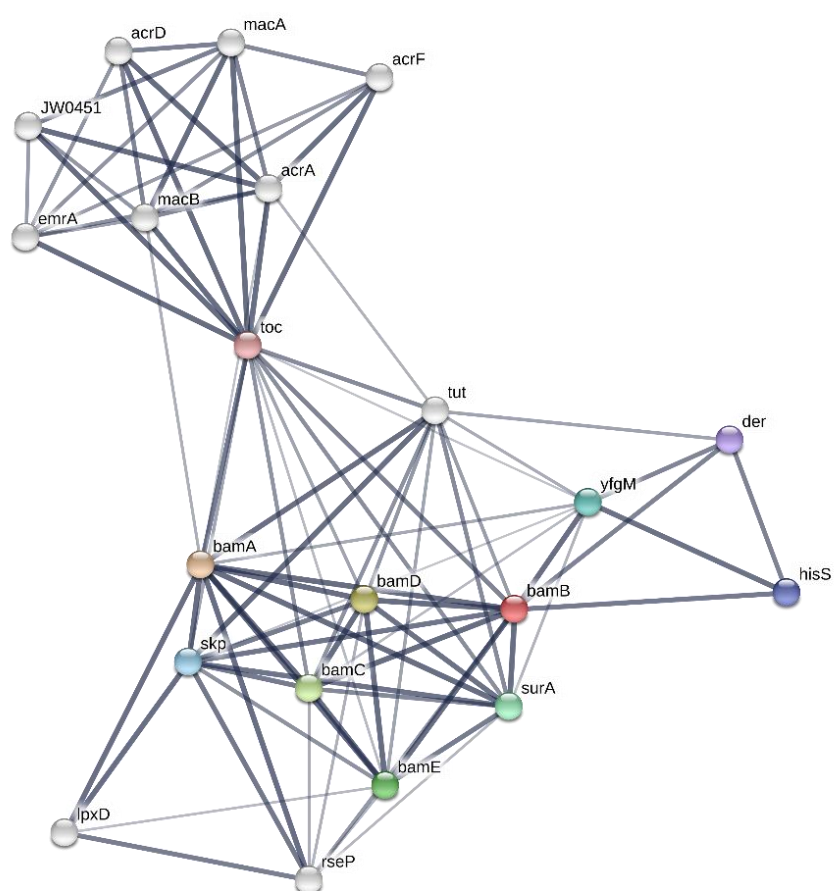
Figure 4.4 *bamB* gene synteny. The protein sequence of the *E. coli* K-12 (MG1655) gene annotated as *bamB* was used to search the STRING v10.5 database for putative functional protein partners. The required confidence score was set at a medium confidence level (0.400). String line thickness represent the strength of data support. Maximum number of interactions to display was set to no more than 10 for the 1st and 2nd shell.

UNIPROT|P77774|BAMB_ECOLI/1-392
UNIPROT|C6BGE7|BAMB_RALP1/1-392
UNIPROT|Q0A984|BAMB_ALKEH/1-383
UNIPROT|Q8EC35|BAMB_SHEON/1-395
UNIPROT|Q5NIB1|BAMB_FRATT/1-456
UNIPROT|Q7VWL3|BAMB_BORPE/1-386
UNIPROT|Q7CJM5|Q74S85|BAMB_YERPE/1-393
UNIPROT|Q63UT0|BAMB_BURPS/1-381
UNIPROT|G4Q9J6|BAMB_TAYAN/1-384
UNIPROT|Q5X521|BAMB_LEGPA/1-384
UNIPROT|Q9K TW8|BAMB_VIBCH/1-386
UNIPROT|Q32D50|BAMB_SHIDS/1-392
UNIPROT|H9L451|BAMB_SALTY/1-392
UNIPROT|C7R5S3|BAMB_KANKD/1-388
UNIPROT|E4PKG3|BAMB_MARAH/1-390
UNIPROT|Q9HXJ7|BAMB_PSEAE/1-380
UNIPROT|Q8P980|BAMB_XANCP/1-406
UNIPROT|Q5E769|BAMB_VIBF1/1-385
UNIPROT|F8GAQ8|BAMB_FRAST/1-521
UNIPROT|F5ZAY7|BAMB_ALTNA/1-418
UNIPROT|Q0AE45|BAMB_NITEC/1-409

Conservation

112

Figure 4.5 Sequence alignment of selected BamB proteins. High to low conservation of residues were indicated from red to white in background. The conserved columns with the highest score are indicated by '*' (Score = 11). Columns with a score of 10 that contained mutations but all properties were conserved, marked with a '+'. Residues with conservation scores ranging from 7-11 annotated in Blue boxes. Protein sequences were acquired from the Uniprot database; *Escherichia coli* (P77774), *Ralstonia pickettii* (C6BGE7), *Alkalilimnicola ehrlichii* (Q0A984), *Shewanella oneidensis (*Q8EC35), *Francisella tularensis subsp. Tularensis* (Q5NIB1), *Bordetella pertussis (*Q7VWL3), *Yersinia pestis* (Q7CJM5), *Burkholderia pseudomallei* (Q63UT0), *Taylorella asinigenitalis* (G4Q9J6), *Legionella pneumophila* (Q5X521), *Vibrio cholerae (*Q9KTW8), *Shigella dysenteriae* (Q32D50), *Salmonella typhimurium* (H9L451), *Kangiella koreensis* (C7R5S3), *Marinobacter adhaerens* (E4PKG3), *Pseudomonas aeruginosa* (Q9HXJ7), *Xanthomonas campestris* (Q8P980), *Vibrio fischeri* (Q5E769), *Francisella sp.* (F8GAQ8), *Alteromonas naphthalenivorans* (F5ZAY7), *Nitrosomonas eutropha* (Q0AE45).

As predicted in previous studies, the highest residue conservation on BamB crystal structure was observed in the regions of IL4 and IL5 (Noinaj et al., 2011; Chen et al., 2016) (Figure 4.6).
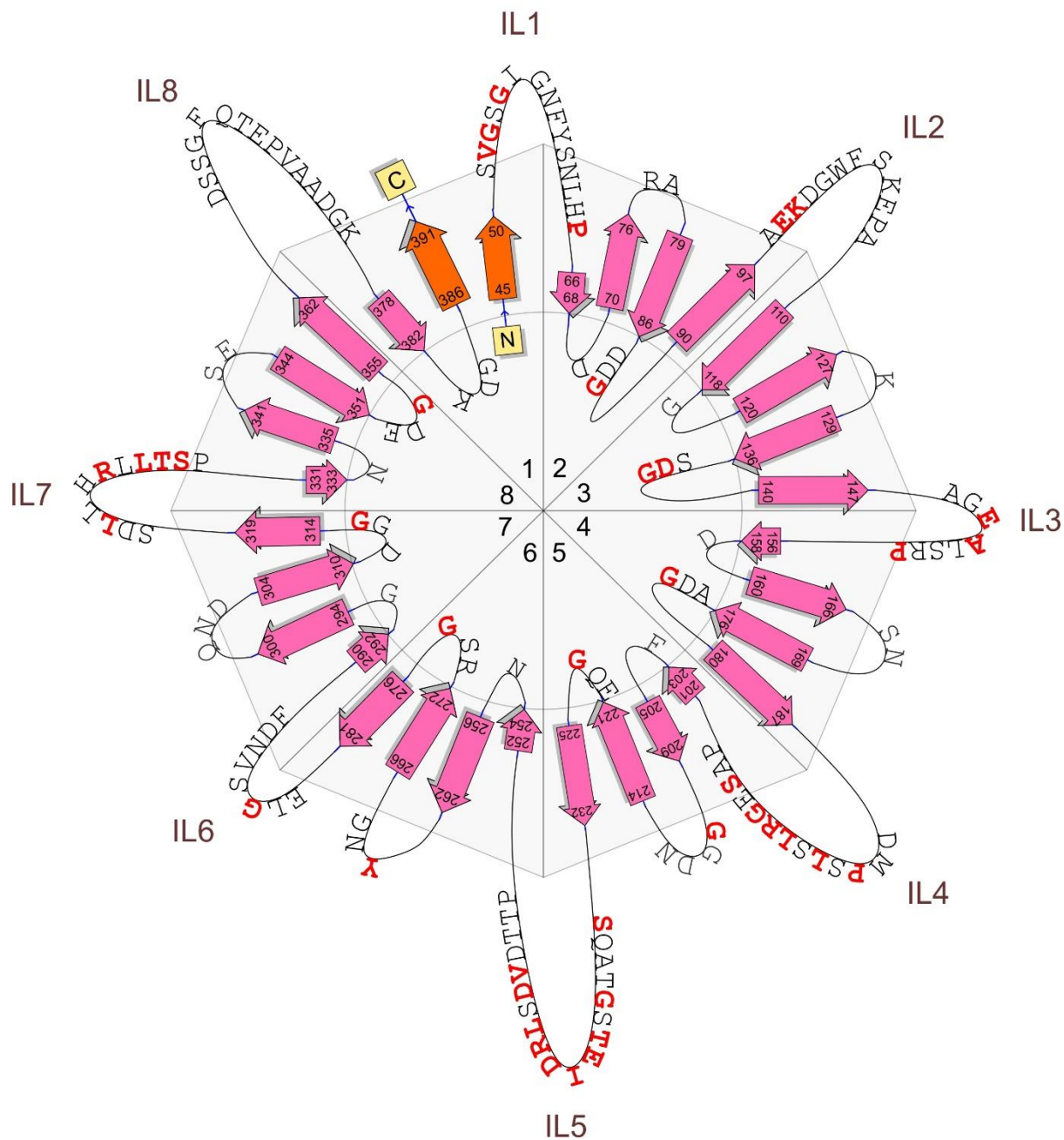
Figure 4.6 Sequence conservation in loop residues of BamB. BamB topology diagram annotated with sequence conserved amino acid residues in red. Inter-connecting loops (orthodox face) face outward from the octagon structure. Unorthodox face loops point inwards and located within the circle.

4.2.2 Orthodox and Unorthodox face loops of BamB.

In the canonical structure of the BAM complex, only the top face of BamB propeller interacts with BamA. I define this as the "orthodox face" with regards to BAM complex interactions. As described earlier, circumferential loops in the orthodox face of BamB, namely IL4 and IL5 play a crucial role in mediating these interactions. However, no studies have yet reported interactions mediated through the bottom face (unorthodox) of BamB, neither with any of the BAM complex subunits, nor possible substrate proteins.
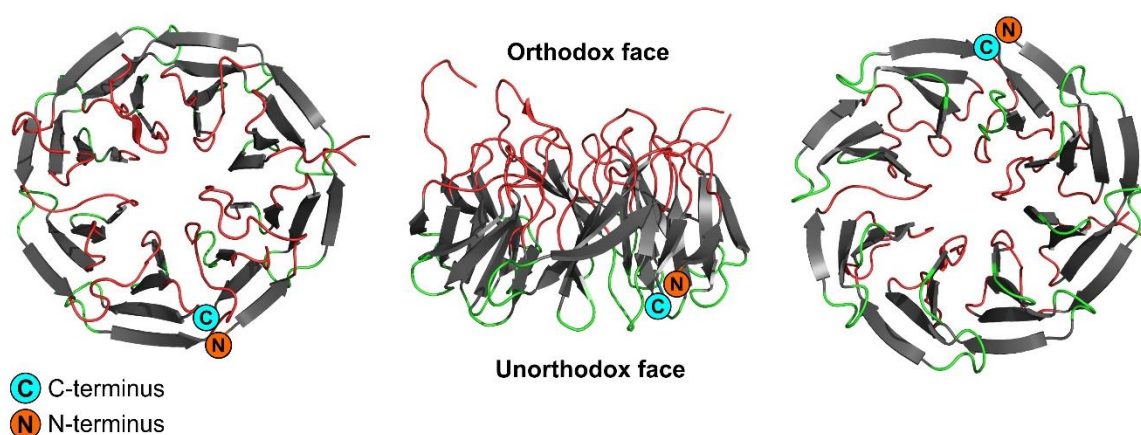
Figure 4.7 Crystal structure of beta-propeller BamB. Orthodox face and unorthodox face loops in BamB are shaded in Red and Green respectively. BamB N-terminal end in Orange and C-terminal end in Cyan (pdb: 5ayw).

Compared to orthodox face loops, unorthodox face loops are much shorter (comprising 3 amino acid residues or less) and do not participate in joining adjacent propeller blades. The observably low B-factor values obtained for these short unorthodox face loops indicate their flexibility is necessarily lower than some of the highly flexible regions in the orthodox face loops (PDB; 3P1L, 5AYW and 5D0O) (Figure 4.4). Interestingly, these unorthodox face loops contain 35% Glycine and 29% Aspartate (Figure 4.10) and according to the multiple sequence alignment (Figure 4.8), many of these Glycine residues were indicated to be highly conserved among Proteobacteria. Glycine residues are

frequently found in beta-sheet turns in many other proteins due to their high flexibility and low steric hindrance caused by their side chains. Furthermore, in BamB almost all of these Glycine residues face the internal cavity of the beta-propeller, making them in accessible for protein-protein interactions. On the other hand, Aspartate residues are charged and often participate in the formation of salt bridges during protein-protein interactions (Donald et al., 2011).

4.2.3 BamB non-canonical interactome mapping using *in situ* photocrosslinking methods.

A plethora of methods are now available to study protein-protein interactions in biological systems. I have utilized *in situ* photocrosslinking approach to characterise possible interactions in the unorthodox face of BamB. This method developed by Schultz and co-workers uses a specially engineered amber suppressor tRNA/tRNA synthetase pair to incorporates photo-activatable phenylalanine derivative, such as p-benzoyl-L-phenylalanine (BPA) into amber codons positions in the protein of interest (Chin et al., 2002; Wang et al., 2006) (Figure 4.8).
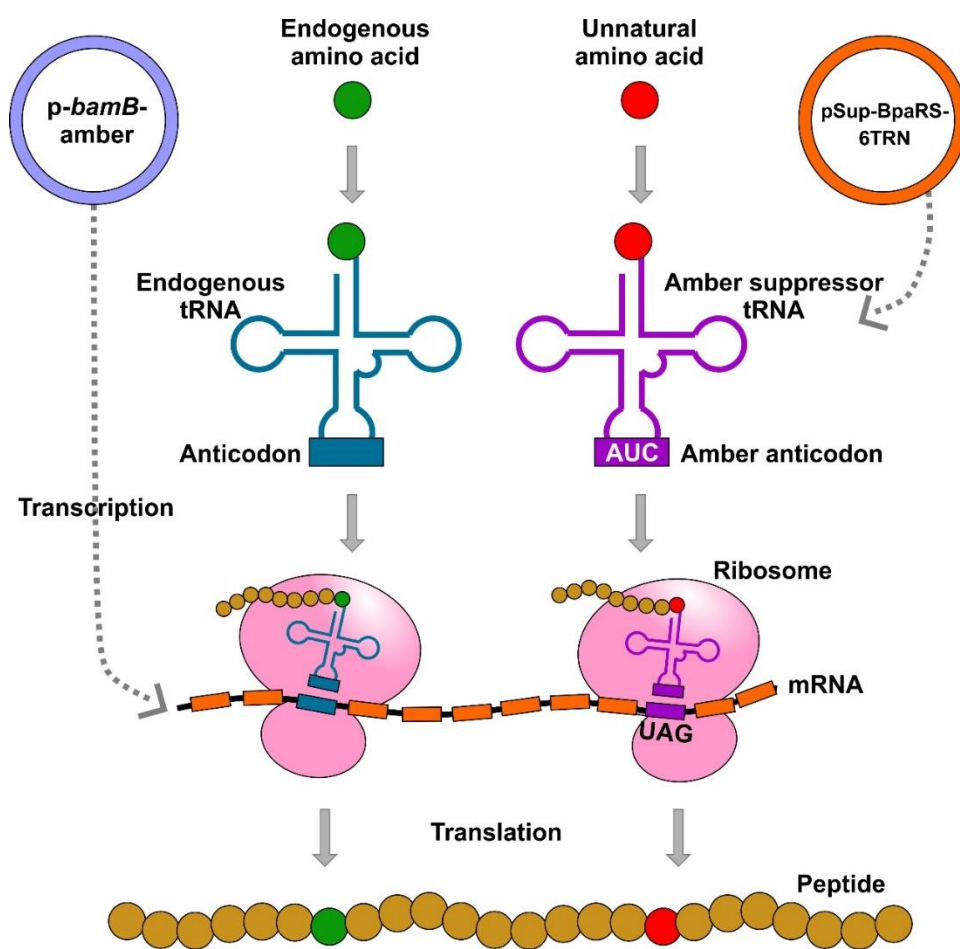
Figure 4.8 Site specific incorporation of photocrosslinkable unnatural amino acids (BPA) into the protein of interest. Specially engineered amber suppressor tRNA/tRNA synthetase pair was used to incorporate unnatural amino acids into the amber codon of a plasmid transcribed mRNA. This mRNA then gets translated into a peptide/protein consisting photocrosslinkable amino acids in specific sites.

Under UV irradiation (350–365 nm), BPA residues in the protein of interest which are close enough (3-8 Å in distance) to form covalent bonds, yield crosslink products (Farrell et al., 2005; Wittelsberger et al., 2008) (Figure 4.12). Hence, this elegant technology offers a physiological method to study protein-protein interaction in live bacteria (Wang et al., 2001). Compared to other crosslinking methods, site specific *in situ* photocrosslinking provides the advantage of being able to analyse protein-protein interactions through

individual segments or individual residues of the protein of interest. In addition, it can be used in parallel with mass spectrometry for unbiased identification of the protein constituents that makeup the crosslink products.
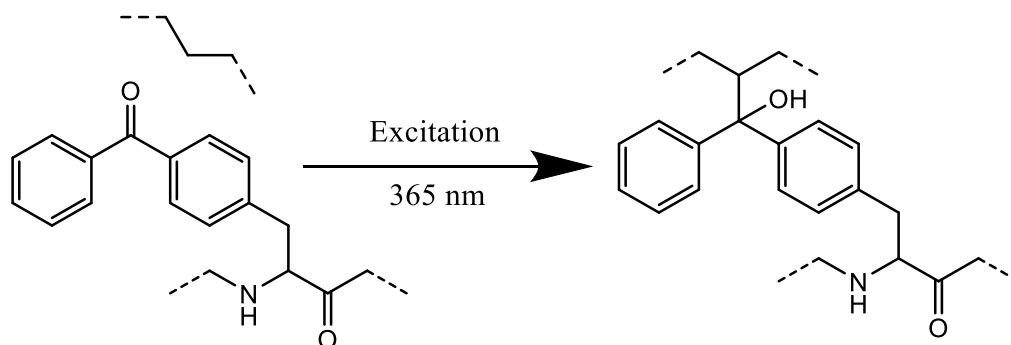
Figure 4.9 Molecular structure of BPA and illustration of photocrosslinking with C-H bond in proximity. Under UV irradiation (365 nm), BPA residues in the protein of interest which are close enough (3-8 Å in distance) to form covalent bonds, yield crosslink products.

4.2.4 Single amber mutation BamB-BPA-photocrosslinking.

BPA residues were incorporated into 40 positions in the *bamB* sequence to generate 40 BPA-alleles, and from these only 29 were viable for *in situ* photocrosslinking studies in *E. coli* (see section 2.2.1). Selection criteria for these 40 residues was based on (i) multiple sequence alignment of BamB homologs to locate conserved residues, (ii) electrostatic potential surface maps of BamB to identify electro-positive and electro-negative amino acid residues, (iii) analysis of BAM complex lattice structure based interactions, (iv) analysis of B-factors (i.e. temperature-factor). Among the BPA incorporation sites, there were 11 positions from the orthodox face (located at IL1, IL2, IL4, IL5, IL7 and IL8) and 18 positons from the unorthodox face of BamB.

Following the *in situ* photcrosslinking protocol described in the methods section, extracts were analysed by SDS-PAGE and immunoblotting using antisera raised against BamA and BamB (see section 2.2.8). Both anti-BamA and anti-BamB immunoblotting showed UV

irradiation produced cross-linked products of approximately 200 kDa when BPA was incorporated at positions 193, 242, 244 and 324 (Figure 4.10 and 4.11). This is larger than the predicted heterodimer of BamA-BamB, calculated to be about ~130 kDa (sum of the molecular masses of BamA, ~90 kDa and BamB, ~40 kDa). However, this seemingly peculiar observation is consistent with observations that crosslinked protein products migrate differently in SDS-PAGE compared to linear polypeptide chains (Farrell et al., 2005; Berg et al., 2014). The fact that I was able to detect these bands with both anti-BamA and anti-BamB, confirms that these were in fact photocrosslinked products of BamA-BamB. Moreover, these crosslinkable residues were heavily concentrated at IL4 and IL5 sites on the BamB structure, which substantiates previous findings in the literature (Kim et al., 2007; Gatzeva-Topalova et al., 2008; Vuong et al., 2008; Noinaj et al., 2011; Dong et al., 2012; O'Neil et al., 2015).

At the unorthodox face, BPA selectively incorporated positions at 90 and 138 also produced photocrosslinked products of BamA-BamB of ~200 kDa) (Figure 4.14). In both anti-BamA and anti-BamB western blots, several fast migrating species were also detected. One possibility is that these are proteolytic fragments of the cross-linked product. Alternatively, these multiple bands could also mean different symmetries of the cross-linked protein (BamA and BamB) at the event of UV irradiation: "X" shaped, "Y" shaped and "T" shaped polypeptides are expected to migrate differently (Farrell et al., 2005). A number of other crosslink products with the size of ~200 kDa was observed at BPA positions 99, 137, 139, 140, 142, 293, 295, 364 and 375 (Figure 4.12). However, they were only detected by anti-BamA and not with anti-BamB antisera. Epitopes of these cross-links are either masked from anti-BamB antibody detection or a protein other than BamB is cross-linked with BamA. Assessment of the presence or absence of other lipoprotein

subunits of the BAM complex in these crosslink products failed to detect BamC, BamD or

BamE (Figure 4.13).
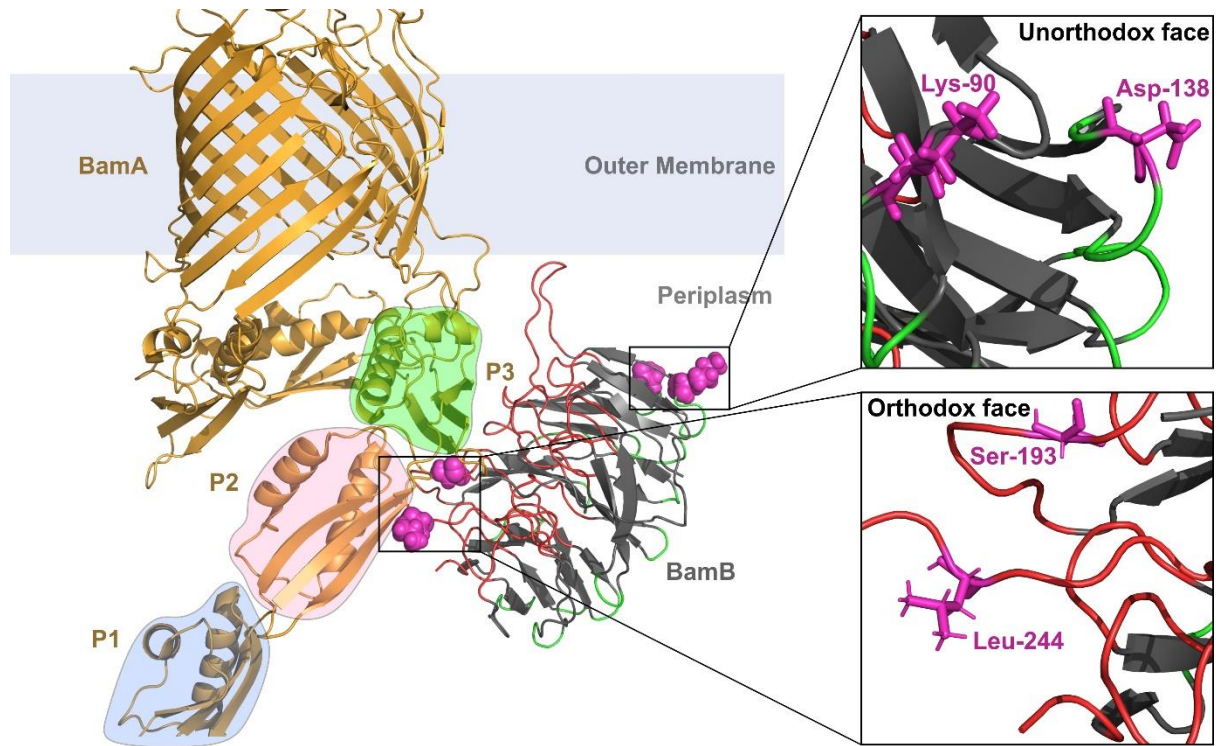
Figure 4.10 Crystal structure of BamA-BamB showing BPA residue incorporation sites on BamB beta-propeller. BPA alleles introduced positions in BamB were represented in purple spheres and a closer look at the orthodox face residues Ser-193, Leu-244 and unorthodox face residues Lys-90, Asp-138 in the right side boxes.
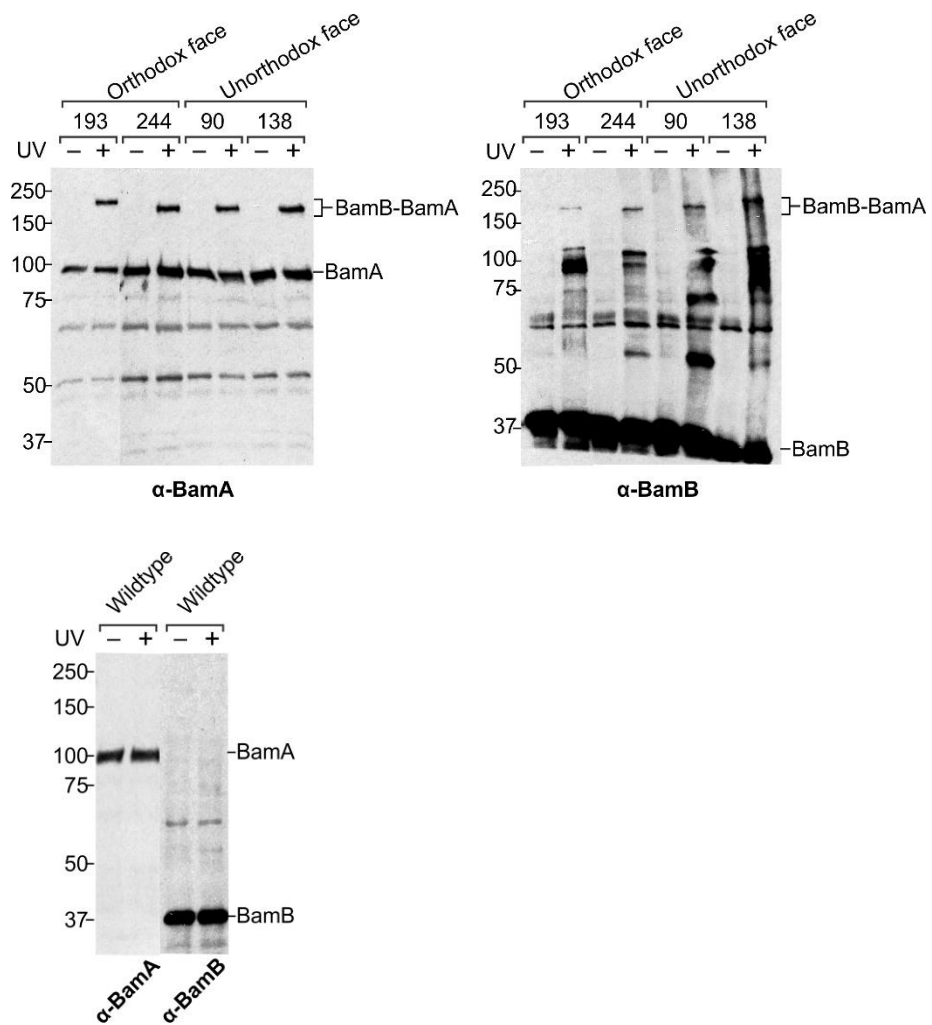
Figure 4.11 BamB *in situ* photocrosslinking using BPA alleles. BamB-BPA photocrosslinking SDS-PAGE/immunoblot detection using antisera raised against BamA and BamB with or without UV exposure (see section 2.2.8). BamB produced repeatable crosslinks to BamA at positions 90, 138, 193, and 244. Extended summary is shown in Figure 4.12.

αBamA

αBamB
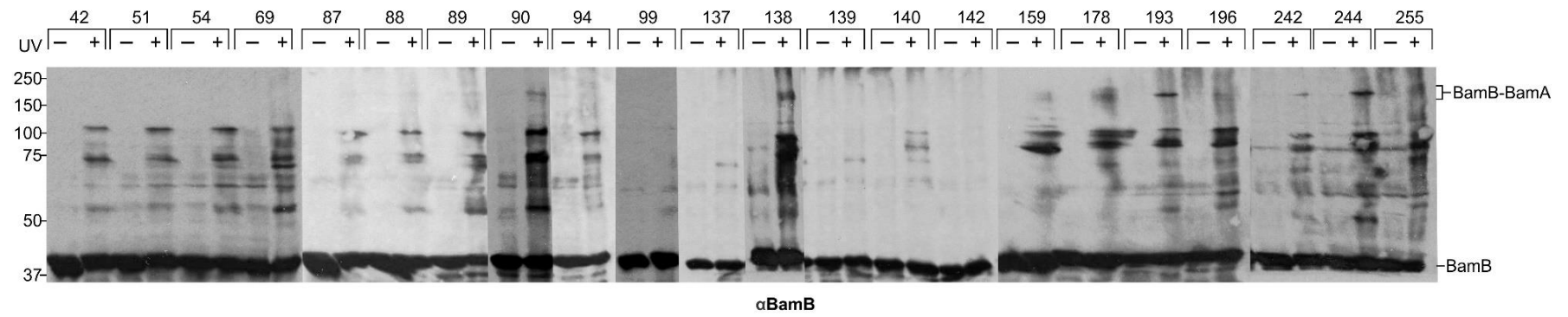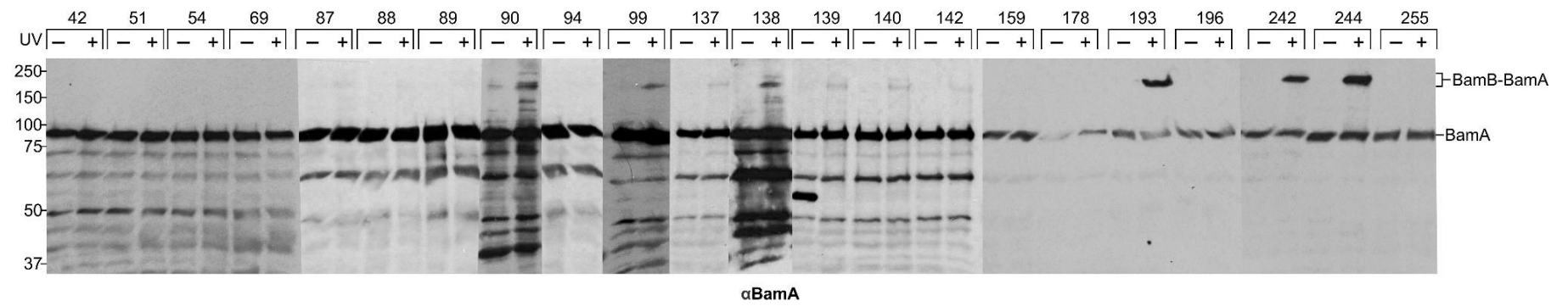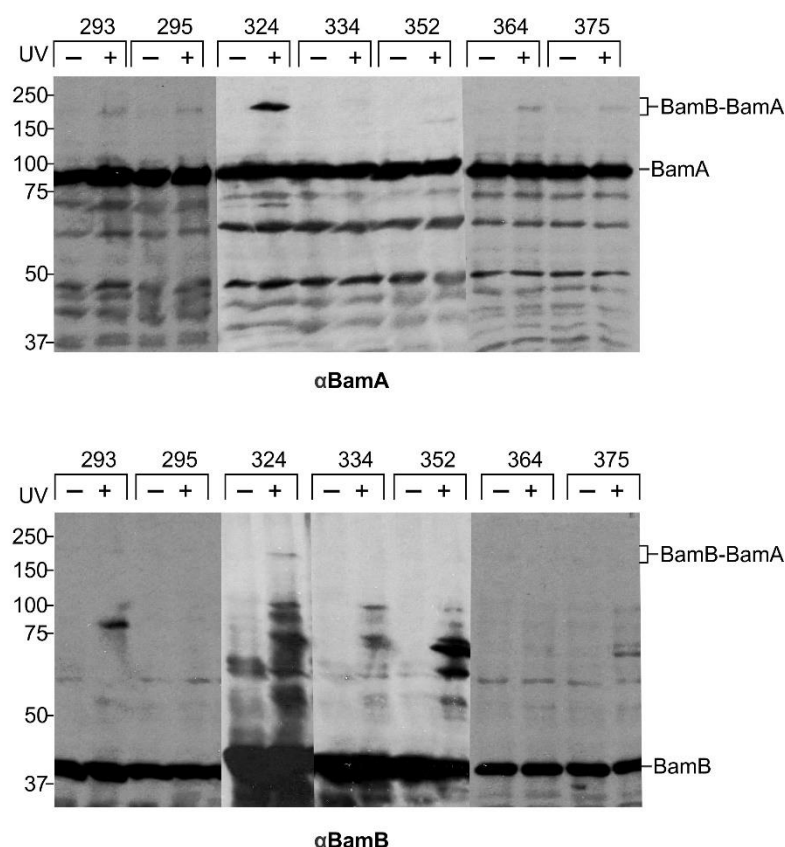
Figure 4.12 Extended summary of BamB *in situ* photocrosslinking using BPA alleles. Amber codons were introduced at 40 positions in the *bamB* sequence, and only 29 were viable for *in situ* photocrosslinking studies in *E. coli* strains.
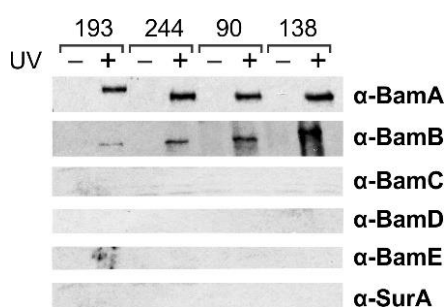
Figure 4.13 Investigating the presence or absence of other subunits of the BAM complex in BamB-BamA crosslink products. Using antibodies raised against BamC, BamD and BamE we determined the presence of other lipoprotein components in the BAM complex in these crosslink products. We also used SurA antibody for the presence of periplasmic chaperons in the crosslink products.

Using BN-PAGE, we were able to show that BamB-BPA variants at positions 90, 138, 193 and 244 had no significant defect in the function of BamB (Figure 4.14). Thus, the presence of the BPA residues does not disturb the integrity of the BAM complex.
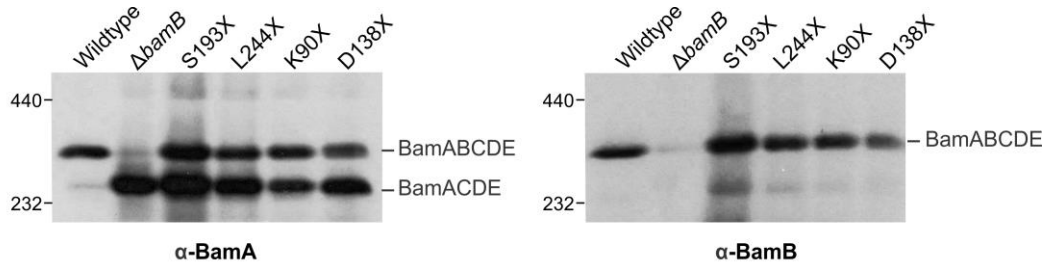
Figure 4.14 BamB BPA allele expression. BN-PAGE/Immunoblot detection using anti-BamA and anti-BamB showing BPA-containing alleles expression in *E. coli*-K12 BW25113; Wildtype, Δ*bamB*::Kan, Δ*bamB*::Kan,pGEM-T-*bamB(S193X)-His6*, Δ*bamB*::Kan,pGEM-T-*bamB(L244X)-His6*, Δ*bamB*::Kan,pGEM-T-*bamB(K90X)-His6* and Δ*bamB*::Kan,pGEM-T-*bamB(D138X)-His6*.
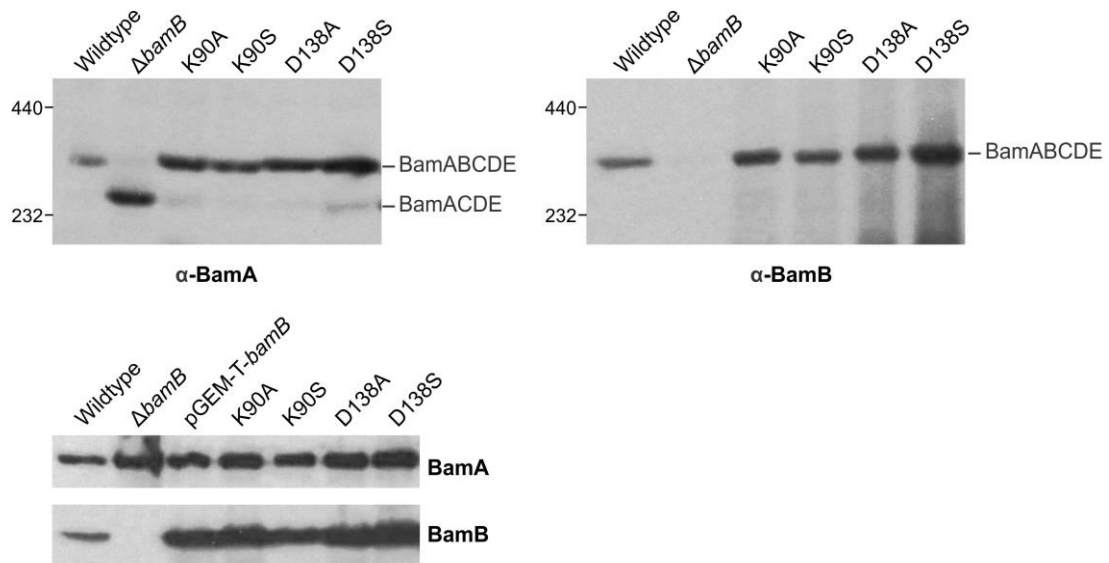
Figure 4.15 BamB site directed mutagenesis expression on unorthodox face residues Lys-90 and Asp-138. Upper panel: BN-PAGE/Immunoblot detection using anti-BamA and anti-BamB showing BamB site directed mutagenesis expression in *E. coli*-K12 BW25113; Wildtype, Δ*bamB*::Kan, Δ*bamB*::Kan,pGEM-T-*bamB(K90A)-His6*,Δ*bamB*::Kan,pGEM-T-*bamB(K90S)-His6*, Δ*bamB*::Kan,pGEM-T-*bamB(D138A)-His6* and Δ*bamB*::Kan,pGEM-T-*bamB(D138S)-His6*. **Lower panel:** SDS-PAGE/Immunoblot detection using anti-BamA and anti-BamB showing BamB site directed mutagenesis expression in *E. coli*-K12 BW25113; Wildtype, Δ*bamB*::Kan, Δ*bamB*::Kan,pGEM-T-*bamB*, Δ*bamB*::Kan,pGEM-T-*bamB(K90A)-His6*,Δ*bamB*::Kan,pGEM-T-*bamB(K90S)-His6*, Δ*bamB*::Kan,pGEM-T-*bamB(D138A)-His6* and Δ*bamB*::Kan,pGEM-T-*bamB(D138S)-His6*.

4.2.5 Dual amber mutation BamB-BPA-photocrosslinking.

Considering a means to demonstrate UV irradiation to produce higher molecular weight crosslinks corresponding to BamA-BamB-BamA heterotrimers (~220 kDa) and/or BamA-BamB-BamB-BamA heterotetramers (~260 kDa).

I performed dual photocrosslinking by introducing two amber mutations into the *bamB* sequence. Combinations for amber dual mutations were selected in a random manner [(90 and 193), (90 and 242), (90 and 244), (138 and 193), (138 and 242) and (138 and 244)]. To test the efficiency of dual amber mutant BPA-photocrosslinking, a positive control was employed. Here, we used two amber mutations located at the orthodox face of BamB (residues 193 and 244).

Dual BPA photocrosslinking experiments, produced the characteristic ~200 kDa bands of the BamA-BamB heterodimer (Figure 4.16). In dual BPA positions (138 and 193) and (138 and 244) a minor amount of crosslink product migrated more slowly than the ~200 kDa BamA-BamB heterodimer. These crosslinks could represent the aforementioned higher order oligomers of BamA and BamB (heterotrimers or heterotetramer). However, these extra higher molecular weight (HMW) bands were not reproducible in subsequent repeat experiments, leaving the question of whether dual-BPA approach can be used in studies such as these. It maybe that these very high molecular weight complexes retained in the stacking gel of the SDS-PAGE and do not readily migrate to the separating gel space for detection by immunoblotting. In order to address this possibility, experiments were repeated using Bis-acrylamide gradient gels (4%-16%) with a softer stacking gel (3%) to perform SDS-PAGE/immunoblotting. Unfortunately, I was not able to detect the very high molecular weight products (Figure 4.17). As a result of the irreproducibility of this data, this line of investigation was abandoned in favour of disulphide cross-linking (section 4.2.6).
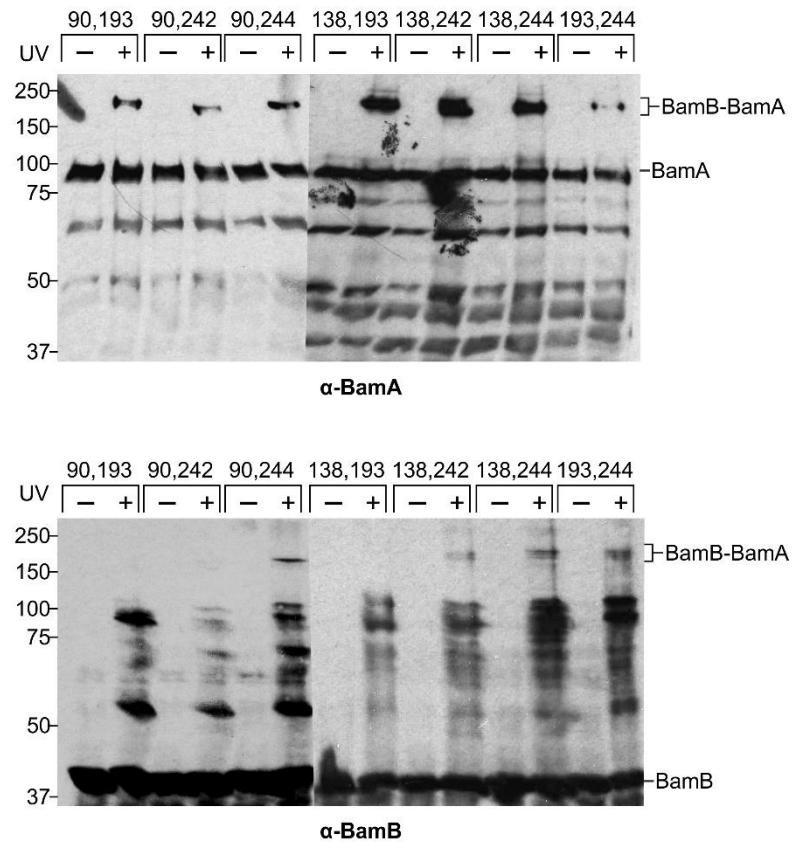
Figure 4.16 BamB *in situ* photocrosslinking using dual BPA alleles. BamB-BPA photocrosslinking SDS-PAGE/immunoblot detection using antisera raised against BamA and BamB with or without UV exposure (see methods). BamB produced BamA-BamB heterodimer crosslinks observed at positions (90 and 244), (138 and 242), (138 and 244) and (193 and 244) [positive control experiment]. BamB also produced non-repeatable HMW bands exceeding the ~200 kDa mark at positions (138 and 242) and (138 and 244).
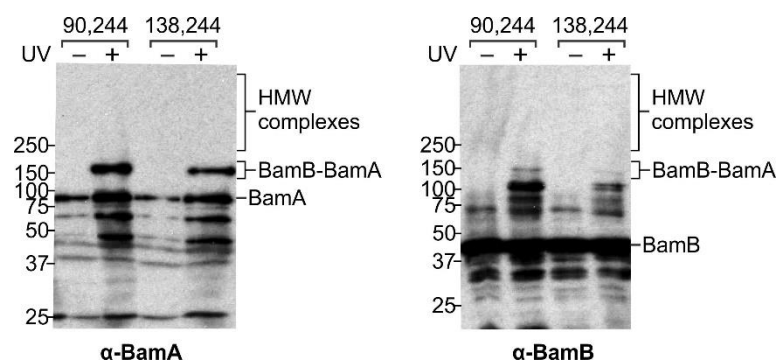
Figure 4.17 Bis-acrylamide gradient gel (4%-16%) for HMW complexes detection. Here, crosslinks exceeding the ~200 kDa BamA-BamB heterodimer mark are considered as HMW complexes which may represent higher order oligomers of BamA and BamB. BamB dual BPA positons (90,244) or (138,244) did not produce any detectable crosslinks correspond to HMW complexes.

4.2.6 Disulphide crosslinking of BamB unorthodox face.

If the neighbouring BAM complex interactions occur exclusively through neighbouring BamB subunits, they should come into contact and possibly form dimers or oligomers. Such BamB-BamB interactions are yet to be observed. Nonetheless, a number of other beta-propellers have been described to form homodimers and hetero-oligomers, and these homotypic interactions are critical for their biological functions (Fath et al., 2007; Yatime et al., 2011; Matthews, 2012).

Sec 13   **Sec 31**   **RACK-1 homodimer**
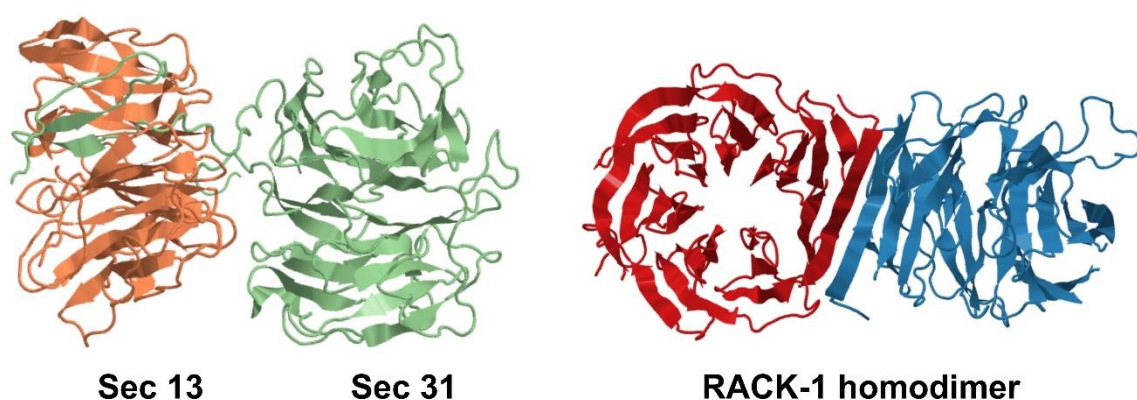
Figure 4.18 Archetypal beta-propellers derived from *Saccharomyces cerevisiae* demonstrating different mechanisms for dimerization. **Left**; N-terminal loop extension of Sec31 interact with Sec13 to form Sec13/31 complex, which is a subunit of COPII assembly complex involved in vesicular trafficking. **Right**; RACK-1 dimer is formed through a mutually shared beta-propeller blade (PDB: 2PM9, 3RFG).

To investigate the propensity for BamB to form homodimers, I utilised site directed mutagenesis to incorporate Cysteine residues at positions 90 or 138 in BamB. Following disulphide crosslinking the proteins were analysed by non-reducing SDS-PAGE and immunoblotting using antisera raised against BamB (see section 2.2.8). Lysates of K90C and D138C showed higher molecular weight BamB species at ~90 kDa and ~120 kDa respectively (Figure 4.20). These corresponding species were hypothesised to represent BamB-BamB interactions. Upon DTT treatment, the higher molecular weight forms were

abolished (Figure 4.20). Based on these observations I speculate that these cysteine mediated disulphide crosslinks represent previously unidentified BamB-BamB interactions. The apparent molecular weights (BamB + BamB = ~80 kDa) of the disulphide crosslinks (90-120 kDa) are not inconsistent with this proposition.
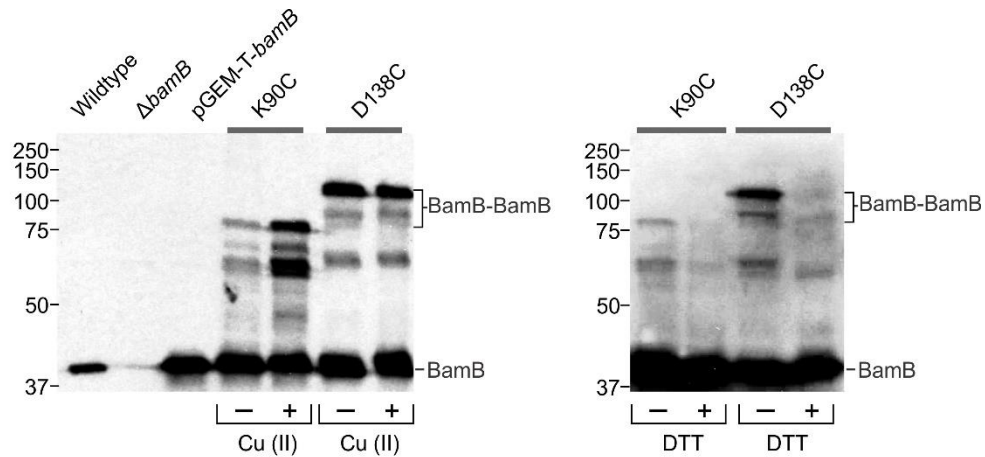
Figure 4.19 BamB-BamB homodimer formation through cysteine mediated disulphide crosslinking. Left panel: BamB disulphide crosslinking and non-reducing SDS-PAGE/immunoblot detection using anti-BamB on whole cell lysates of Wild Type, Δ*bamB*::Kan, Δ*bamB*::Kan,pGEM-T-*bamB-His6*, Δ*bamB*::Kan,pGEM-T-*bamB(K90C)-His6*, Δ*bamB*::Kan,pGEM-T-*bamB(D138C)-His6* with or without Cu(II) enhancement (see methods). **Right panel**: TCA precipitated whole cell lysates of K90C and D138C with or without DTT treatment (see methods). Highest observable molecular weight disulphide crosslinks are indicative of BamB dimers.

To further analyse the constituents of the highest molecular weight disulphide crosslinks, Ni-NTA enrichment was employed (see section 2.2.8). After TCA precipitation of the samples, these BamB-his-tag enriched fractions were separated on a SDS-PAGE. Cross-link products corresponding to ~90 kDa (K90C samples) and ~120 kDa (D138C samples) were then subjected to in-gel digestion for mass spectrometric characterisation of proteins (Figure 4.21). Proteomics analysis revealed a ~40 kDa protein to be the most abundant protein in these ~90 kDa and ~120 kDa crosslink products (Table 4.1). The highest number

of protein spectral matches (PSM) and protein sequence coverage (more than 90%) confirmed the ~40 kDa protein was BamB. Various other proteins ranging from ~70-90 kDa were also detected and were found in both Cysteine crosslinked samples and in the negative control with similar low abundance.
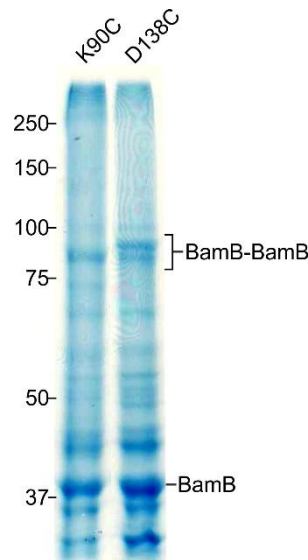
Figure 4.20 Isolation of BamB-BamB homodimers using coomassie blue SDS-PAGE for in-gel digestion for mass spectrometric characterisation of proteins. Ni-NTA His-tag enriched fractions of K90C and D138C were subjected to TCA precipitation (see methods) and separated on 8% Acrylamide SDS-PAGE. Bands were visualised using coomassie blue staining. **Negative control**; A gel fragment of the same region in the adjacent lane, derived from wildtype BamB sample, in which no higher molecular weight cross-linked product was visible was excised and subjected to protein mass spectrometry and used as a negative control (see methods).

Table 4.1 Proteomic analysis of BamB disulphide crosslinks.

Sample	Protein Rank	Protein	Uniprot accession number	Mass (kDa)	[Log Prob]	Best Score	Total Intensity	Number of PSMs	Coverage %
BamB (K90C)	**1**	**BamB**	**P77774**	**41.92**	**1369.98**	**1732.90**	**2313266562.0**	**657**	**94.13**
	2	KatE	P21179	84.16	629.44	1398.7	107637350.7	169	74.9
	3	Pnp	P05055	77.10	523.08	1254.5	78888735	134	72.29
	4	PflB	P09373	85.36	508.37	1084.9	46247079.6	117	76.05
	5	AceF	P06959	66.1	454.49	978.9	46002444.1	101	67.14
BamB (D138C)	**1**	**BamB**	**P77774**	**41.92**	**3111.64**	**1799.00**	**30595297563.5**	**2380**	**98.47**
	2	MgtA	P0ABB8	99.47	832.73	1105.5	496275958.3	250	61.47
	3	FusA	P0A6M8	77.60	766.12	1400.2	278083515.7	171	78.41
	4	AlaS	P00957	96.03	739.08	1240.2	82999251.3	107	68.49
	5	FtsY	P10121	54.51	736.56	1570.8	497978520.4	158	87.93
Negative control	**1**	**KatE**	**P21179**	**84.16**	**1944.07**	**1457.4**	**5103958190.3**	**948**	**88.31**
	2	FusA	P0A6M8	77.60	737.35	1346.9	480143432.5	217	78.27
	3	ClpB	P63284	95.58	730.53	955.7	133518256.8	131	69.78
	4	BamA	P0A940	90.55	719.94	1354.5	223370310.9	148	75.56
	5	DnaK	P0A6Y8	69.11	711.55	1625.4	190318348.4	145	76.8

[Log Prob]: Absolute value of the Log base 10 of the protein p-value (p is the probability that the observed match is a random event). **Best Score** - Largest Byonic score of a Protein Spectral Match (PSM) assigned to the protein. **Total Intensity** – Sum of all fragment peak intensities over all MS/MS spectra. **Number of PSMs** - Total number of PSMs including duplicate PSMs. **Coverage %** – Percent of the protein sequence covered by PSMs.

4.3 Discussion.

The evidence gathered from *in situ* photocrosslinking experiments helped us to expand the interactome of BamB lipoprotein subunit in the BAM complex. My results demonstrate how the unorthodox face of BamB participates in non-canonical interactions with neighbouring BAM complex components, both BamA and BamB. Cysteine mediated disulphide crosslinking studies in BamB provides additional confirmation to the protein interactions occurring at the unorthodox face through the formation of BamB-BamB homotypic interactions. Together these findings provide a mechanistic overview for BamB-mediated inter-BAM complex interactions and consequently, illustrates the formation of protein assembly precincts in the outer membrane. It cannot be ruled out that interactions mediated through the unorthodox face of BamB might also assists interactions with substrate OMPs at initial and/or later stages of the protein assembly (Figure 5A). However, this remains as yet simple speculation.

The crosslinking data taken together with *d*STORM data (Chapter 3) provide mechanistic understanding with BamB mediating neighbouring BAM complex interactions, consequently illuminating further the idea of protein assembly precincts in the outer membrane of *E. coli*. These ideas are discussed in the final Chapter of this thesis.

Top view

Photocrosslinkable residues

—— BamB orthodox face loops

—— BamB unorthodox face loops

······ BAM:BAM interaction interface
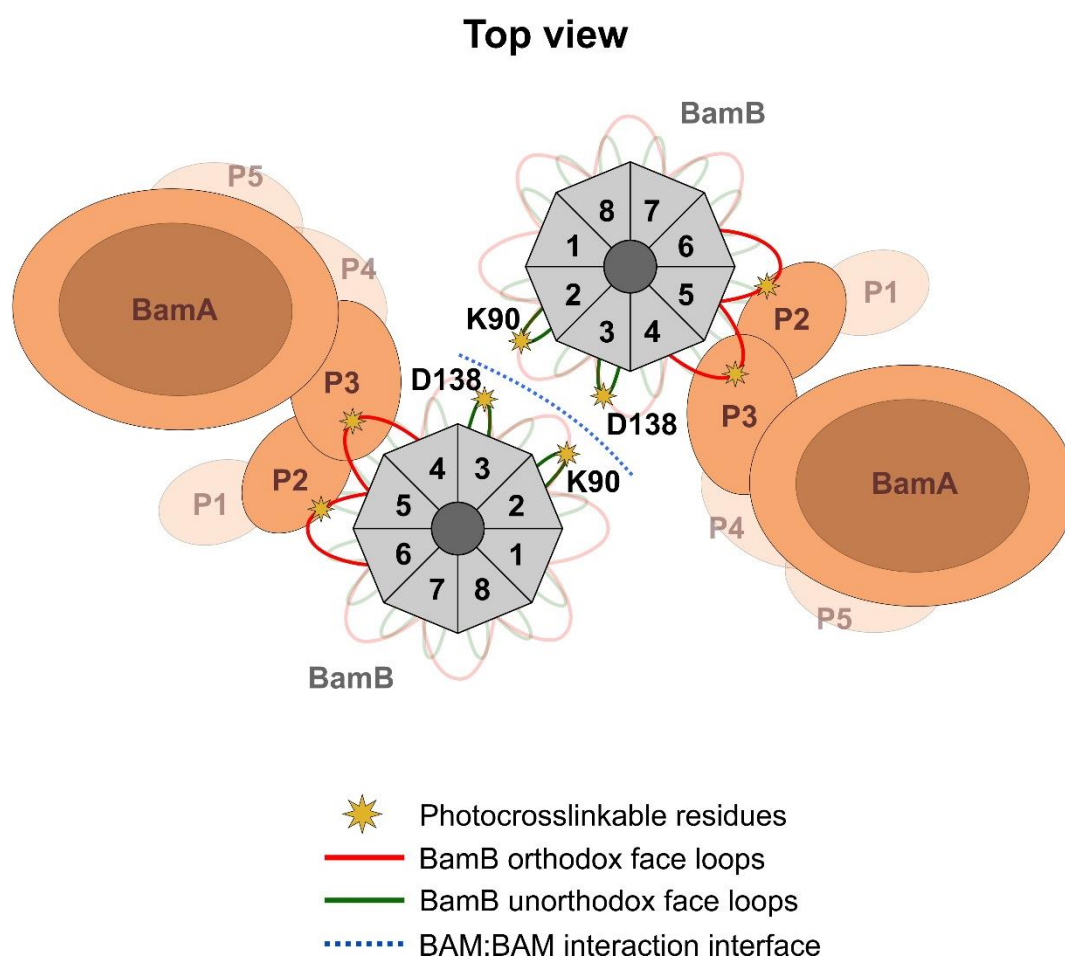
Figure 4.21 A novel BAM:BAM interaction interface formed through unorthodox face of BamB. This interaction interface can serve as a binding domain for neighbouring BAM complex subunits and BAM complex substrates.

Chapter 5: BAM clusters as protein assembly precincts; a small glimpse into the bigger picture.

Based on all of the data presented in this thesis, I am proposing a BAM:BAM interaction model that provides a small glimpse into the bigger picture of the mechanism employed by the BAM complex to catalyse assembly and insertion of newly folded OMPs. The present findings have important implications in solving the long lasting question of what drives the integral proteins assembly in the first place, especially in the absence of any chemical energy source such as ATP. The current paradigm of membrane destabilisation via BamA is thought to provide a means to lower the energy barrier for insertion of nascent outer membrane proteins (Fleming, 2015; Noinaj et al., 2017).

I suggest that protein assembly precincts formed for several BAM complexes enables a more pronounced membrane destabilisation, providing sufficient entropy to drive protein integration into the membrane. This can be potentially useful in assembling a number of porins that function as multimers at the outer membrane, such as trimers of OmpC, OmpF and LamB (Figure 5.1).
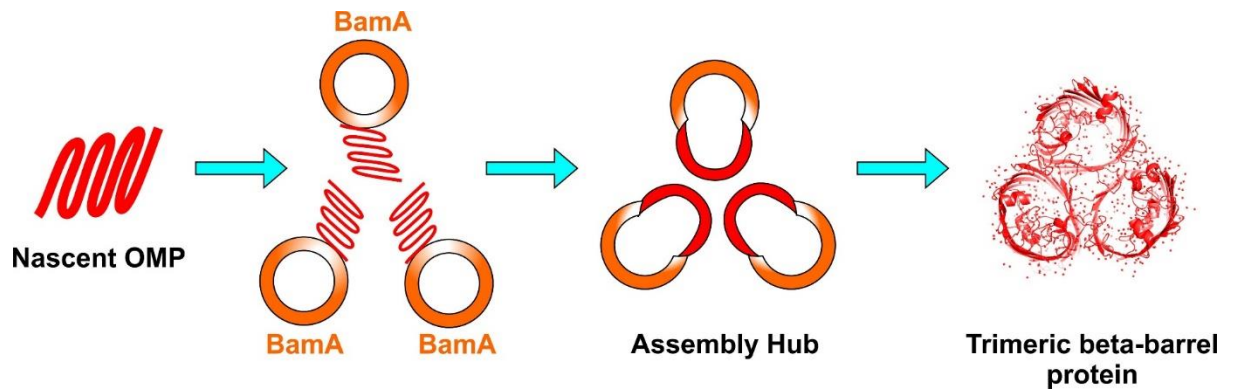
Figure 5.1 BAM complex assembly precincts or assembly hub formation. Flow diagram Left to Right; (1) the incoming nascent OMP. (2) BamA beta-barrel serves as a template to fold bet-barrel proteins via the beta-augmentation mechanism. (3) Several BAM complexes coming together and forms assembly hubs where several beta-barrel proteins are being folded and assembled into the outer membrane simultaneously. (4) Formation of multimeric outer membrane proteins at the outer membrane.

Previous studies which have examined the lateral mobility of porins and other monomeric beta-barrel proteins (such as Antigen 43) suggests their existence in large rafts of proteins in the outer membrane as a result of non-specific protein-protein interactions. However, the question remains whether the same notion can be applied to explain the formation of BAM complex assembly precincts. These highly organised assembly hubs occupying several BAM complexes visualised through nanoscopy would seem to have much more specific protein-protein interactions, rather than promiscuous in nature. Our cluster analysis calculations showed these assembly hubs sits at ~200 nm apart from each other, in wildtype cells and in mutants (Δ*bamB* or Δ*bamE*), and this does not change even in the absence of the load of protein cargo they are handling (mid-log phase or under reduced protein synthesis conditions).

The biochemical evidence gathered through *in situ* crosslinking experiments, we were able to provide more mechanistic overview on the mediator role played by BamB subunit promoting BAM:BAM interactions within BAM clusters. The different rates at which the

assembly takes place and the specificity of BamA towards the substrates can be important factors in determining the nature of these interactions, as could the conformational changes that would occur within the BAM complex to minimise steric effects occurring between neighbouring BAM complexes during the formation of assembly precincts.

My findings provide a missing piece of the mechanistic puzzle of the BAM complex in regards to how it catalyses the assembly and insertion of substrate OMPs by forming assembly precincts in the outer membrane. Additionally, the surface localization studies carried out on *E. coli* BAM complex provide groundwork to spatially characterise similar supramolecular assembly complexes in other gram-negative bacteria.

References

Abràmoff, M.D., Magalhães, P.J., and Ram, S.J. (2004). Image processing with ImageJ. *Biophotonics international* 11(7)**,** 36-42.

Albrecht, R., and Zeth, K. (2011). Structural basis of outer membrane protein biogenesis in bacteria. *Journal of Biological Chemistry* 286(31)**,** 27792-27803.

Ames, P., and Parkinson, J.S. (2006). Conformational suppression of inter-receptor signaling defects. *Proceedings of the National Academy of Sciences* 103(24)**,** 9292-9297.

Baba, T., Ara, T., Hasegawa, M., Takai, Y., Okumura, Y., Baba, M., et al. (2006). Construction of Escherichia coli K-12 in-frame, single-gene knockout mutants: the Keio collection. *Molecular Systems Biology* 2**,** 2006.0008-2006.0008. doi: 10.1038/msb4100050.

Baddeley, A., and Turner, R. (2005). spatstat: An R Package for Analyzing Spatial Point Patterns. *2005* 12(6)**,** 42. doi: 10.18637/jss.v012.i06.

Bakelar, J., Buchanan, S.K., and Noinaj, N. (2016). The structure of the beta-barrel assembly machinery complex. *Science* 351(6269)**,** 180-186. doi: 10.1126/science.aad3460.

Bakshi, S., Siryaporn, A., Goulian, M., and Weisshaar, J.C. (2012). Superresolution imaging of ribosomes and RNA polymerase in live Escherichia coli cells. *Molecular microbiology* 85(1)**,** 21-38.

Barlag, B., Beutel, O., Janning, D., Czarniak, F., Richter, C.P., Kommnick, C., et al. (2016). Single molecule super-resolution imaging of proteins in living Salmonella enterica using self-labelling enzymes. *Scientific reports* 6.

Begg, K., and Donachie, W. (1973). Topography of outer membrane growth in E. coli. *Nature* 245(141)**,** 38-39.

Bennion, D., Charlson, E.S., Coon, E., and Misra, R. (2010). Dissection of β-barrel outer membrane protein assembly pathways through characterizing BamA POTRA 1 mutants of Escherichia coli. *Molecular Microbiology* 77(5)**,** 1153-1171.

Berg, M., Michalowski, A., Palzer, S., Rupp, S., and Sohn, K. (2014). An In Vivo Photo-Cross-Linking Approach Reveals a Homodimerization Domain of Aha1 in S. cerevisiae. *PLoS ONE* 9(3)**,** e89436-e89436.

Bergal, H.T., Hopkins, A.H., Metzner, S.I., and Sousa, M.C. (2016). The Structure of a BamA-BamD Fusion Illuminates the Architecture of the beta-Barrel Assembly Machine Core. *Structure* 24(2)**,** 243-251. doi: 10.1016/j.str.2015.10.030.

Betzig, E., Patterson, G.H., Sougrat, R., Lindwasser, O.W., Olenych, S., Bonifacino, J.S., et al. (2006). Imaging intracellular fluorescent proteins at nanometer resolution. *Science* 313(5793)**,** 1642-1645. doi: 10.1126/science.1127344.

Bi, E., and Lutkenhaus, J. (1991). FtsZ ring structure associated with division in Escherichia coli. *Nature* 354(6349)**,** 161.

Binenbaum, Z., Parola, A.H., Zaritsky, A., and Fishov, I. (1999). Transcription-and translation-dependent changes in membrane dynamics in bacteria: testing the transertion model for domain formation. *Molecular microbiology* 32(6)**,** 1173-1182.

Cameron, E.A., Maynard, M.A., Smith, C.J., Smith, T.J., Koropatkin, N.M., and Martens, E.C. (2012). Multidomain carbohydrate-binding proteins involved in Bacteroides thetaiotaomicron starch metabolism. *Journal of Biological Chemistry* 287(41)**,** 34614-34625.

Charles, M., Pérez, M., Kobil, J.H., and Goldberg, M.B. (2001). Polar targeting of Shigella virulence factor IcsA in Enterobacteriacae and Vibrio. *Proceedings of the National Academy of Sciences* 98(17)**,** 9871-9876.

Charlson, E.S., Werner, J.N., and Misra, R. (2006). Differential effects of yfgL mutation on Escherichia coli outer membrane proteins and lipopolysaccharide. *Journal of bacteriology* 188(20)**,** 7186-7194.

Chatterjee, S., and Rothenberg, E. (2012). Interaction of bacteriophage l with its *E. coli* receptor, LamB. *Viruses* 4(11)**,** 3162-3178. doi: 10.3390/v4113162.

Chen, Z., Zhan, L.-H., Hou, H.-F., Gao, Z.-Q., Xu, J.-H., Dong, C., et al. (2016). Structural basis for the interaction of BamB with the POTRA3–4 domains of BamA. *Acta Crystallographica Section D: Structural Biology* 72(2)**,** 236-244.

Childers, B.M., and Klose, K.E. (2007). Regulation of virulence in Vibrio cholerae: the ToxR regulon.

Chin, J.W., Santoro, S.W., Martin, A.B., King, D.S., Wang, L., and Schultz, P.G. (2002). Addition of p-Azido-l-phenylalanine to the Genetic Code of Escherichia c oli. *Journal of the American Chemical Society* 124(31)**,** 9026-9027.

Christensen, H., Garton, N.J., Horobin, R.W., Minnikin, D.E., and Barer, M.R. (1999). Lipid domains of mycobacteria studied with fluorescent molecular probes. *Molecular microbiology* 31(5)**,** 1561-1572.

Clancy, B., and Cauller, L. (1998). Reduction of background autofluorescence in brain sections following immersion in sodium borohydride. *Journal of neuroscience methods* 83(2)**,** 97-102.

Clements, A., Bursac, D., Gatsos, X., Perry, A.J., Civciristov, S., Celik, N., et al. (2009). The reducible complexity of a mitochondrial molecular machine. *Proceedings of the National Academy of Sciences* 106(37)**,** 15791-15795.

Dalbey, R.E., and Kuhn, A. (2012). Protein traffic in Gram-negative bacteria–how exported and secreted proteins find their way. *FEMS microbiology reviews* 36(6)**,** 1023-1045.

Danese, P.N., Pratt, L.A., Dove, S.L., and Kolter, R. (2000). The outer membrane protein, Antigen 43, mediates cell-to-cell interactions within *Escherichia coli* biofilms. *Molecular microbiology* 37(2)**,** 424-432. doi: 10.1046/j.1365-2958.2000.02008.x.

de Cock, H., and Tommassen, J. (1996). Lipopolysaccharides and divalent cations are involved in the formation of an assembly-competent intermediate of outer-membrane protein PhoE of E. coli. *The EMBO journal* 15(20)**,** 5567.

De Geyter, J., Tsirigotaki, A., Orfanoudaki, G., Zorzini, V., Economou, A., and Karamanou, S. (2016). Protein folding in the cell envelope of *Escherichia coli*. *Nature microbiology* 1**,** 16107. doi: 10.1038/nmicrobiol.2016.107.

De Pedro, M.A., Schwarz, H., and Koch, A.L. (2003). Patchiness of murein insertion into the sidewall of *Escherichia coli*. *Microbiology* 149(7)**,** 1753-1761. doi: 10.1099/mic.0.26125-0.

Dempsey, G.T., Vaughan, J.C., Chen, K.H., Bates, M., and Zhuang, X. (2011). Evaluation of fluorophores for optimal performance in localization-based super-resolution imaging. *Nature methods* 8(12)**,** 1027-1036.

Donald, J.E., Kulp, D.W., and DeGrado, W.F. (2011). Salt Bridges: Geometrically Specific, Designable Interactions. *Proteins* 79(3)**,** 898-915. doi: 10.1002/prot.22927.

Dong, C., Hou, H.F., Yang, X., Shen, Y.Q., and Dong, Y.H. (2012). Structure of Escherichia coli BamD and its functional implications in outer membrane protein assembly. *Acta Crystallogr D Biol Crystallogr* 68(Pt 2)**,** 95-101. doi: 10.1107/s0907444911051031.

Driks, A., and Losick, R. (1991). Compartmentalized expression of a gene under the control of sporulation transcription factor sigma E in Bacillus subtilis. *Proceedings of the National Academy of Sciences* 88(22)**,** 9934-9938.

Dunstan, R.A., Hay, I.D., Wilksch, J.J., Schittenhelm, R.B., Purcell, A.W., Clark, J., et al. (2015). Assembly of the secretion pores GspD, Wza and CsgG into bacterial outer membranes does not require the Omp85 proteins BamA or TamA. *Molecular microbiology* 97(4)**,** 616-629.

Endesfelder, U., Malkusch, S., Flottmann, B., Mondry, J., Liguzinski, P., Verveer, P.J., et al. (2011). Chemically induced photoswitching of fluorescent probes—a general concept for super-resolution microscopy. *Molecules* 16(4)**,** 3106-3118.

Endo, T., Kawano, S., and Yamano, K. (2011). BamE structure: the assembly of β-barrel proteins in the outer membranes of bacteria and mitochondria. *EMBO reports* 12(2)**,** 94-95.

Fardini, Y., Chettab, K., Grépinet, O., Rochereau, S., Trotereau, J., Harvey, P., et al. (2007). The YfgL lipoprotein is essential for type III secretion system expression and virulence of Salmonella enterica serovar Enteritidis. *Infection and immunity* 75(1)**,** 358-370.

Farrell, I.S., Toroney, R., Hazen, J.L., Mehl, R.A., and Chin, J.W. (2005). Photo-cross-linking interacting proteins with a genetically encoded benzophenone. *Nature methods* 2(5)**,** 377-384.

Fath, S., Mancias, J.D., Bi, X., and Goldberg, J. (2007). Structure and organization of coat proteins in the COPII cage. *Cell* 129(7)**,** 1325-1336.

Fishov, I., and Norris, V. (2012). Membrane heterogeneity created by transertion is a global regulator in bacteria. *Current opinion in microbiology* 15(6)**,** 724-730.

Fishov, I., and Woldringh, C.L. (1999). Visualization of membrane domains in Escherichia coli. *Molecular microbiology* 32(6)**,** 1166-1172.

Fleming, K.G. (2015). A combined kinetic push and thermodynamic pull as driving forces for outer membrane protein sorting and folding in bacteria. *Phil. Trans. R. Soc. B* 370(1679)**,** 20150026.

Gahlmann, A., and Moerner, W. (2014). Exploring bacterial cell biology with single-molecule tracking and super-resolution imaging. *Nature Reviews Microbiology* 12(1)**,** 9-22.

Gatzeva-Topalova, P.Z., Walton, T.A., and Sousa, M.C. (2008). Crystal structure of YaeT: conformational flexibility and substrate recognition. *Structure* 16(12)**,** 1873-1881.

Getis, A., and Franklin, J. (1987). Second-Order Neighborhood Analysis of Mapped Point Patterns. *Ecology* 68(3)**,** 473-477. doi: 10.2307/1938452.

Ghosh, A.S., and Young, K.D. (2005). Helical disposition of proteins and lipopolysaccharide in the outer membrane of Escherichia coli. *Journal of bacteriology* 187(6)**,** 1913-1922.

Gibbs, K.A., Isaac, D.D., Xu, J., Hendrix, R.W., Silhavy, T.J., and Theriot, J.A. (2004). Complex spatial distribution and dynamics of an abundant *Escherichia coli* outer membrane protein, LamB. *Molecular microbiology* 53(6)**,** 1771-1783. doi: 10.1111/j.1365-2958.2004.04242.x.

Gu, Y., Li, H., Dong, H., Zeng, Y., Zhang, Z., Paterson, N.G., et al. (2016). Structural basis of outer membrane protein insertion by the BAM complex. *Nature* 531(7592)**,** 64-69.

Gustafsson, M.G. (2000). Surpassing the lateral resolution limit by a factor of two using structured illumination microscopy. *Journal of microscopy* 198(2)**,** 82-87.

Gustafsson, M.G. (2005). Nonlinear structured-illumination microscopy: wide-field fluorescence imaging with theoretically unlimited resolution. *Proceedings of the*

National Academy of Sciences of the United States of America 102(37)**,** 13081-13086. doi: 10.1073/pnas.0406877102.

Haas, B.L., Matson, J.S., DiRita, V.J., and Biteen, J.S. (2015). Single-molecule tracking in live Vibrio cholerae reveals that ToxR recruits the membrane-bound virulence regulator TcpP to the toxT promoter. *Molecular microbiology* 96(1)**,** 4-13.

Hagan, C.L., and Kahne, D. (2011). The reconstituted Escherichia coli Bam complex catalyzes multiple rounds of β-barrel assembly. *Biochemistry* 50(35)**,** 7444-7446.

Hagan, C.L., Kim, S., and Kahne, D. (2010a). Reconstitution of outer membrane protein assembly from purified components. *Science* 328(5980)**,** 890-892.

Hagan, C.L., Kim, S., and Kahne, D. (2010b). Reconstitution of outer membrane protein assembly from purified components. *Science* 328(5980)**,** 890-892. doi: 10.1126/science.1188919.

Hagan, C.L., Silhavy, T.J., and Kahne, D. (2011). β-Barrel membrane protein assembly by the Bam complex. *Annual review of biochemistry* 80**,** 189-210.

Han, L., Zheng, J., Wang, Y., Yang, X., Liu, Y., Sun, C., et al. (2016). Structure of the BAM complex and its implications for biogenesis of outer-membrane proteins. *Nature structural & molecular biology* 23(3)**,** 192-196.

Hancock, R. (1987). Role of porins in outer membrane permeability. *Journal of bacteriology* 169(3)**,** 929.

Hancock, R., and Reeves, P. (1976). Lipopolysaccharide-deficient, bacteriophage-resistant mutants of *Escherichia coli* K-12. *Journal of bacteriology* 127(1)**,** 98-108.

Heilemann, M., Dedecker, P., Hofkens, J., and Sauer, M. (2009a). Photoswitches: Key molecules for subdiffraction-resolution fluorescence imaging and molecular quantification. *Laser & Photonics Reviews* 3(1-2)**,** 180-202. doi: 10.1002/lpor.200810043.

Heilemann, M., Margeat, E., Kasper, R., Sauer, M., and Tinnefeld, P. (2005). Carbocyanine dyes as efficient reversible single-molecule optical switch. *Journal of the American Chemical Society* 127(11)**,** 3801-3806.

Heilemann, M., van de Linde, S., Mukherjee, A., and Sauer, M. (2009b). Super-resolution imaging with small organic fluorophores. *Angewandte Chemie International Edition* 48(37)**,** 6903-6908.

Hell, S.W. (2007). Far-field optical nanoscopy. *Science* 316(5828)**,** 1153-1158. doi: 10.1126/science.1137395.

Hell, S.W. (2009). Microscopy and its focal switch. *Nature methods* 6(1)**,** 24-32. doi: 10.1038/nmeth.1291.

Hell, S.W., and Wichmann, J. (1994). Breaking the diffraction resolution limit by stimulated emission: stimulated-emission-depletion fluorescence microscopy. *Optics letters* 19(11)**,** 780-782. doi: 10.1364/OL.19.000780.

Henderson, I.R., Navarro-Garcia, F., Desvaux, M., Fernandez, R.C., and Ala'Aldeen, D. (2004). Type V protein secretion pathway: the autotransporter story. *Microbiology and molecular biology reviews* 68(4)**,** 692-744.

Heras, B., Totsika, M., Peters, K.M., Paxman, J.J., Gee, C.L., Jarrott, R.J., et al. (2014). The antigen 43 structure reveals a molecular Velcro-like mechanism of autotransporter-mediated bacterial clumping. *Proceedings of the National Academy of Sciences* 111(1)**,** 457-462.

Heuck, A., Schleiffer, A., and Clausen, T. (2011). Augmenting beta-augmentation: structural basis of how BamB binds BamA and may support folding of outer membrane proteins. *J Mol Biol* 406(5)**,** 659-666. doi: 10.1016/j.jmb.2011.01.002.

Hofmann, M., Eggeling, C., Jakobs, S., and Hell, S.W. (2005). Breaking the diffraction barrier in fluorescence microscopy at low light intensities by using reversibly

photoswitchable proteins. *Proceedings of the National Academy of Sciences of the United States of America* 102(49)**,** 17565-17569. doi: 10.1073/pnas.0506010102.

Hsieh, P.-F., Hsu, C.-R., Chen, C.-T., Lin, T.-L., and Wang, J.-T. (2016). The Klebsiella pneumoniae YfgL (BamB) lipoprotein contributes to outer membrane protein biogenesis, type-1 fimbriae expression, anti-phagocytosis, and in vivo virulence. *Virulence* 7(5)**,** 587-601.

Huang, B., Babcock, H., and Zhuang, X. (2010). Breaking the diffraction barrier: super-resolution imaging of cells. *Cell* 143(7)**,** 1047-1058. doi: 10.1016/j.cell.2010.12.002.

Huang, B., Bates, M., and Zhuang, X. (2009). Super-resolution fluorescence microscopy. *Annual review of biochemistry* 78**,** 993-1016. doi: 10.1146/annurev.biochem.77.061906.092014.

Ieva, R., and Bernstein, H.D. (2009). Interaction of an autotransporter passenger domain with BamA during its translocation across the bacterial outer membrane. *Proceedings of the National Academy of Sciences* 106(45)**,** 19120-19125.

Ieva, R., Tian, P., Peterson, J.H., and Bernstein, H.D. (2011). Sequential and spatially restricted interactions of assembly factors with an autotransporter β domain. *Proceedings of the National Academy of Sciences* 108(31)**,** E383-E391.

Ihaka, R., and Gentleman, R. (1996). R: A Language for Data Analysis and Graphics. *Journal of Computational and Graphical Statistics* 5(3)**,** 299-314. doi: 10.1080/10618600.1996.10474713.

Jain, S., van Ulsen, P., Benz, I., Schmidt, M.A., Fernandez, R., Tommassen, J., et al. (2006). Polar localization of the autotransporter family of large bacterial virulence proteins. *Journal of bacteriology* 188(13)**,** 4841-4850.

Janakiraman, A., and Goldberg, M.B. (2004). Evidence for polar positional information independent of cell division and nucleoid occlusion. *Proceedings of the National Academy of Sciences of the United States of America* 101(3)**,** 835-840. doi: 10.1073/pnas.0305747101.

Jansen, K.B., Baker, S.L., and Sousa, M.C. (2012). Crystal structure of BamB from Pseudomonas aeruginosa and functional evaluation of its conserved structural features. *PloS one* 7(11)**,** e49749.

Jansen, K.B., Baker, S.L., and Sousa, M.C. (2015). Crystal structure of BamB bound to a periplasmic domain fragment of BamA, the central component of the β-barrel assembly machine. *Journal of Biological Chemistry* 290(4)**,** 2126-2136.

Juette, M.F., Gould, T.J., Lessard, M.D., Mlodzianoski, M.J., Nagpure, B.S., Bennett, B.T., et al. (2008). Three-dimensional sub-100 nm resolution fluorescence microscopy of thick samples. *Nat Methods* 5(6)**,** 527-529. doi: 10.1038/nmeth.1211.

Kamiyama, D., and Huang, B. (2012). Development in the STORM. *Developmental cell* 23(6)**,** 1103-1110. doi: 10.1016/j.devcel.2012.10.003.

Karunatilaka, K.S., Cameron, E.A., Martens, E.C., Koropatkin, N.M., and Biteen, J.S. (2014). Superresolution imaging captures carbohydrate utilization dynamics in human gut symbionts. *MBio* 5(6)**,** e02172-02114.

Kato, N., Ohta, M., Kido, N., Ito, H., Naito, S., Hasegawa, T., et al. (1990). Crystallization of R-form lipopolysaccharides from *Salmonella minnesota* and *Escherichia coli*. *Journal of bacteriology* 172(3)**,** 1516-1528. doi: 10.1128/jb.172.3.1516-1528.1990.

Kato, N., Sugiyama, T., Naito, S., Arakawa, Y., Ito, H., Kido, N., et al. (2000). Molecular structure of bacterial endotoxin (*Escherichia coli* Re lipopolysaccharide): implications for formation of a novel heterogeneous lattice structure. *Molecular microbiology* 36(4)**,** 796-805. doi: 10.1046/j.1365-2958.2000.01893.x.

Kim, K.H., Aulakh, S., and Paetzel, M. (2011). Crystal structure of beta-barrel assembly machinery BamCD protein complex. *J Biol Chem* 286(45)**,** 39116-39121. doi: 10.1074/jbc.M111.298166.

Kim, K.H., Aulakh, S., and Paetzel, M. (2012). The bacterial outer membrane β-barrel assembly machinery. *Protein Science* 21(6)**,** 751-768.

Kim, K.H., and Paetzel, M. (2011). Crystal structure of Escherichia coli BamB, a lipoprotein component of the beta-barrel assembly machinery complex. *J Mol Biol* 406(5)**,** 667-678. doi: 10.1016/j.jmb.2010.12.020.

Kim, S., Malinverni, J.C., Sliz, P., Silhavy, T.J., Harrison, S.C., and Kahne, D. (2007). Structure and function of an essential component of the outer membrane protein assembly machine. *Science* 317(5840)**,** 961-964.

Kjærgaard, K., Schembri, M.A., Hasman, H., and Klemm, P. (2000). Antigen 43 from *Escherichia coli* induces inter-and intraspecies cell aggregation and changes in colony morphology of *Pseudomonas fluorescens. Journal of bacteriology* 182(17)**,** 4789-4796. doi: 10.1128/JB.182.17.4789-4796.2000.

Klar, T.A., and Hell, S.W. (1999). Subdiffraction resolution in far-field fluorescence microscopy. *Optics letters* 24(14)**,** 954-956. doi: 10.1364/OL.24.000954.

Klemm, P., Hjerrild, L., Gjermansen, M., and Schembri, M.A. (2004). Structure-function analysis of the self-recognizing antigen 43 autotransporter protein from Escherichia coli. *Molecular microbiology* 51(1)**,** 283-296.

Knowles, T.J., Browning, D.F., Jeeves, M., Maderbocus, R., Rajesh, S., Sridhar, P., et al. (2011). Structure and function of BamE within the outer membrane and the beta-barrel assembly machine. *EMBO Rep* 12(2)**,** 123-128. doi: 10.1038/embor.2010.202.

Knowles, T.J., Jeeves, M., Bobat, S., Dancea, F., McClelland, D., Palmer, T., et al. (2008). Fold and function of polypeptide transport-associated domains responsible for delivering unfolded proteins to membranes. *Molecular microbiology* 68(5)**,** 1216-1227.

Koch, A.L. (1996). What size should a bacterium be? A question of scale. *Annual Reviews in Microbiology* 50(1)**,** 317-348. doi: 10.1146/annurev.micro.50.1.317.

Leksa, N.C., and Schwartz, T.U. (2010). Membrane-coating lattice scaffolds in the nuclear pore and vesicle coats: commonalities, differences, challenges. *Nucleus* 1(4)**,** 314-318. doi: 10.4161/nucl.1.4.11798.

Lewis, C., Skovierova, H., Rowley, G., Rezuchova, B., Homerova, D., Stevenson, A., et al. (2008). Small outer-membrane lipoprotein, SmpA, is regulated by σE and has a role in cell envelope integrity and virulence of Salmonella enterica serovar Typhimurium. *Microbiology* 154(3)**,** 979-988.

Li, B., Hu, Z., and Elkins, C.A. (2014). Detection of Live *Escherichia coli* O157:H7 Cells by PMA-qPCR. *Journal of Visualized Experiments : JoVE* (84)**,** 50967. doi: 10.3791/50967.

Lieberman, J.A., Frost, N.A., Hoppert, M., Fernandes, P.J., Vogt, S.L., Raivio, T.L., et al. (2012). Outer membrane targeting, ultrastructure, and single molecule localization of the enteropathogenic Escherichia coli type IV pilus secretin BfpB. *Journal of bacteriology* 194(7)**,** 1646-1658.

Lindner, A.B., Madden, R., Demarez, A., Stewart, E.J., and Taddei, F. (2008). Asymmetric segregation of protein aggregates is associated with cellular aging and rejuvenation. *Proceedings of the National Academy of Sciences* 105(8)**,** 3076-3081. doi: 10.1073/pnas.0708931105.

Lippincott-Schwartz, J., and Patterson, G.H. (2009). Photoactivatable fluorescent proteins for diffraction-limited and super-resolution imaging. *Trends in cell biology* 19(11)**,** 555-565. doi: 10.1016/j.tcb.2009.09.003.

Livingstone, C.D., and Barton, G.J. (1993). Protein sequence alignments: a strategy for the hierarchical analysis of residue conservation. *Bioinformatics* 9(6)**,** 745-756.

Lu, Q., Xu, Y., Yao, Q., Niu, M., and Shao, F. (2015). A polar-localized iron-binding protein determines the polar targeting of Burkholderia BimA autotransporter and actin tail formation. *Cellular microbiology* 17(3)**,** 408-424.

Malinverni, J.C., Werner, J., Kim, S., Sklar, J.G., Kahne, D., Misra, R., et al. (2006). YfiO stabilizes the YaeT complex and is essential for outer membrane protein assembly in Escherichia coli. *Mol Microbiol* 61(1)**,** 151-164. doi: 10.1111/j.1365-2958.2006.05211.x.

Manley, S., Gillette, J.M., Patterson, G.H., Shroff, H., Hess, H.F., Betzig, E., et al. (2008). High-density mapping of single-molecule trajectories with photoactivated localization microscopy. *Nature methods* 5(2)**,** 155-157. doi: 10.1038/nmeth.1176.

Matthews, J.M. (2012). *Protein dimerization and oligomerization in biology.* Springer Science & Business Media.

Metcalf, D.J., Edwards, R., Kumarswami, N., and Knight, A.E. (2013). Test samples for optimizing STORM super-resolution microscopy. *JoVE (Journal of Visualized Experiments)* (79)**,** e50579-e50579.

Miller, E.A. (2013). The COPII cage sharpens its image. *Nat Struct Mol Biol* 20(2)**,** 139-140. doi: 10.1038/nsmb.2507.

Mlodzianoski, M.J., Juette, M.F., Beane, G.L., and Bewersdorf, J. (2009). Experimental characterization of 3D localization techniques for particle-tracking and super-resolution microscopy. *Opt Express* 17(10)**,** 8264-8277.

Mühlradt, P.F., Menzel, J., Golecki, J.R., and Speth, V. (1973). Outer membrane of *Salmonella. European Journal of Biochemistry* 35(3)**,** 471-481. doi: 10.1111/j.1432-1033.1973.tb02861.x.

Namdari, F., Hurtado-Escobar, G.A., Abed, N., Trotereau, J., Fardini, Y., Giraud, E., et al. (2012). Deciphering the Roles of BamB and Its Interaction with BamA in Outer Membrane Biogenesis, T3SS Expression and Virulence in Salmonella. *PLoS ONE* 7(11).

Noinaj, N., Fairman, J.W., and Buchanan, S.K. (2011). The crystal structure of BamB suggests interactions with BamA and its role within the BAM complex. *Journal of molecular biology* 407(2)**,** 248-260.

Noinaj, N., Gumbart, J.C., and Buchanan, S.K. (2017). The β-barrel assembly machinery in motion. *Nature Reviews Microbiology*. doi: 10.1038/nrmicro.2016.191.

Noinaj, N., Kuszak, A.J., Balusek, C., Gumbart, J.C., and Buchanan, S.K. (2014a). Lateral opening and exit pore formation are required for BamA function. *Structure* 22(7)**,** 1055-1062. doi: 10.1016/j.str.2014.05.008.

Noinaj, N., Kuszak, A.J., Balusek, C., Gumbart, J.C., and Buchanan, S.K. (2014b). Lateral opening and exit pore formation are required for BamA function. *Structure* 22(7)**,** 1055-1062.

Noinaj, N., Kuszak, A.J., Gumbart, J.C., Lukacik, P., Chang, H., Easley, N.C., et al. (2013). Structural insight into the biogenesis of beta-barrel membrane proteins. *Nature* 501(7467)**,** 385-390. doi: 10.1038/nature12521.

Norris, V., and Madsen, M.S. (1995). Autocatalytic gene expression occursviatransertion and membrane domain formation and underlies differentiation in bacteria: a model. *Journal of molecular biology* 253(5)**,** 739-748.

O'Neil, P.K., Rollauer, S.E., Noinaj, N., and Buchanan, S.K. (2015). Fitting the Pieces of the Beta-barrel Assembly Machinery Complex. *Biochemistry* 54(41)**,** 6303-6311. doi: 10.1021/acs.biochem.5b00852.

O'Neil, P.K., Rollauer, S.E., Noinaj, N., and Buchanan, S.K. (2015). Fitting the pieces of the β-barrel assembly machinery complex. *Biochemistry* 54(41)**,** 6303-6311.

Oddershede, L., Dreyer, J.K., Grego, S., Brown, S., and Berg-Sørensen, K. (2002). The motion of a single molecule, the λ-receptor, in the bacterial outer membrane. *Biophysical journal* 83(6)**,** 3152-3161. doi: 10.1016/S0006-3495(02)75318-6.

Oliver, D.B., Cabelli, R.J., Dolan, K.M., and Jarosik, G.P. (1990). Azide-resistant mutants of *Escherichia coli* alter the SecA protein, an azide-sensitive component of the protein export machinery. *Proc Natl Acad Sci U S A* 87(21)**,** 8227-8231.

Olivier, N., Keller, D., Rajan, V.S., Gönczy, P., and Manley, S. (2013). Simple buffers for 3D STORM microscopy. *Biomedical optics express* 4(6)**,** 885-899.

Owen, D.M., Rentero, C., Rossy, J., Magenau, A., Williamson, D., Rodriguez, M., et al. (2010). PALM imaging and cluster analysis of protein heterogeneity at the cell surface. *J Biophotonics* 3(7)**,** 446-454. doi: 10.1002/jbio.200900089.

Owen, P., Meehan, M., de Loughry-Doherty, H., and Henderson, I. (1996). Phase-variable outer membrane proteins in Escherichia coli. *FEMS Immunol Med Microbiol* 16(2)**,** 63-76.

Pallen, M.J., Chaudhuri, R.R., and Henderson, I.R. (2003). Genomic analysis of secretion systems. *Current opinion in microbiology* 6(5)**,** 519-527.

Palomino, C., Marin, E., and Fernandez, L.A. (2011). The fimbrial usher FimD follows the SurA-BamB pathway for its assembly in the outer membrane of Escherichia coli. *J Bacteriol* 193(19)**,** 5222-5230. doi: 10.1128/jb.05585-11.

Patterson, G., Davidson, M., Manley, S., and Lippincott-Schwartz, J. (2010). Superresolution imaging using single-molecule localization. *Annual review of physical chemistry* 61**,** 345-367. doi: 10.1146/annurev.physchem.012809.103444

Plummer, A.M., and Fleming, K.G. (2016). From Chaperones to the Membrane with a BAM! *Trends in Biochemical Sciences* 41(10)**,** 872-882. doi: 10.1016/j.tibs.2016.06.005.

Rassam, P., Copeland, N.A., Birkholz, O., Tóth, C., Chavent, M., Duncan, A.L., et al. (2015). Supramolecular assemblies underpin turnover of outer membrane proteins in bacteria. *Nature* 523(7560)**,** 333-336. doi: 10.1038/nature14461.

Rigel, N.W., Schwalm, J., Ricci, D.P., and Silhavy, T.J. (2012). BamE modulates the Escherichia coli beta-barrel assembly machine component BamA. *J Bacteriol* 194(5)**,** 1002-1008. doi: 10.1128/jb.06426-11.

Ritchie, K., Lill, Y., Sood, C., Lee, H., and Zhang, S. (2013). Single-molecule imaging in live bacteria cells. *Phil. Trans. R. Soc. B* 368(1611)**,** 20120355. doi: 10.1098/rstb.2012.0355.

Rothenberg, E., Sepúlveda, L.A., Skinner, S.O., Zeng, L., Selvin, P.R., and Golding, I. (2011). Single-virus tracking reveals a spatial receptor-dependent search mechanism. *Biophysical journal* 100(12)**,** 2875-2882. doi: 10.1016/j.bpj.2011.05.014.

Rudner, D.Z., and Losick, R. (2010). Protein subcellular localization in bacteria. *Cold Spring Harbor perspectives in biology* 2(4)**,** a000307.

Ruiz, N., Falcone, B., Kahne, D., and Silhavy, T.J. (2005). Chemical conditionality: a genetic strategy to probe organelle assembly. *Cell* 2(121)**,** 307-317.

Ruiz, N., Kahne, D., and Silhavy, T.J. (2006). Advances in understanding bacterial outer-membrane biogenesis. *Nature Reviews Microbiology* 4(1)**,** 57-66.

Rust, M.J., Bates, M., and Zhuang, X. (2006). Sub-diffraction-limit imaging by stochastic optical reconstruction microscopy (STORM). *Nature methods* 3(10)**,** 793-796.

Ryter, A., Shuman, H., and Schwartz, M. (1975). Intergration of the receptor for bacteriophage lambda in the outer membrane of Escherichia coli: coupling with cell division. *Journal of bacteriology* 122(1)**,** 295-301.

Ryu, Y., and Schultz, P.G. (2006). Efficient incorporation of unnatural amino acids into proteins in Escherichia coli. *Nature methods* 3(4)**,** 263.

Samsudin, F., Ortiz-Suarez, M.L., Piggot, T.J., Bond, P.J., and Khalid, S. (2016). OmpA: A Flexible Clamp for Bacterial Cell Wall Attachment. *Structure* 24(12)**,** 2227-2235. doi: 10.1016/j.str.2016.10.009.

Sandoval, C.M., Baker, S.L., Jansen, K., Metzner, S.I., and Sousa, M.C. (2011). Crystal structure of BamD: an essential component of the beta-Barrel assembly machinery of gram-negative bacteria. *J Mol Biol* 409(3)**,** 348-357. doi: 10.1016/j.jmb.2011.03.035.

Schägger, H., and von Jagow, G. (1991). Blue native electrophoresis for isolation of membrane protein complexes in enzymatically active form. *Analytical biochemistry* 199(2)**,** 223-231.

Schindler, M., Osborn, M., and Koppel, D.E. (1980). Lateral diffusion of lipopolysaccharide in the outer membrane of *Salmonella typhimurium*. doi: 10.1038/285261a0.

Schirmer, T., Keller, T.A., Wang, Y.-F., and Rosenbusch, J.P. (1995). Structural basis for sugar translocation through maltoporin channels at 3.1 angstrom resolution. *Science* 267(5197)**,** 512. doi: 10.1126/science.7824948.

Selkrig, J., Leyton, D.L., Webb, C.T., and Lithgow, T. (2014). Assembly of beta-barrel proteins into bacterial outer membranes. *Biochim Biophys Acta* 1843(8)**,** 1542-1550. doi: 10.1016/j.bbamcr.2013.10.009.

Shapiro, L., McAdams, H.H., and Losick, R. (2002). Generating and exploiting polarity in bacteria. *Science* 298(5600)**,** 1942-1946.

Sinnige, T., Weingarth, M., Renault, M., Baker, L., Tommassen, J., and Baldus, M. (2014). Solid-state NMR studies of full-length BamA in lipid bilayers suggest limited overall POTRA mobility. *Journal of molecular biology* 426(9)**,** 2009-2021.

Sklar, J.G., Wu, T., Gronenberg, L.S., Malinverni, J.C., Kahne, D., and Silhavy, T.J. (2007). Lipoprotein SmpA is a component of the YaeT complex that assembles outer membrane proteins in Escherichia coli. *Proceedings of the National Academy of Sciences* 104(15)**,** 6400-6405.

Slusky, J.S. (2017). Outer membrane protein design. *Current Opinion in Structural Biology* 45**,** 45-52. doi: 10.1016/j.sbi.2016.11.003.

Smit, J., and Nikaido, H. (1978). Outer membrane of gram-negative bacteria. XVIII. Electron microscopic studies on porin insertion sites and growth of cell surface of *Salmonella typhimurium*. *Journal of Bacteriology* 135(2)**,** 687-702. doi: 10.1101/cshperspect.a000414.

Spector, J., Zakharov, S., Lill, Y., Sharma, O., Cramer, W.A., and Ritchie, K. (2010). Mobility of BtuB and OmpF in the *Escherichia coli* outer membrane: implications for dynamic formation of a translocon complex. *Biophysical journal* 99(12)**,** 3880-3886. doi: 10.1016/j.bpj.2010.10.029.

Stenberg, F., von Heijne, G., and Daley, D.O. (2007). Assembly of the cytochrome bo3 complex. *J Mol Biol* 371(3)**,** 765-773. doi: 10.1016/j.jmb.2007.05.045.

Stubenrauch, C., Belousoff, M.J., Hay, I.D., Shen, H.-H., Lillington, J., Tuck, K.L., et al. (2016). Effective assembly of fimbriae in Escherichia coli depends on the

translocation assembly module nanomachine. 1**,** 16064. doi: 10.1038/nmicrobiol.2016.64

Sundararaj, S., Guo, A., Habibi-Nazhad, B., Rouani, M., Stothard, P., Ellison, M., et al. (2004). The CyberCell Database (CCDB): a comprehensive, self-updating, relational database to coordinate and facilitate in silico modeling of *Escherichia coli*. *Nucleic Acids Res* 32(Database issue)**,** D293-295. doi: 10.1093/nar/gkh108.

Thiem, S., Kentner, D., and Sourjik, V. (2007). Positioning of chemosensory clusters in *E. coli* and its relation to cell division. *The EMBO journal* 26(6)**,** 1615-1623. doi: 10.1038/sj.emboj.7601610.

Thiem, S., and Sourjik, V. (2008). Stochastic assembly of chemoreceptor clusters in *Escherichia coli*. *Molecular microbiology* 68(5)**,** 1228-1236. doi: 10.1111/j.1365-2958.2008.06227.x.

Tommassen, J. (2010). Assembly of outer-membrane proteins in bacteria and mitochondria. *Microbiology* 156(9)**,** 2587-2596.

Toomre, D., and Bewersdorf, J. (2010). A new wave of cellular imaging. *Annual review of cell and developmental biology* 26**,** 285-314. doi: 10.1146/annurev-cellbio-100109-104048.

Ureta, A.R., Endres, R.G., Wingreen, N.S., and Silhavy, T.J. (2007). Kinetic analysis of the assembly of the outer membrane protein LamB in Escherichia coli mutants each lacking a secretion or targeting factor in a different cellular compartment. *Journal of bacteriology* 189(2)**,** 446-454.

Ursell, T.S., Trepagnier, E.H., Huang, K.C., and Theriot, J.A. (2012). Analysis of surface protein expression reveals the growth pattern of the gram-negative outer membrane. *PLoS Comput Biol* 8(9)**,** e1002680. doi: 10.1371/journal.pcbi.1002680.

van der Woude, M.W., and Henderson, I.R. (2008). Regulation and function of Ag43 (flu). *Annu Rev Microbiol* 62**,** 153-169. doi: 10.1146/annurev.micro.62.081307.162938.

Verhoeven, G.S., Dogterom, M., and den Blaauwen, T. (2013). Absence of long-range diffusion of OmpA in *E. coli* is not caused by its peptidoglycan binding domain. *BMC microbiology* 13(1)**,** 66. doi: 10.1186/1471-2180-13-66.

Voulhoux, R., Bos, M.P., Geurtsen, J., Mols, M., and Tommassen, J. (2003). Role of a highly conserved bacterial protein in outer membrane protein assembly. *Science* 299(5604)**,** 262-265.

Vuong, P., Bennion, D., Mantei, J., Frost, D., and Misra, R. (2008). Analysis of YfgL and YaeT interactions through bioinformatics, mutagenesis, and biochemistry. *Journal of bacteriology* 190(5)**,** 1507-1517.

Walther, D.M., Rapaport, D., and Tommassen, J. (2009). Biogenesis of β-barrel membrane proteins in bacteria and eukaryotes: evolutionary conservation and divergence. *Cellular and Molecular Life Sciences* 66(17)**,** 2789-2804.

Wang, H., Wingreen, N.S., and Mukhopadhyay, R. (2008). Self-organized periodicity of protein clusters in growing bacteria. *Physical Review Letters* 101(21)**,** 218101. doi: 10.1103/PhysRevLett.101.218101.

Wang, L., Brock, A., Herberich, B., and Schultz, P.G. (2001). Expanding the genetic code of Escherichia coli. *Science* 292(5516)**,** 498-500.

Wang, L., Xie, J., and Schultz, P.G. (2006). Expanding the genetic code. *Annu. Rev. Biophys. Biomol. Struct.* 35**,** 225-249.

Webb, C.T., Selkrig, J., Perry, A.J., Noinaj, N., Buchanan, S.K., and Lithgow, T. (2012). Dynamic association of BAM complex modules includes surface exposure of the lipoprotein BamC. *J Mol Biol* 422(4)**,** 545-555. doi: 10.1016/j.jmb.2012.05.035.

Whelan, D.R., Holm, T., Sauer, M., and Bell, T.D. (2014). Focus on super-resolution imaging with direct stochastic optical reconstruction microscopy (dSTORM). *Australian Journal of Chemistry* 67(2)**,** 179-183.

Wisniewski, J.R., and Rakus, D. (2014). Multi-enzyme digestion FASP and the 'Total Protein Approach'-based absolute quantification of the *Escherichia coli* proteome. *J Proteomics* 109**,** 322-331. doi: 10.1016/j.jprot.2014.07.012.

Wittelsberger, A., Mierke, D.F., and Rosenblatt, M. (2008). Mapping Ligand–receptor Interfaces: Approaching the Resolution Limit of Benzophenone-based Photoaffinity Scanning. *Chemical biology & drug design* 71(4)**,** 380-383.

Wolter, S., Loschberger, A., Holm, T., Aufmkolk, S., Dabauvalle, M.C., van de Linde, S., et al. (2012). rapidSTORM: accurate, fast open-source software for localization microscopy. *Nat Methods* 9(11)**,** 1040-1041. doi: 10.1038/nmeth.2224.

Wu, T., Malinverni, J., Ruiz, N., Kim, S., Silhavy, T., and Kahne, D. (2005). Identification of a multicomponent complex required for outer membrane biogenesis in Escherichia coli. *Cell* 121(2)**,** 235-245.

Xie, X.S., Choi, P.J., Li, G.-W., Lee, N.K., and Lia, G. (2008). Single-molecule approach to molecular biology in living bacterial cells. *Annu. Rev. Biophys.* 37**,** 417-444. doi: 10.1146/annurev.biophys.37.092607.174640.

Xu, C., and Min, J. (2011). Structure and function of WD40 domain proteins. *Protein & cell* 2(3)**,** 202-214.

Yatime, L., Hein, K.L., Nilsson, J., and Nissen, P. (2011). Structure of the RACK1 dimer from Saccharomyces cerevisiae. *Journal of molecular biology* 411(2)**,** 486-498.

Zhang, H., Gao, Z.-Q., Hou, H.-F., Xu, J.-H., Li, L.-F., Su, X.-D., et al. (2011). High-resolution structure of a new crystal form of BamA POTRA4–5 from Escherichia coli. *Acta Crystallographica Section F: Structural Biology and Crystallization Communications* 67(7)**,** 734-738.